Electromechanical Characterization of Microresonators for Circuit Applications

by Tu-Cuong (Clark) Nguyen

Research Project

Submitted to the Department of Electrical Engineering and Computer Sciences, University of California at Berkeley, in partial satisfaction of the requirements for the degree of **Master of Science, Plan II.**

Approval for the Report and Comprehensive Examination:

Committee:

Roger T. Howe

Professor Roger T. Howe
Research Advisor

April 23, 1991

(Date)

* * * * *

Richard S. Muller

Professor Richard S. Muller
Second Reader

April 25, 1991

(Date)

ELECTROMECHANICAL CHARACTERIZATION OF MICRORESONATORS FOR CIRCUIT APPLICATIONS

by

Tu-Cuong (Clark) H. Nguyen

Submitted to the Graduate Faculty
of the Department of Electrical Engineering and Computer Sciences
in partial fulfillment of
the requirement for the degree of
Master of Science, Plan II

University of California at Berkeley
April 21, 1991

ABSTRACT

The design of circuits incorporating microresonators which utilize electrostatic drive and sense is accompanied by a need for a convenient method to experimentally extract the circuit elements modelling the microresonators. Previously, techniques which *electrically* detect microresonator motional current using only *off-chip* electronics have been seriously hampered by parasitic feedthrough currents arising from probe-to-probe capacitance, which mask the tiny motional current.

In this report, equivalent circuits for electrostatic-comb driven and parallel-plate driven microresonators are derived. Resonance frequency, quality factor, and $\frac{\partial C}{\partial x}$ are found to be the key measurable parameters in determining equivalent circuit elements. Using the derived circuit models, parasitic-induced distortion of microresonator electrical performance is quantified. Measurements and simulation of low frequency ($f_r = 20kHz$) microresonators conclude that ac drive voltages on the order of millivolts define the threshold whereby motional current can be measured with acceptable interference from probe-to-probe parasitics without the need for special parasitic suppression techniques.

Techniques allowing *off-chip electrical* detection of microresonator motional current without interference from parasitics are then introduced. These detection strategies operate by separating motional current from parasitics in either the time or frequency domains; effectively, they eliminate all dc capacitance and sense only ac (motional) capacitance. The time-domain technique (GSED) detects motional current during the zero-input period of a gated-sinusoid excitation signal, and thus, depends upon the high-Q of the microresonator for sustainance of oscillation during detection. The frequency domain technique (EAM) is implemented by biasing the microresonator with a high-frequency carrier signal in addition to the required dc-bias. Qualitatively, the carrier signal and its time-derivative are multiplied by capacitive elements of microstructure motion, resulting in motional current, frequency-shifted to sidebands around the carrier frequency and separated from dc parasites still at the drive frequency.

Application of these techniques (particularly EAM) to microresonator circuit model extraction, ground plane design, and system performance verification will be demonstrated. A novel microelectromechanical filter implemented using parallel microresonators will be introduced in the process.

ACKNOWLEDGEMENTS

I would like to express, first, my deepest appreciation for the technical guidance and support given by my research advisor, Professor Roger T. Howe. His vast knowledge of numerous engineering disciplines, coupled with an unmatchable enthusiasm for the field of microsensors and microelectromechanics, continues to enhance my own intellectual development and ability to conduct research.

Professors Muller and White of the Berkeley Sensor and Actuator Center (BSAC) also deserve great thanks for their interest in my research and encouragement during research presentations. Professor White suggested the Gated-Sinusoid Excitation and Detection (GSED) technique.

In addition, I would like to thank Dr. Jon Bernstein (currently of Draper Labs.) for conversations inspiring the Electromechanical Amplitude Modulation (EAM) characterization technique.

Several BSAC students were helpful in the successful completion of this work. Collaboration with (Dr.) Bill Tang (now at Ford Motor Co.), who invented the electrostatic-comb driven lateral microresonator, gave me hands on and instant knowledge of the workings and fabrication of this device. The practical advice, laboratory assistance, and bad taste in music of (Prof.) Jim Chung (now at MIT) are much appreciated. (Dr.) Carlos Mastrangelo (now at Ford), the local UNIX and microfabrication guru, has also been very helpful. I am also grateful for practical electronics advice from Stuart Wenzel. In addition, I would like to thank Kay Huang for pursuing a project to extend the bandwidth of the current EAM system.

Sometimes bogus, but stimulating, technical and casual conversations from the aforementioned and Reza Moazzami, Guochun Liang (who lived in Cory Hall), Jian Chen, Martin Lim, Joe (Chih-Chieh) King, Tim Hu, and Yu-Chong Tai are much appreciated.

Finally, I would like to thank my parents and brothers for their support and encouragement (and understanding).

TABLE OF CONTENTS

1.0 INTRODUCTION

Mechanical resonators have proven to be highly sensitive probes for physical or chemical parameters which alter their potential or kinetic energy. This sensitivity, usually occuring as a resonance frequency shift, has been harnessed by recent microfabricated sensors, which utilize resonant micromechanical structures as transducing elements [1, 2, 3, 4][1] . Microsensors for detecting pressure [5, 6, 7], acceleration [8], and vapor concentration [9] have been demonstrated. In addition to the aforementioned sensor applications, the high quality factor Q of microresonators in vacuum suggests a strong potential for use as frequency references in monolithic systems and as electromechanical filters.

The design of circuits incorporating microresonators which utilize electrostatic drive and sense is accompanied by a need for a convenient method to experimentally extract the circuit elements modelling the microresonators. In general, these circuit elements are primarily determined by the resonance frequency ω_r, the quality factor Q, and the change in shuttle-to-electrode capacitance per unit displacement $\frac{\partial C}{\partial x}$. The last two of these parameters are particularly difficult to determine theoretically, since they depend heavily upon second order effects. For example, Q depends upon the energy dissipation mechanisms in the system. For the case of an electrostatic-comb driven lateral microresonator, Couette flow is the dominant, but not the only, dissipation mechanism of importance [10], and thus, accurate prediction of Q requires consideration of more than just simple Couette effects. $\frac{\partial C}{\partial x}$ is even more difficult to predict, since it is strongly influenced by both fringing electric fields and by bias-induced levitation of the movable shuttle [11]. These parameters, however, can be readily determined from an electrically measured microresonator transconductance spectrum.

Historically, implementation of a convenient, off-chip, open-loop, electrical characterization technique for capacitively excited and sensed microresonators has been difficult. To start, the motional current to be detected is miniscule, on the order of picoamperes for

[1]Parenthetical references placed superior to the line of text refer to the bibliography.

low Q (air-damped) situations. Furthermore, feedthrough currents arising from parasitic capacitance between probes contacting the drive and sense ports mask the motional current of the dc-biased oscillating structure. Thus, partially successful attempts to detect resonance electrically have been limited to the use of on-chip circuitry or the use of special, tedious precautions, including the requirement of operation in vacuum, to attenuate parasitic feedthrough [12].

The above restrictions to *electrical* transfer function measurement have led to *optical* techniques [13], in which laser light, reflected from an oscillating microstructure, is detected. However, optical techniques suffer from several drawbacks. First, alignment of laser light, even via optical fibers, is a tedious affair, making transfer function determination somewhat inconvenient from structure to structure. Second, special, more expensive equipment is necessary for high-Q vacuum applications, since it is difficult to feed a fiber into a vacuum environment. Finally, and most importantly, actual *electrical* information is not provided; important information concerning the electrical performance of capacitively driven and sensed microstructures (as used in sensors, oscillators, etc.) is lacking, and thus, direct performance verification of electronic systems utilizing microresonators is not possible.

This report details two novel techniques which allow detection of microresonator motional current through *off-chip electrical* means by separating motional current from feedthrough in the either the time or frequency domains. The time domain technique (GSED; Chapter 4) involves exciting a high-Q microresonator via a gated-sinsoid and detecting motional current by open-loop, off-chip, electronic instrumentation during the zero-input period of the excitation signal.

The frequency domain technique (Chapter 5) allows not only detection of motional current, but also accurate determination of a microresonator transconductance spectrum. It is achieved by applying a high frequency ac signal (on top of the dc bias) to the microstructure. This signal serves as a carrier which is modulated by the time-varying sense capacitance of the resonating structure, therefore, separating motional current from dc feedthrough in the frequency domain. Even the intrinsic dc capacitance of the microstructure is effectively eliminated.

This electromechanical amplitude modulation (EAM) technique is useful for one-port, as well as multi-port, microstructures with virtually any range of Q. It has been successfully

demonstrated as a convenient, repeatable, wafer-level measurement technique and shows potential for application in integrated detection circuitry.

In addition to providing a detailed description of the EAM characterization technique, this report will also demonstrate its application to microresonator circuit model extraction and system performance verification (for the case of a microelectromechanical filter; Chapter 6). First, however, equivalent circuits for microresonators are derived (Chapter 2), and the role of parasitic feedthrough interference in dictating feasible detection techniques (Chapter 3) is discussed.

2.0 EQUIVALENT CIRCUITS FOR MICRORESONATORS

Of the several existing methods for exciting the resonance of micromechanical structures [1, 5, 6, 7, 9, 14], capacitive (electrostatic) excitation and detection have proven attractive for conducting microstructures, in particular those constructed of polysilicon, since this approach offers fabrication simplicity which avoids complicated stress relief problems [15, 16]. Several forms of capacitive drive and detection are available, including parallel-plate [1, 9, 12], electrostatic-comb [10], and T [17] types, shown in Figs. 2.1(a), 2.1(b), and 2.1(c), respectively.

Parallel-plate-capacitor drive and sense is possibly the most obvious of the three, and thus, has been common in such applications as quartz cantilever oscillators in wrist watches [*], and recently, as the resonant element in a vapor sensor [9]. However, several drawbacks complicate the design of systems utilizing microresonators excited and sensed via parallel-plate-capacitors. First, for large vibration amplitudes, the force arising from the application of an ac drive voltage is nonlinearly dependent on that voltage, and thus, the voltage-to-current transfer function is nonlinear. Consequently, only small amplitudes are allowed for linear operation. In addition, for vertical resonators[1], the quality factor Q of the resonance is very low at atmospheric pressure because of squeeze-film damping in the micron-sized capacitor gap [9]. The Q can be raised by orders of magnitude in a vacuum environment, but unfortunately, this further complicates system design, since the very high intrinsic Q and the efficient parallel-plate excitation restrict excitation voltages to the millivolt range. Design of the sustaining amplifier is complicated by the requirement of amplitude limiting [12].

Electrostatic-comb driven and sensed lateral microresonators offer numerous advantages over parallel-plate driven types and show the most promise for system applications. The most significant advantage is that the drive capacitance is linear with displacement

[1]Parallel-plate driven microresonators which vibrate vertically have been most common, since they allow the largest overlap area for the drive capacitor.

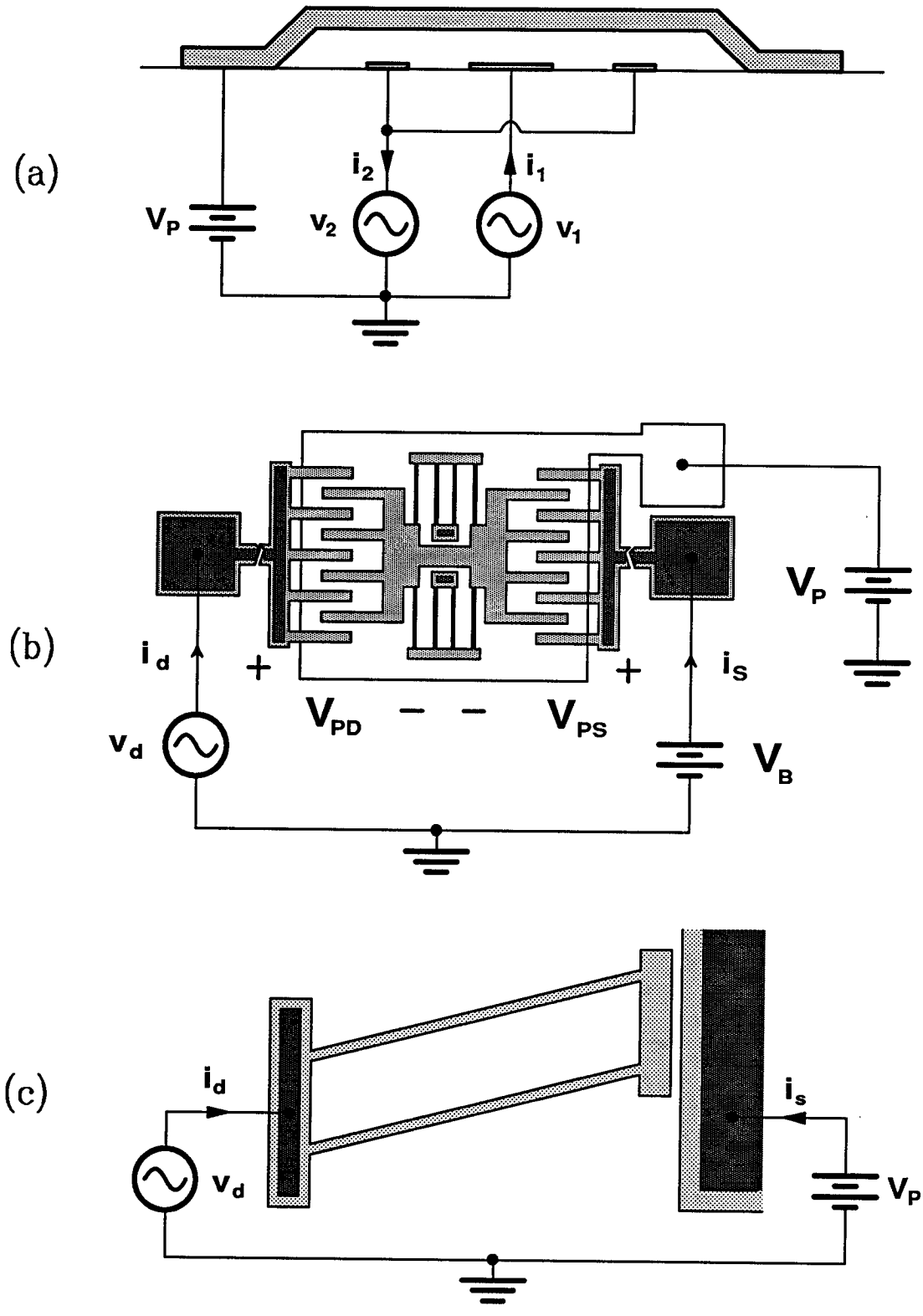

Figure 2.1. Electrostatic drive and sense of microresonators with bias and excitation circuit configuration included. For each type, V_P and V_S are bias voltages, v_d is an ac excitation signal, and i_s is the sense current. (a) Parallel-plate driven vertical microresonator. (b) Electrostatic-comb driven lateral microresonator. (c) T-driven lateral microresonator.

of the structure, resulting in a force which is independent of the vibration amplitude. This leads to a linear voltage-to-current transfer function! Furthermore, the use of weaker fringing fields to excite resonance allows larger steady-state excitation voltages under high Q conditions (i.e. in vacuum), and thus, greatly simplifies design of a sustaining amplifier. The folded-beam support feature leads to a larger range of linear operation, and also, serves as a residual stress relief mechanism. Additional rewards come from lateral operation of the microresonator, namely higher Q in air[2], more flexibility in the geometric design of the microresonator[3], and the lithographic convenience of having all critical features defined in a single mask. Last, but certainly not least, testing and study of these microresonators is very much facilitated, since their motion can be viewed under the high magnification of an optical microscope.

Microresonators excited to lateral motion via T-drive are relative newcomers to the field. They offer the advantage over parallel-plate driven types of a larger range of motion (over 40 μm) with a large drive force. However, they retain the hindrance of a nonlinear voltage-to-current transfer function.

Due to the above considerations, the majority of the results for this report were obtained using electrostatic-comb driven and sensed lateral microresonators.

2.1 Small Signal Equivalent Circuits for Microresonators

The equivalent circuit describing microresonator performance under ac electrostatic excitation can be derived through consideration of the electromechanics dictated by resonator geometry. In particular, the geometries of the drive and sense ports determine the drive and sense configurations (e.g. electrostatic-comb, parallel-plate, T, etc...), and thus, directly influence electrical performance. Since the electrostatic-comb configuration offers several advantages over others, it is of the most interest and will be the focus of the detailed derivation in the following subsection.

It must be stressed that the equivalent circuits presented in this section represent microresonators in the ideal case which neglects parasitic elements. The circuits are, thus,

[2]Under atmospheric pressure, the Q is high relative to vertical resonators, since Couette flow (rather that squeeze-film damping) in the gap between the resonating shuttle and the substrate comprises the dominant dissipative mechanism. Couette flow is much less dissipative than squeeze-film damping.

[3]For example, differential excitation and detection, as well as torsional resonators, are made possible.

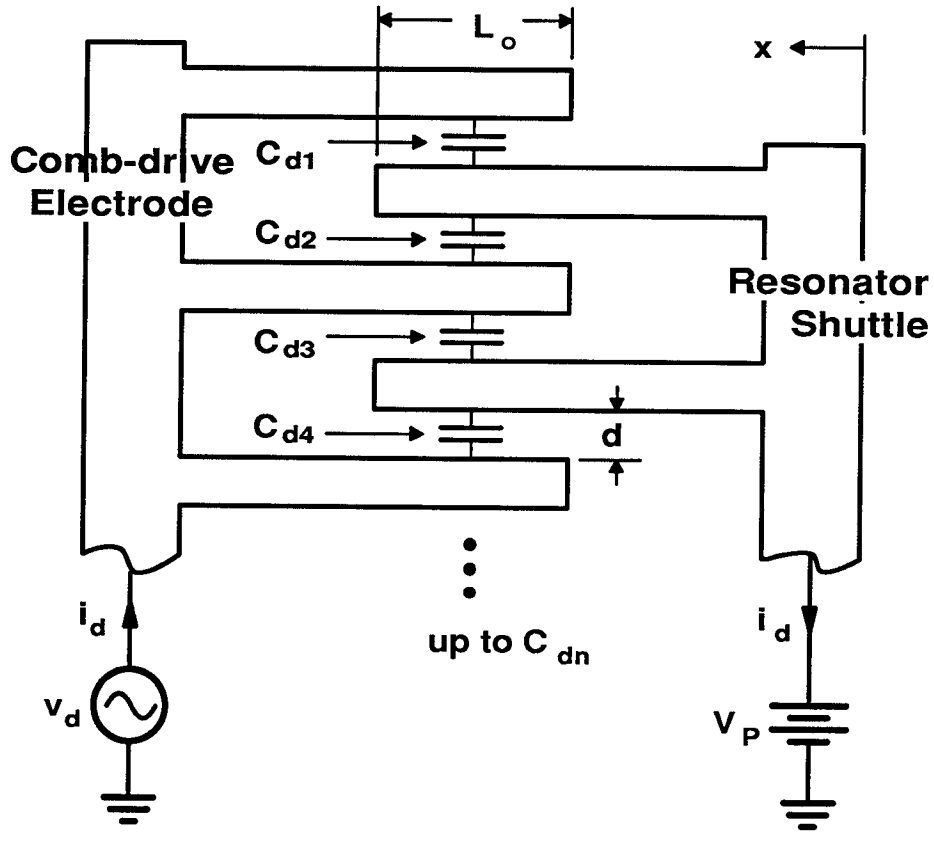

Figure 2.2. Expanded view of the interdigitated finger structure at the drive port of an electrostatic-comb driven microresonator. Distances relevant to electromechanical analysis are indicated, as are the individual finger-overlap capacitors, C_{dn}. The direction of shuttle motion x is defined such that the overlap capacitance increases with x.

most applicable to the case where microresonator motion is excited and sensed by on-chip circuitry. Off-chip excitation and detection will be discussed thoroughly in the chapters that follow.

2.1.1 Equivalent Circuit for a Two-Port Electrostatic-Comb Driven and Sensed Lateral Microresonator

The geometries involved for capacitive drive and sense of an electrostatic-comb driven lateral microresonator are summarized in Fig. 2.2. This figure depicts an expanded view of the interdigitated finger structure, indicating the gap d, the individual overlap capacitors

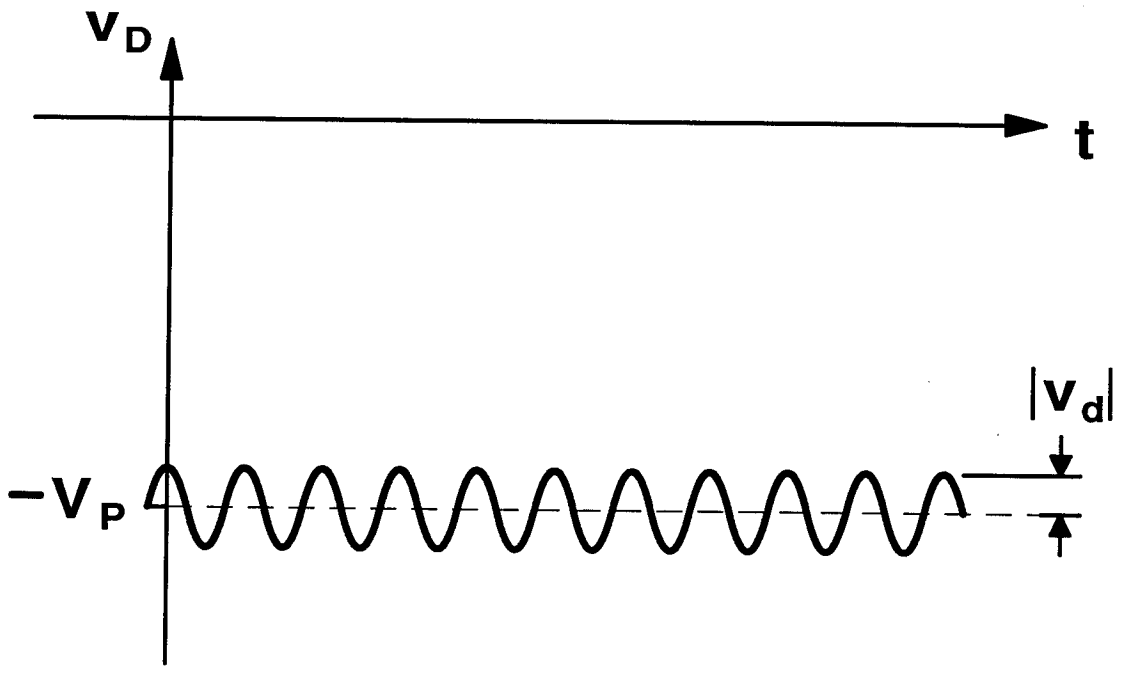

Figure 2.3. Effective excitation voltage for the drive and bias configuration of Fig. 2.1 with V_P positive.

C_{dn}, and the finger overlap length L_o. The direction of shuttle motion x is defined such that x increases with increasing overlap capacitance.

Biasing and excitation of the microresonator is also shown in Fig. 2.2. This derivation considers the case where a dc bias V_P (e.g. $|V_P| = 50$ V in air) is applied to the microresonator, which is driven by an ac signal v_d ($|v_d| = 10$ V in air). The effective excitation voltage is, thus, $v_D = v_d - V_P$, graphed in Fig. 2.3, for V_P positive.[4] The dc bias V_P is necessary for two reasons: First, as will be derived, the resulting ac drive force f_d is directly proportional to V_P; and secondly, the dc bias provides an offset which allows the frequency of the drive force to be identical with the frequency of the drive voltage. Without the dc offset, the force f_d would peak at both the maxima and minima of the v_d waveform, and thus, it would have twice the frequency of the excitation voltage v_d.

Let us now consider the input drive admittance for the lateral microresonator of Fig. 2.2,

[4] As will be apparent later, whether V_P is positive or negative has no consequence on the equivalent circuit for a microresonator. The effective input resistance at resonance will be positive for both cases.

defined (in phasor form) by

$$Y_d(j\omega) = \frac{I_d(j\omega)}{V_d(j\omega)}. \tag{2.1}$$

To start, we define explicitly the bias and excitation parameters of interest:

$$v_d(t) = |v_d| \cos \omega t \tag{2.2}$$

$$v_D(t) = v_d(t) - V_P = v_d(t) + V_{PD}, \tag{2.3}$$

where $V_{PD} = -V_P$ has been introduced for later notational consistency. In addition, the capacitors $C_{d0} \ldots C_{dn}$ are all in parallel and so will be lumped into a single time-variable capacitor

$$C(t) = \begin{cases} \approx C_o & \text{off resonance} \\ C_o + C_m(t) & \text{at resonance} \end{cases} \tag{2.4}$$

$$C_m(t) = |C_m| \sin \omega_r t \tag{2.5}$$

where $C(t)$ represents the total capacitance at the drive port, C_o is the total dc capacitance (i.e. the value of capacitance for a motionless shuttle), and $C_m(t)$ is the total (ac) motional capacitance with peak amplitude $|C_m|$. Note that the motion of the microresonator as measured by x lags the excitation force f_d by 90° at resonance, therefore the capacitance $C(t)$ must lag the excitation voltage v_d by 90°. With this, let us proceed to find an expression for $i_d(t)$. A general expression for $i_d(t)$ can be written

$$i_d(t) = C(t)\frac{dv_D(t)}{dt} + v_D(t)\frac{\partial C(t)}{\partial t}. \tag{2.6}$$

From Eqs. (2.4) and (2.5), $\frac{\partial C(t)}{\partial t}$ $\left[= \frac{\partial C(x,t)}{\partial x}\right]$ can be expressed as

$$\frac{\partial C(t)}{\partial t} = \frac{\partial C}{\partial x}\frac{\partial x}{\partial t}. \tag{2.7}$$

Applying Eqs. (2.3), (2.4), and (2.7) to the general form for $i_d(t)$, Eq. (2.6), yields

$$i_d(t) = C_o\frac{dv_d}{dt} + x\frac{\partial C}{\partial x}\frac{dv_d}{dt} + V_{PD}\frac{\partial C}{\partial x}\frac{\partial x}{\partial t} + v_d\frac{\partial C}{\partial x}\frac{\partial x}{\partial t}, \tag{2.8}$$

and converting to phasor form, we obtain

$$I_d = C_o j\omega V_d + 2\frac{\partial C}{\partial x} j\omega V_d X + V_{PD}\frac{\partial C}{\partial x} j\omega X. \tag{2.9}$$

The first term in Eq. (2.9) represents the feedthrough current arising from an ac excitation voltage v_d across an effective dc capacitor with value C_o. The second represents a modulation component at twice the excitation frequency. It results from multiplicative interaction

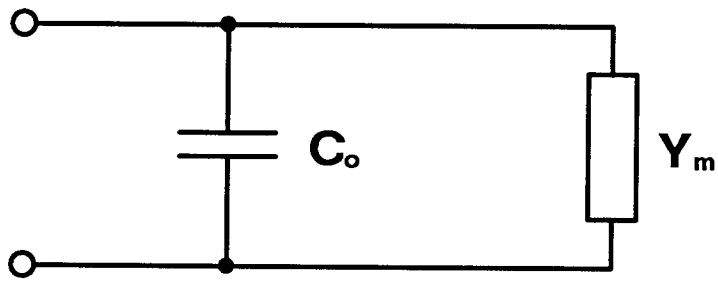

Figure 2.4. Circuit diagram depicting the equivalent impedance looking into the drive port of a microresonator.

between the microresonator ac capacitance $C(t)$ and the excitation voltage v_d. The third component is the motional current arising from the dc biased microresonator time-varying capacitor $C(t)$.

In practice, the microresonator will be biased such that $V_P \gg |v_d|$ (or $|V_{PD}| \gg |v_d|$). For example, in air, typical bias and excitation voltages are $V_P = 80$ V and $|v_d| = 5$ to 10 V; while in vacuum, $V_P = 5$ V and $|v_d| = 10$ mV are typical. Thus, in practice, the modulation component (second term of Eq. (2.9)) will generally be the smallest of the three i_d constituents. With this in mind, the modulation component will be neglected in the derivation of the drive admittance given by Eq. (2.1). It, however, will be reconsidered in a later chapter as a possible means for detection of microstructure resonance.

Equation (2.9), after neglecting the second component, can be seen to have an equivalent circuit comprised of the parallel combination of the capacitor C_o and the drive admittance due to motional current $Y_x(j\omega)$ shown in Fig. 2.4. To find an expression for $Y_x(j\omega)$, given by

$$Y_x(j\omega) = \frac{I_x(j\omega)}{V_d(j\omega)}, \tag{2.10}$$

where $I_x(j\omega)$ is the phasor motional current given by the third component of Eq. (2.9)

$$I_x(j\omega) = V_{PD}\frac{\partial C}{\partial x} j\omega X, \tag{2.11}$$

we must first find $N_d(j\omega)$, the transfer function relating shuttle displacement x to drive voltage v_d. In phasor form

$$N_d(j\omega) = \frac{X(j\omega)}{V_d(j\omega)}. \tag{2.12}$$

To achieve this goal, we proceed to find the drive force f_d in terms of the drive voltage v_d. This can be found as follows:

$$\begin{aligned} f_d &= \frac{1}{2}v_D{}^2\frac{\partial C}{\partial x} = \frac{1}{2}(v_d + V_{PD})^2\frac{\partial C}{\partial x} \\ &= \frac{1}{2}\{V_{PD}{}^2 + 2|v_d|V_{PD}\cos\omega t + |v_d|^2\cos^2\omega t\}\frac{\partial C}{\partial x} \\ &= \frac{1}{2}\{\underbrace{V_{PD}{}^2 + \frac{|v_d|^2}{2}}_{\text{dc term}} + \underbrace{2|v_d|V_{PD}\cos\omega t}_{\text{drive frequency component}} + \underbrace{\frac{|v_d|^2}{2}\cos 2\omega t}_{\text{second harmonic}}\}\frac{\partial C}{\partial x}. \end{aligned} \tag{2.13}$$

With the simultaneous assumptions that the resonator has a reasonably large quality factor and that $|v_d| \ll V_P$, we may neglect the dc term and the second harmonic. The phasor form for the driving force, then, becomes

$$F_d = V_{PD}\frac{\partial C}{\partial x}V_d. \tag{2.14}$$

The electrostatic force $F_d(j\omega)$ may be related to the average deflection $X(j\omega)$ of the shuttle via the transfer function [1]

$$M_d(j\omega) = \frac{X(j\omega)}{F_d(j\omega)} = \frac{k_{sys}^{-1}}{1-(\omega/\omega_r)^2 + j(\omega/Q\omega_r)} \tag{2.15}$$

where ω_r is the first lateral resonance frequency, Q is the quality factor, and k_{sys} is the system spring constant for the microresonator[5].

[5]For the microresonator of Fig. 2.1(b), the fundamental lateral resonance frequency ω_r can be accurately determined, using Rayleigh's Method [21]:

$$\omega_r = \left[\frac{k_{sys}}{(M_p + 0.3714M)}\right]^{\frac{1}{2}} \tag{2.16}$$

where M_p and M are the masses of the plate and of the supporting beams, respectively. For the folded-beam structure, an analytical expression for k_{sys} can be found by neglecting residual strain and assuming that the trusses joining the folded beam segments are rigid:

$$k_{sys} = 24EI/L^3 = 2Eh(W\,L)^3, \tag{2.17}$$

where $I = (1/12)hW^3$ is the moment of inertia of the beams. Combining Eqs. (2.16) and (2.17), it follows that

$$\omega_r = \left[\frac{2Eh(W/L)^3}{(M_p + 0.3714M)}\right]^{\frac{1}{2}} \tag{2.18}$$

Quality factor Q in air can be estimated by assuming that Couette flow underneath the plate is the dominant dissipative process [18]:

$$Q = \frac{z}{\mu A_p}(M_p k_{sys})^{\frac{1}{2}} \tag{2.19}$$

where μ is the absolute viscosity of air ($1.8 \times 10^{-5}\,\mathrm{N\cdot s\cdot m^{-2}}$), and z is the offset between the plate and the substrate. Equation (2.19), however, tends to overshoot the actual Q, indicating that Couette flow is not the only dissipative factor [10].

From Eqs. (2.14) and (2.15) $N_d(j\omega)$ is found to be

$$N_d(j\omega) = \frac{X(j\omega)}{V_d(j\omega)} = M_d(j\omega)V_{PD}\frac{\partial C}{\partial x} = \frac{k_{sys}^{-1}V_{PD}\frac{\partial C}{\partial x}}{1-(\omega/\omega_r)^2+j(\omega/Q\omega_r)}. \tag{2.20}$$

Note that the above equation correctly indicates that the shuttle motion lags the excitation voltage by 90° at resonance.

Having established the excitation voltage to shuttle displacement transfer function, we may now determine $Y_x(j\omega)$, the transfer function relating excitation voltage $V_d(j\omega)$ to motional current $I_x(j\omega)$. From Eqs. (2.11) and (2.20), we have

$$Y_x(j\omega) = \frac{I_x(j\omega)}{V_d(j\omega)} = \frac{j\omega k_{sys}^{-1}V_{PD}^2\left(\frac{\partial C}{\partial x}\right)^2}{1-(\omega/\omega_r)^2+j(\omega/Q\omega_r)}. \tag{2.21}$$

From the above equation, we see that $I_x(j\omega)$ is in phase with the excitation voltage $V_d(j\omega)$. The block element in Fig. 2.4 may now be recognized as a series LCR circuit with elements given by the following equations:

$$C_d = \frac{V_{PD}^2}{k_{sys}}\left(\frac{\partial C}{\partial x}\right)^2 \tag{2.22}$$

$$L_d = \frac{k_{sys}}{\omega_r^2 V_{PD}^2\frac{\partial C}{\partial x}} \tag{2.23}$$

$$R_d = \frac{k_{sys}}{\omega_r Q V_{PD}^2\frac{\partial C}{\partial x}}. \tag{2.24}$$

For the two-port drive and sense configuration of current interest, shown in Fig. 2.1(b), the current i_s at the sense port arises purely from a dc-biased time-varying capacitance, and thus, its form will be similar to that of i_x above. The general equation for i_s is

$$i_s = V_{PS}\left(\frac{\partial C}{\partial x}\right)_s\frac{\partial x}{\partial t} \tag{2.25}$$

$$I_s = \frac{j\omega k_{sys}^{-1}V_{PD}V_{PS}\left(\frac{\partial C}{\partial x}\right)_d\left(\frac{\partial C}{\partial x}\right)_s}{1-(\omega/\omega_r)^2+j(\omega/Q\omega_r)}V_d. \tag{2.26}$$

where $V_{PS} = V_B - V_P$ is equal to $-V_P$ if the sense port is grounded[6], and $\left(\frac{\partial C}{\partial x}\right)_d$ and $\left(\frac{\partial C}{\partial x}\right)_s$ are the change in capacitance per unit displacement of the shuttle at the drive port and

[6]Microresonator performance is most linear if the sense port is grounded so that $V_P = V_S$, since in this case, levitation due to the ground plane-induced imbalance of vertical electric fields /citelevitation will be balanced on both sides of the shuttle. Biasing such that $V_P \neq V_B$ should be avoided.

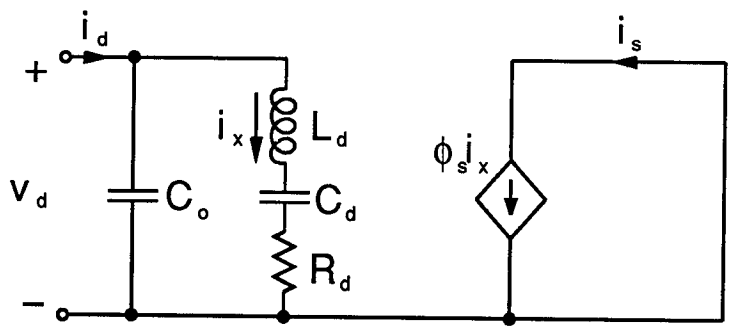

$$C_d = \frac{V_{PD}^2}{k_{sys}} \left(\frac{\partial C}{\partial x}\right)^2$$
$$L_d = \frac{k_{sys}}{\omega_r^2 V_{PD}^2 \frac{\partial C}{\partial x}}$$
$$R_d = \frac{k_{sys}}{\omega_r Q V_{PD}^2 \frac{\partial C}{\partial x}}.$$
$$\phi_s = \frac{V_{PS}\left(\frac{\partial C}{\partial x}\right)_s}{V_{PD}\left(\frac{\partial C}{\partial x}\right)_d}$$

Figure 2.5. Equivalent circuit with element equations for the electrostatic-comb driven lateral microresonator biased as in Fig. 2.1(b), i.e. with sense-port grounded.

sense port, respectively. For the general case, assuming uniform shuttle thickness, $\left(\frac{\partial C}{\partial x}\right)_d$ and $\left(\frac{\partial C}{\partial x}\right)_s$ will differ when the gap distance for fingers at the drive port differs from that at the sense port, and/or when the ports differ in number of fingers. Thus, I_x and I_s are related by

$$\phi_s = \frac{I_s}{I_x} = \frac{V_{PS}\left(\frac{\partial C}{\partial x}\right)_s}{V_{PD}\left(\frac{\partial C}{\partial x}\right)_d} \tag{2.27}$$

and the equivalent circuit for the arrangement shown in Fig. 2.1(b) can now be presented as in Fig. 2.5, where a current-controlled current source describes the electrical behavior of the microresonator at the sense port. Note that the sign of Eq. (2.27) will be negative, since the change in finger overlap capacitance for a given change in x will have the opposite sign at the sense port from that at the drive port.

In the general case, the microresonator might be used as a two-port device, where there are excitation signals at both ports, as shown in Fig. 2.6. By symmetry, the equivalent circuit and the corresponding equations defining the elements for this general case are those summarized in Fig. 2.7.

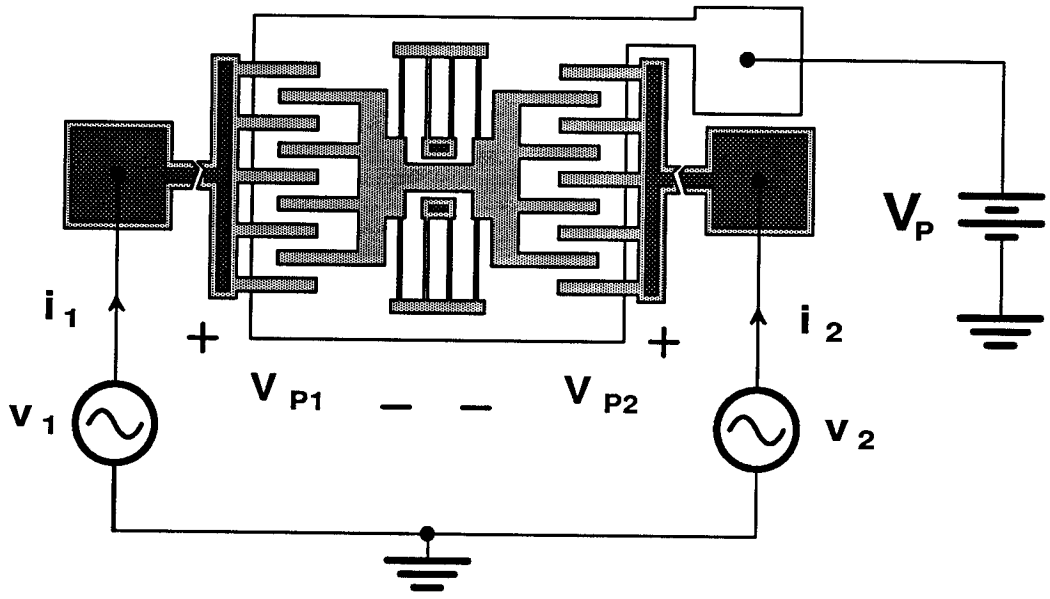

Figure 2.6. General biasing and excitation for a two-port electrostatic-comb driven lateral microresonator.

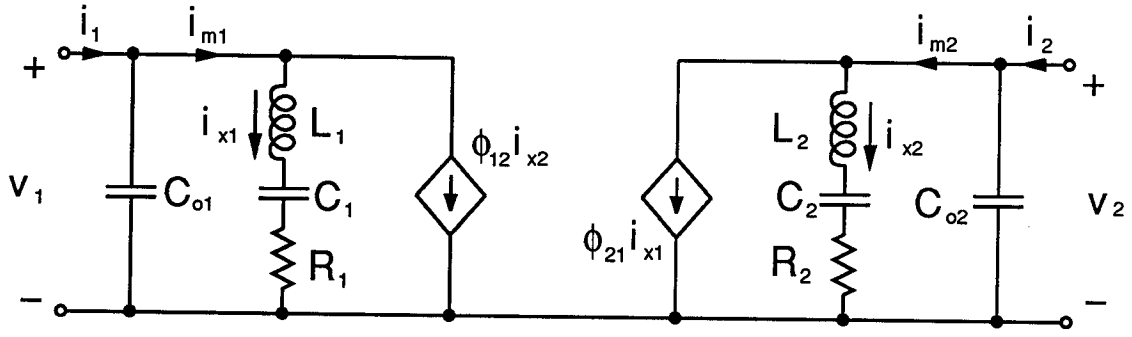

$$C_{o1} = C_{overlap1} \text{ at dc} \qquad C_{o2} = C_{overlap2} \text{ at dc}$$

$$L_1 = \frac{k_{sys}}{\omega_r^2 V_{P1}^2 \left(\frac{\partial C}{\partial x}\right)_1^2} \qquad L_2 = \frac{k_{sys}}{\omega_r^2 V_{P2}^2 \left(\frac{\partial C}{\partial x}\right)_2^2}$$

$$C_1 = \frac{V_{P1}^2}{k_{sys}} \left(\frac{\partial C}{\partial x}\right)_1^2 \qquad C_2 = \frac{V_{P2}^2}{k_{sys}} \left(\frac{\partial C}{\partial x}\right)_2^2$$

$$R_1 = \frac{k_{sys}}{\omega_r Q V_{P1}^2 \left(\frac{\partial C}{\partial x}\right)_1^2} \qquad R_2 = \frac{k_{sys}}{\omega_r Q V_{P2}^2 \left(\frac{\partial C}{\partial x}\right)_2^2}$$

$$\phi_{12} = \frac{V_{P1}\left(\frac{\partial C}{\partial x}\right)_1}{V_{P2}\left(\frac{\partial C}{\partial x}\right)_2} \qquad \phi_{21} = \phi_{12}^{-1} = \frac{V_{P2}\left(\frac{\partial C}{\partial x}\right)_2}{V_{P1}\left(\frac{\partial C}{\partial x}\right)_1}$$

Figure 2.7. Equivalent circuit with element values for the drive and biasing configuration of Fig. 2.6.

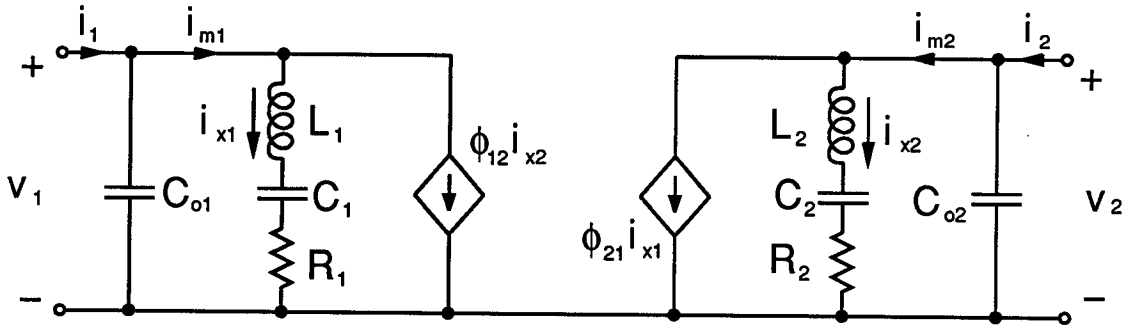

$C_{o1} = C_{overlap1}$ at dc $\quad C_{o2} = C_{overlap2}$ at dc

$L_1 = \omega_r^{-2}[g_1 C_{o1}]^{-1} \quad L_2 = \omega_r^{-2}[g_2 C_{o2}]^{-1}$

$C_1 = g_1 C_{o1}(1 - g_1)^{-1} \quad C_2 = g_2 C_{o2}(1 - g_2)^{-1}$

$R_1 = [g_1 \omega_r C_{o1} Q]^{-1} \quad R_2 = [g_1 \omega_r C_{o1} Q]^{-1}$

$\phi_{12} = \frac{a_1 V_{P1} C_{o1}}{a_2 V_{P2} C_{o2}} \quad \phi_{21} = \phi_{12}^{-1}$

where

$$g_1 = a_1^2 C_{o1} V_{P1}^2 k_{sys}^{-1} d^{-2}$$

$$g_1 = a_2^2 C_{o2} V_{P2}^2 k_{sys}^{-1} d^{-2}$$

Figure 2.8. Small signal (small displacement amplitude) equivalent circuit for a two-port parallel-plate driven and sensed vertical microresonator with circuit element values.

2.1.2 Equivalent Circuit for a Two-Port Parallel-Plate Driven and Sensed Vertical Microresonator

The small signal (and small displacement amplitude) equivalent circuit for a two-port parallel-plate driven and sensed vertical microresonator has been derived by Howe [1] and is summarized in Fig. 2.8. Comparison of Figs. 2.7 and 2.8 shows that electrostatic-comb and parallel-plate resonators have the same small signal equivalent circuits with slight differences in the element values.

In particular, note that the resonance frequency of the parallel-plate driven microresonator can be pulled via changing the dc bias V_P. This feature arises from a nonlinearity in the excitation voltage-to-drive force transfer function, given in phasor form (for small vibration amplitude) by [1]:

$$F_d(j\omega) = -C_o d^{-1} V_P V_d(j\omega) + C_o d^{-2} V_P^2 X(j\omega) \tag{2.28}$$

where $X(j\omega)$ is the average deflection of the center portion of the bridge, and the other parameters are given in Fig. 2.1(a). The corresponding transfer function for electrostatic-comb driven microresonators, given above by Eq. (2.14), is linear, and thus, this particular frequency pulling feature is not available for these resonator types[7].

2.1.3 Equivalent Circuit for One-Port Microresonators

Typical biasing and excitation configurations for microresonators used as one-port devices are shown in Figs. 2.9(a) and (b) for electrostatic-comb and parallel-plate driven microresonators, respectively. The equivalent circuit for one-ports follows directly from the analysis of Section 2.1.1 and is shown with appropriate element values in Fig. 2.10.

2.2 Transconductance Spectrum as Predicted Via the Equivalent Circuit

To make more concrete the above equivalent circuits, let us obtain expressions for the equivalent circuit of a two-port electrostatic-comb driven lateral microresonator with the assumption that capacitance due to fringing fields between interdigitated fingers can be neglected. With this assumption we obtain the following expression for the total finger overlap capacitance at port 1 as a function of x:

$$C_1(x) = \frac{2N_1\varepsilon_o h(L_1 + x)}{d_1} \tag{2.29}$$

where N_1 is the number of shuttle fingers on the port 1 side, ε_o is the permittivity in vacuum (or air), and the dimensions h, L_1, and d_1 are given in Fig. 2.2 (with L_1 replacing L_o and d_1 replacing d). Differentiating with respect to x, we obtain

$$\left(\frac{\partial C}{\partial x}\right)_1 = \frac{2N_1\varepsilon_o h}{d_1}. \tag{2.30}$$

The corresponding expression for $\left(\frac{\partial C}{\partial x}\right)_2$ at port 2 has the same form with N_1 replaced by N_2 and d_1 replaced by d_2.

[7]Frequency pulling via a change in bias can be implemented for electrostatic-comb types with some sacrifice in the linearity of the voltage-to-current transfer function. This can be implemented by putting a gradient on some of the comb-finger edges, making the effective capacitance somewhat nonlinear with displacement.

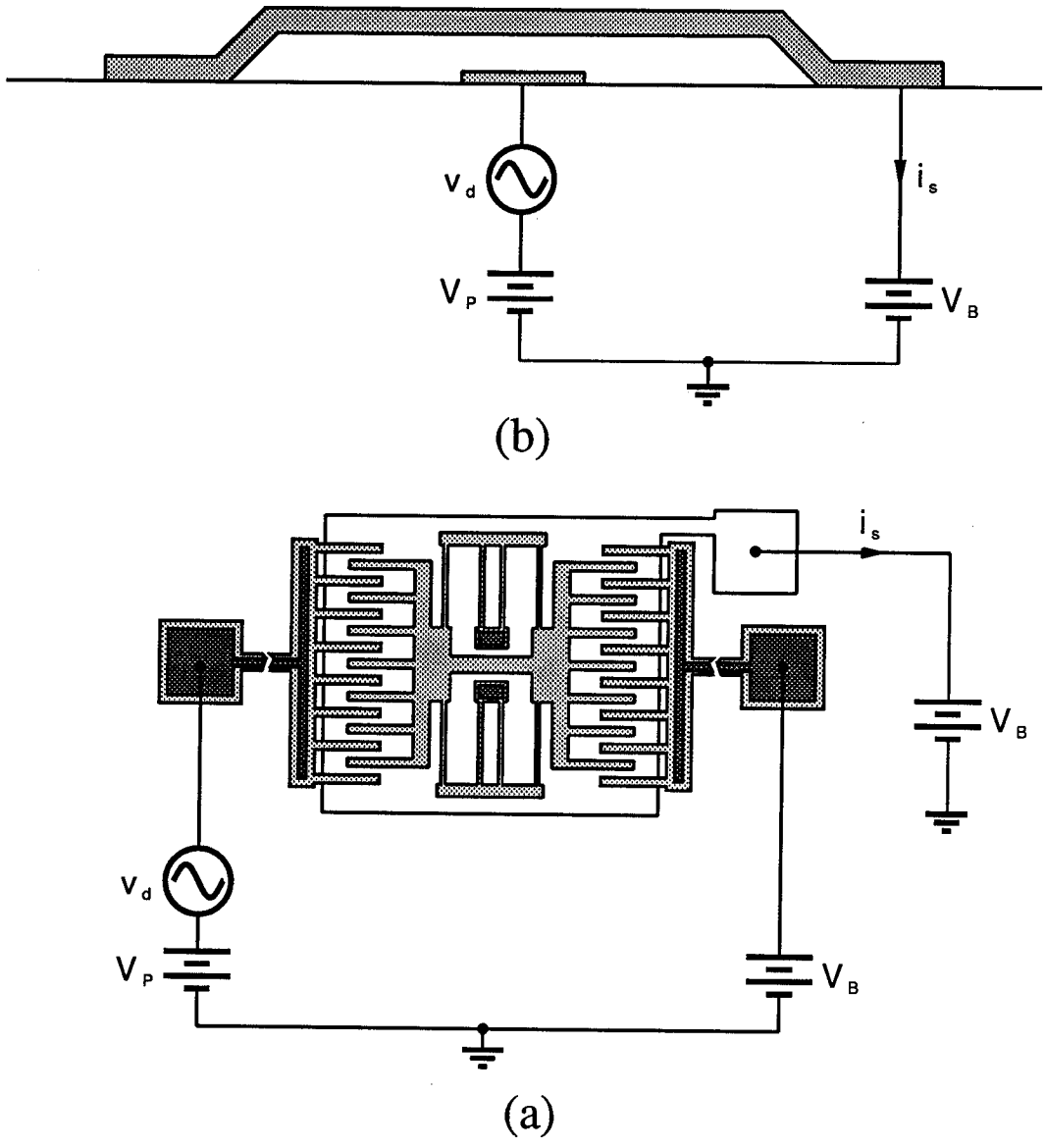

Figure 2.9. Typical bias and excitation configurations for one-port operation for (a) a two-port electrostatic-comb driven microresonator and (b) a one-port parallel-plate driven microresonator.

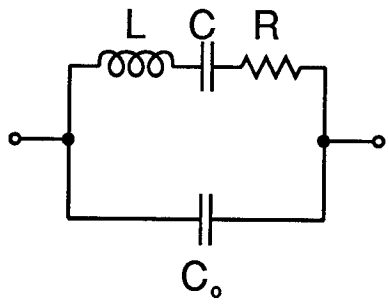

Parallel-plate	**Electrostatic-comb**
$C_o = C_{overlap}$ at dc	$C_o = C_{overlap}$ at dc
$L_1 = \omega_r^{-2}[g_1 C_{o1}]^{-1}$	$L_1 = \frac{k_{sys}}{\omega_r^2 V_{PD}^2 \frac{\partial C}{\partial x}}$
$C_1 = g_1 C_{o1}(1-g_1)^{-1}$	$C_1 = \frac{V_{PD}^2}{k_{sys}}\left(\frac{\partial C}{\partial x}\right)^2$
$R_1 = [g_1 \omega_r C_{o1} Q]^{-1}$	$R_d = \frac{k_{sys}}{\omega_r Q V_{PD}^2 \frac{\partial C}{\partial x}}$

Figure 2.10. General equivalent circuit for microresonators operated as one-ports. The a_1 and a_2 model the fact that average deflection over the electrodes is used in the derivation [1].

Given the expressions for $\left(\frac{\partial C}{\partial x}\right)_1$ and $\left(\frac{\partial C}{\partial x}\right)_2$, the elements for the equivalent circuit of a two-port electrostatic-comb lateral microresonator, shown in Fig. 2.7, are summarized below:

$C_{o1} = \frac{2N_1\varepsilon_o h L_1}{d_1}$	$C_{o2} = \frac{2N_2\varepsilon_o h L_2}{d_2}$
$L_1 = \frac{k_{sys}}{4}\left[\frac{d_1}{\omega_r N_1 \varepsilon_o h V_{P1}}\right]^2$	$L_2 = \frac{k_{sys}}{4}\left[\frac{d_2}{\omega_r N_2 \varepsilon_o h V_{P2}}\right]^2$
$C_1 = 4k_{sys}^{-1}\left[\frac{N_1\varepsilon_o h V_{P1}}{d_1}\right]^2$	$C_2 = 4k_{sys}^{-1}\left[\frac{N_2\varepsilon_o h V_{P2}}{d_2}\right]^2$
$R_1 = \frac{k_{sys}}{4\omega_r Q}\left[\frac{d_1}{N_1\varepsilon_o h V_{P1}}\right]$	$R_2 = \frac{k_{sys}}{4\omega_r Q}\left[\frac{d_2}{N_2\varepsilon_o h V_{P2}}\right]$
$\phi_1 = \frac{d_2 N_1 V_{P1}}{d_1 N_2 V_{P2}}$	$\phi_2 = \phi_1^{-1} = \frac{d_1 N_2 V_{P2}}{d_2 N_1 V_{P1}}$

At resonance, the motional current of the microresonator is determined by the value of the equivalent resistance R; detectable motional current is maximized when R is minimized for the port involved. From the above equations, R can be minimized by maximizing the number of fingers N, the thickness h, the quality factor Q, and the effective bias voltage V_P, and minimizing the interdigitated finger gap d and the system spring constant k_{sys}.

Let us take for a numerical example, an electrostatic-comb driven and sensed lateral microresonator with the following parameters:

$$
\begin{array}{ll}
N_1 = N_2 = 12 & E = 150\text{GPa} \\
d_1 = d_2 = 2\ \mu\text{m} & W = 2\ \mu\text{m} \\
L_{o1} = L_{o2} = 20\ \mu\text{m} & L = 200\ \mu\text{m} \\
M_p = 4.468 \times 10^{-11}\ \text{kg} & M = 1.803 \times 10^{-11}\ \text{kg} \\
h = 2\ \mu\text{m} &
\end{array}
$$

where W and L are the length and width of the supporting beams, respectively, h is the thickness, E is the Young's modulus, and M_p and M are the masses of the plate and of the supporting beams, respectively. The other parameters have been summarized before in Fig. 2.2.

Typical biasing and excitation voltages for the above microresonator are as follows (refer to Fig. 2.1(b)):

$$
\begin{aligned}
V_P &= 80\ \text{V} \\
|v_d| &= 10\ \text{V}
\end{aligned}
$$

The parameters necessary for determination of equivalent circuit elements may be predicted using Eqs. 2.16 through 2.19. From these equations, $k_{sys} = 0.6$ N/m, $\omega_r = 17.2$ kHz, and $Q = 59$. As mentioned previously, this calculated value of Q overshoots the actual value significantly, and thus, a measured value of $Q = 27$ will be used. For this example, the elements of the equivalent circuit are now calculated to be:

$$
\begin{array}{ll}
C_{o1} = 4.25\ \text{fF} & C_{o2} = 4.25\ \text{fF} \\
L_1 = 1.78 \times 10^5\ \text{H} & L_2 = 1.78 \times 10^5\ \text{H} \\
C_1 = 4.82 \times 10^{-16}\ \text{F} & C_2 = 4.82 \times 10^{-16}\ \text{F} \\
R_1 = 7.12 \times 10^8 & R_2 = 7.12 \times 10^8 \\
\phi_1 = -1.0 & \phi_2 = -1.0
\end{array}
$$

The circuit elements are the same on both ports since the microresonator is symmetrical.

Simulation via SPICE3 using the above equivalent circuit elements for a microresonator biased and excited as in Fig. 2.1(b) yields the $Y_d(j\omega) = I_s(j\omega)/V_d(j\omega)$ spectrum shown in Fig. 2.11. This response is typical.

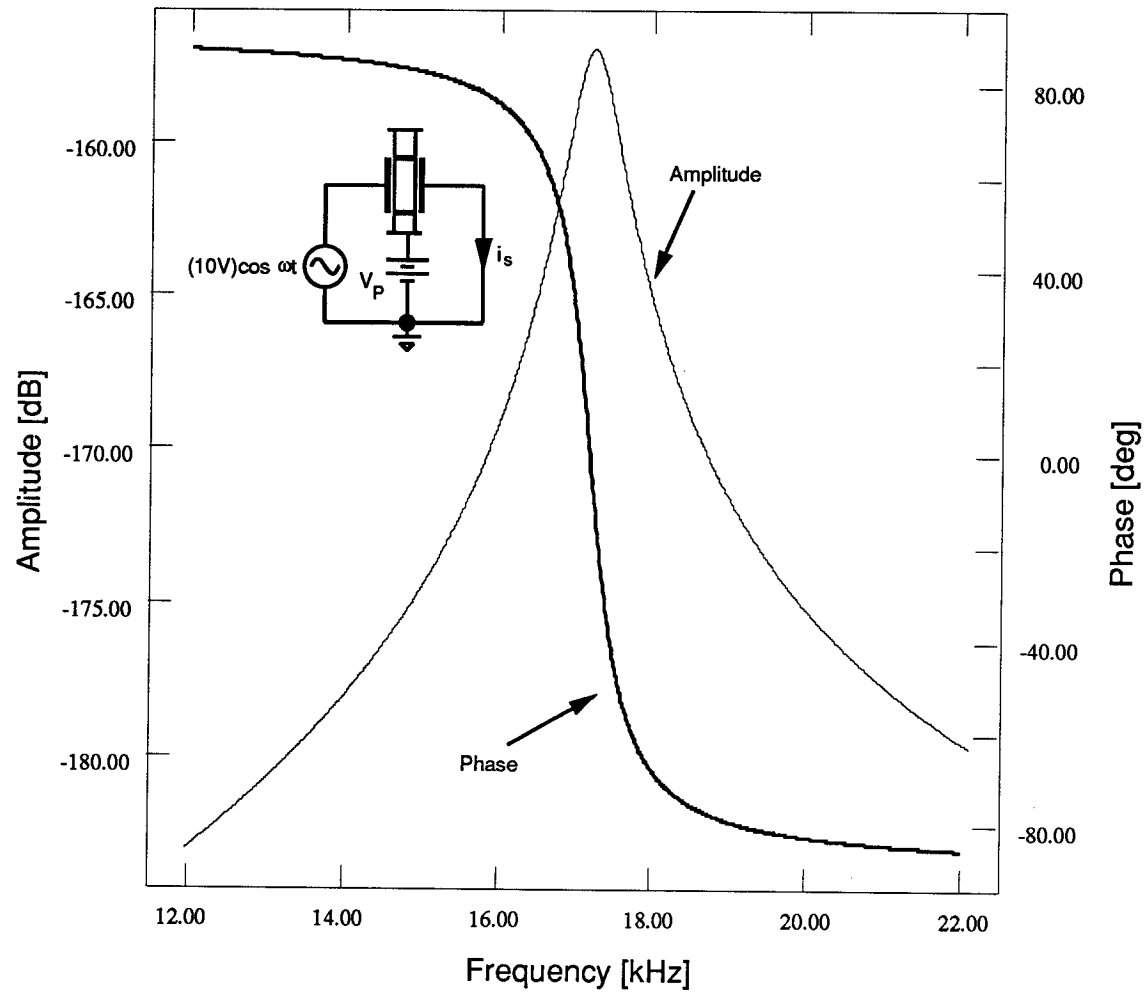

Figure 2.11. Transconductance spectrum for an electrostatic-comb driven microresonator biased as in Fig. 2.1(b) as predicted by its equivalent circuit model.

2.3 Design Parameters of Interest and the Need for a Convenient Characterization Technique

Design of microresonators for use in circuit applications requires accurate determination of the aforementioned equivalent circuits. This, in turn, requires accurate determination of electromechanical characteristics, such as resonance frequency, quality factor, $\frac{\partial C}{\partial x}$, and both electrical and mechanical noise as seen in output currents. For many cases, simple theoretical models are not adequate for accurate determination of equivalent circuit elements.

For example, the expressions given by Eqs. (2.29) and (2.30), which neglect the ca-

pacitance contributions due to fringing electric fields, although qualitatively accurate, are not adequate for correct determination of $\frac{\partial C}{\partial x}$ (and thus, determination of equivalent circuit elements) for many cases. As an example, for a microresonator with a finger gap $d = 2\ \mu$m and thickness $h = 2\ \mu$m, Eq. (2.30) undershoots the measured value by more than 40 %.

Furthermore, the peak value of output current at resonance (and thus, the equivalent resistance) for any given microresonator depends heavily upon second order effects, which are difficult to model precisely and which may depend strongly upon microresonator design. An excellent example of this is the strong dependence of peak current on the type of microresonator ground plane. This dependence is caused by levitation of the microresonator shuttle structure due to a ground plane-induced imbalance of vertically directed electrostatic forces [11]. The amount of levitation determines the finger overlap capacitance, which in turn determines the value of $\frac{\partial C}{\partial x}$.

Thus, experimental techniques for measurement of $\frac{\partial C}{\partial x}$ are necessary. As will be seen, use of a striped ground plane, instead of a uniform one, suppresses levitation and increases the peak microresonator current at resonance, thus, decreasing the series resistance of the microresonator. The importance of an accurate knowledge of series resistance in a microresonator is paramount for design of a microresonator oscillator, since series resistance determines the amount of gain required by the sustaining amplifier. Inaccurate formulas are not adequate in this case, and again, the need for accurate experimental determination of R_s is stressed.

Similar examples follow for resonance frequency, quality factor, and electrical and mechanical noise, all important for microresonator circuit design.

To characterize microresonators for circuit applications, a technique which directly measures the *electrical* parameters of a microresonator is a *must*. An optical technique, as described in Chapter 1, is no substitute. The characterization technique must not only be *electrical*, but it must be convenient to use. Specifically, it should be operable at a wafer-level probe station and should utilize only off-chip electronics. In other words, for characterization of a microresonator, one should be required to fabricate only the microresonator, and not any on-chip electronics, which could double or triple the necessary integrated circuit processing time.

The remaining chapters in this report detail the problems with achieving such a characterization technique, successful implementations, and examples of their application to

microresonator design for circuits.

3.0 PARASITIC FEEDTHROUGH INTERFERENCE

Implementation of a convenient, off-chip, open-loop microresonator characterization technique is a challenging task mainly because of parasitic feedthrough currents which can mask the relatively tiny motional current of a microresonator. These parasitic currents arise mostly from probe-to-probe capacitive feedthrough and substrate capacitance and make the direct experimental detection scheme shown in Fig. 3.1 infeasible for cases where the drive voltage amplitude must be larger than a few millivolts. This chapter will investigate parasitic feedthrough and the restrictions it imposes on sense current detection schemes.

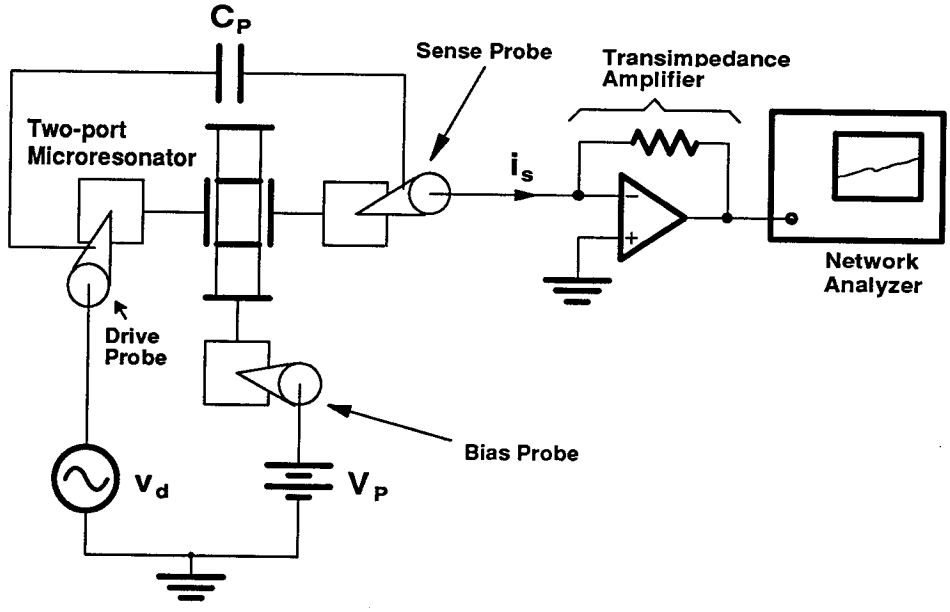

Figure 3.1. Experimental set-up for direct off-chip detection of microresonator motional current. This detection strategy is ineffective when drive voltages larger than a few millivolts are required because of interference from probe-to-probe parasitic feedthrough. (Here, the circuit symbol for a two-port microresonator, which readily corresponds to the drawing in Fig. 2.1(b), is used.)

3.1 Intrinsic DC Capacitance in One-port Microresonators

In the previous chapter, the transconductance spectrum of a two-port electrostatic-comb driven lateral microresonator was plotted under ideal conditions where all parasitic feedthrough was neglected. A pure series resonance spectrum was obtained (Fig. 2.11). It is instructive to compare the spectrum under similar (ideal) conditions for a one-port microresonator, which has an intrinsic dc capacitance in its equivalent circuit.

For this purpose, let us take a parallel-plate driven vertical microresonator with the following typical dimensions (refer to Fig. 2.1(a)):

length of bridge (L): 160 μm
width of bridge (W): 20 μm
thickness (h): 1.275 μm
width of driving electrode (L_d): 10 μm
distance between bridge and driving electrode (d): 2.1 μm

Let us operate the microresonator in vacuum (assume $Q = 10^4$) with a 20 V dc bias. Using the expressions in Fig. 2.10 of the previous chapter, the equivalent circuit elements for the above microresonator may be summarized as follows:

$$C_o = 0.843 \text{ fF}$$
$$C = 1.015 \times 10^{-18} \text{ F}$$
$$L = 1.454 \times 10^5 \text{ H}$$
$$R = 37.8 \text{ M}$$

The transconductance spectrum for this one-port microresonator is presented in Fig. 3.2. The spectrum contains both a series and a parallel resonance brought on by the intrinsic dc capacitance C_o in parallel with the series LCR in the equivalent circuit.

For characterization purposes, the spectrum of Fig. 3.2 has limited applicability. For instance, because of C_o, the series resonance frequency shown in Fig. 3.2 is shifted downward slightly from the actual mechanical resonance frequency. Furthermore, because of the distortion, the quality factor of the microresonator cannot be accurately determined from Fig. 3.2. A pure series resonance spectrum would yield the mechanical series resonance frequency and the quality factor much more conveniently and accurately. Thus, the most desirable characterization scheme should be able to eliminate even the intrinsic dc capacitance in a microresonator.

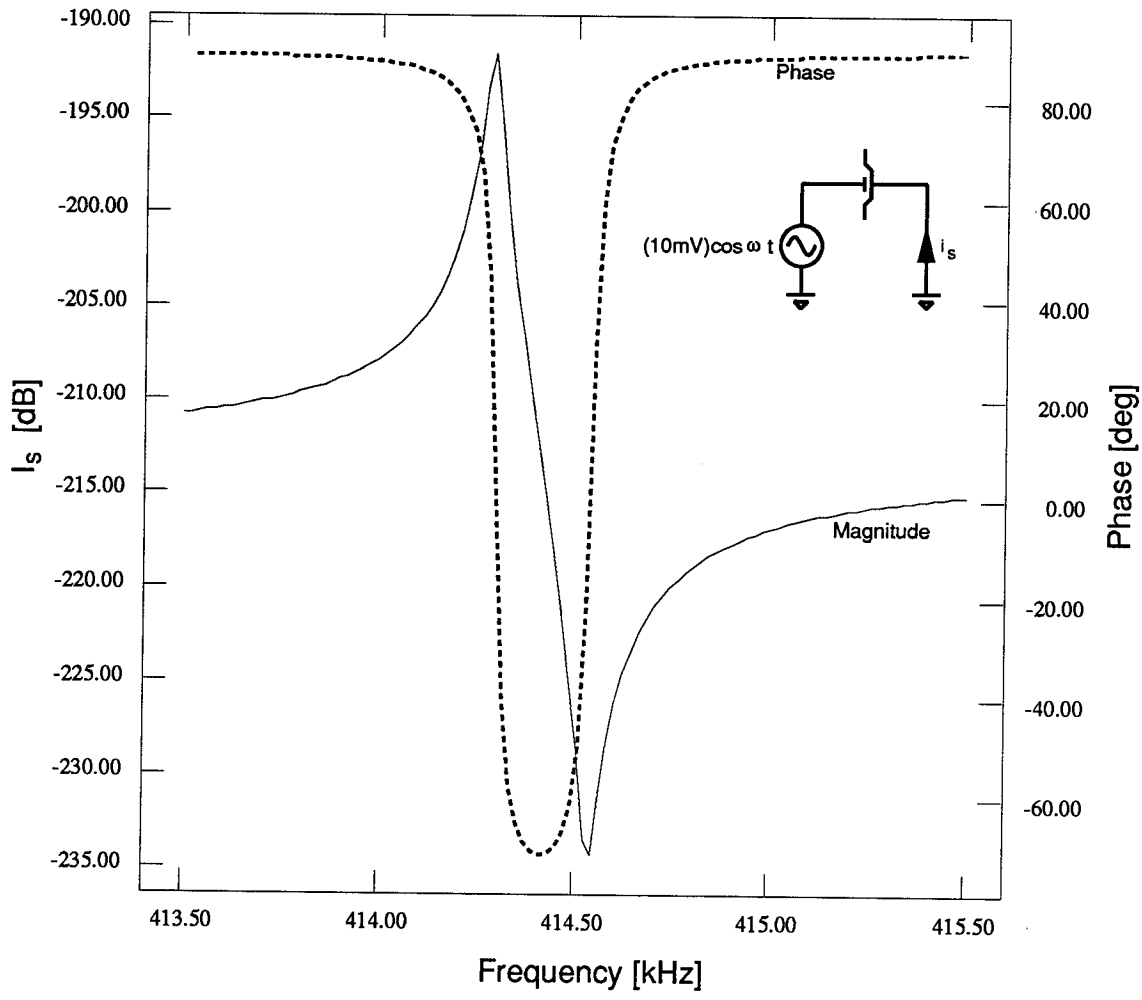

Figure 3.2. Simulated transconductance spectrum for a one-port parallel-plate driven microresonator.

3.2 Probe-to-probe Parasitic Feedthrough

In the previous section, the intrinsic dc capacitance of one-port microresonators was found to yield a transconductance spectrum distorted from pure series resonance. However, in the previous *chapter*, a two-port microresonator was found to provide a pure series resonance transconductance spectrum if its sense port is grounded. Thus, if an indirect measurement of sense current for a one-port microresonator is acceptable, the solution to the distorted series resonance problem seems to be as simple as just fabricating two-port microresonators for characterization purposes. Unfortunately, for an *off-chip* measurement scheme, the dc capacitance that causes the distortion is unavoidable even for multi-port mi-

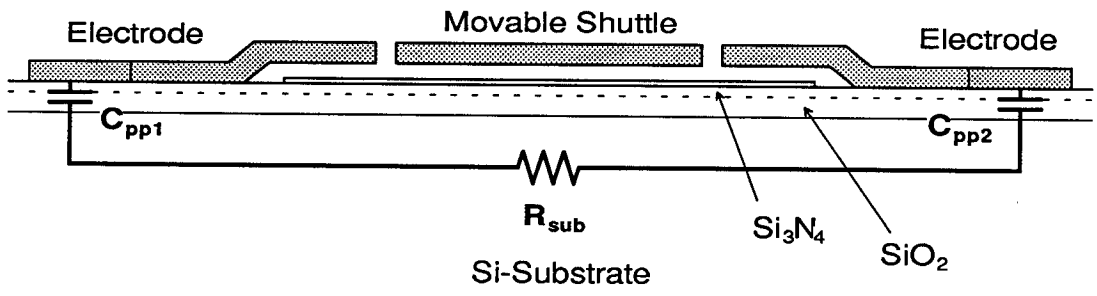

Figure 3.3. Schematic of the elements modelling substrate parasitics which contribute to the distortion of the microresonator transconductance spectrum.

croresonators.

Probe-to-probe and substrate parasitics are the culprits, here, and in general, these sources contribute the majority of the parasitic dc capacitance in off-chip detection schemes. Typical values for probe-to-probe capacitance are 30 fF for unshielded tungsten probes and 2 fF for coaxial probes. Note that these parasites are generally larger than the variation in capacitance of an oscillating microresonator, which is usually on the order of one femtofarad or less.

Substrate parasitics can be modelled by a series combination of the input-to-output substrate resistance R_{sub} and the pad-to-substrate parasitic capacitance at both ports, C_{pp1} and C_{pp2}, as shown schematically in Fig. 3.3. The degree to which substrate parasitics contribute to series resonance distortion depends upon the conductivity of the substrate. If the substrate is not doped, then R_{sub} is large and the current feeding through the substrate is quite small. In terms of an effective capacitance (for simplicity), measurements for the undoped substrate case indicate that $C_{eff} \approx 0.2$ fF. If the substrate is doped and unbiased (not grounded), R_{sub} is much smaller, and the measured effective capacitance is $C_{eff} \approx 2$ fF. Thus, if a $POCl_3$ substrate diffusion is included in the process sequence for microresonator fabrication, electrical access to the substrate must be insured to minimize substrate parasitics.

Distortion of the pure series resonance spectrum as a function of capacitance in parallel with a microresonator is depicted in Fig. 3.4. The figure shows that as the dc capacitance increases, the series resonance of the microresonator gradually fades to a point where the

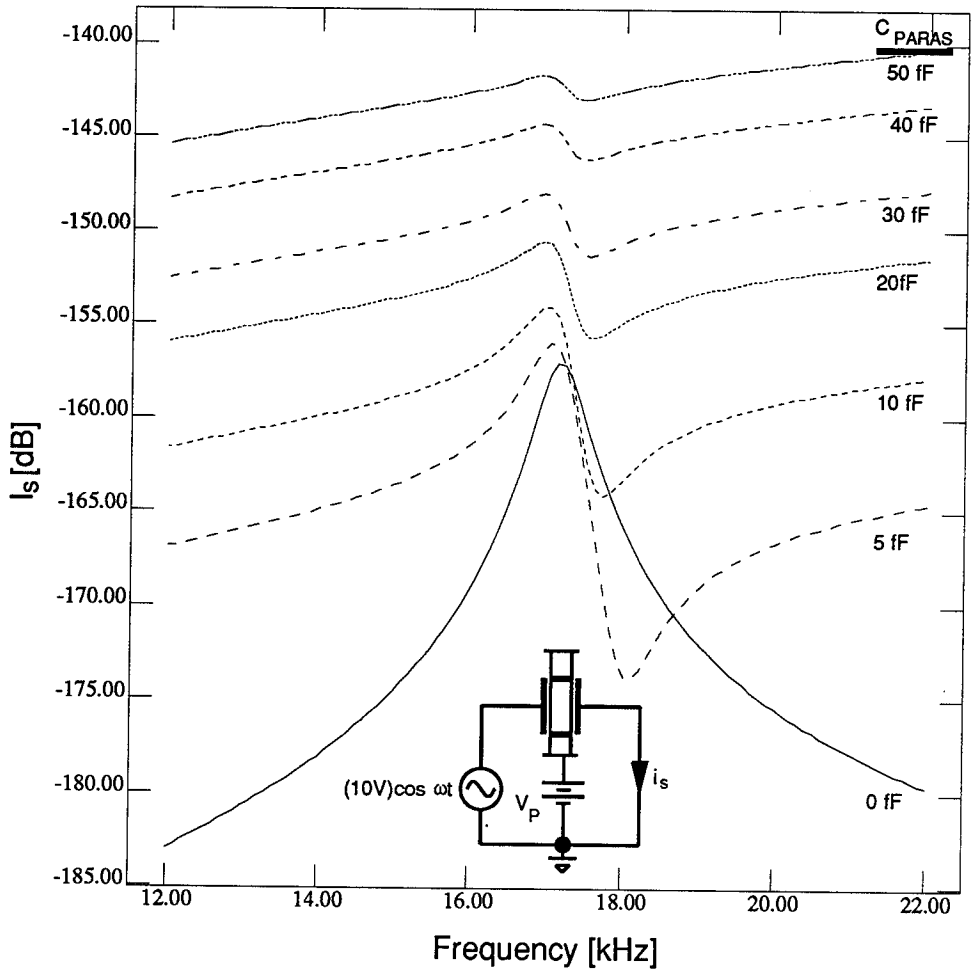

Figure 3.4. Plot of the transconductance spectrum for the two-port microresonator of Section 2.2 and Fig. 3.1 as a function of the capacitance in parallel with the microresonator. This plot models the effect of increasing parasitic capacitance between the drive and sense ports. ($V_P = 80$ V, $|v_d| = 10$ V)

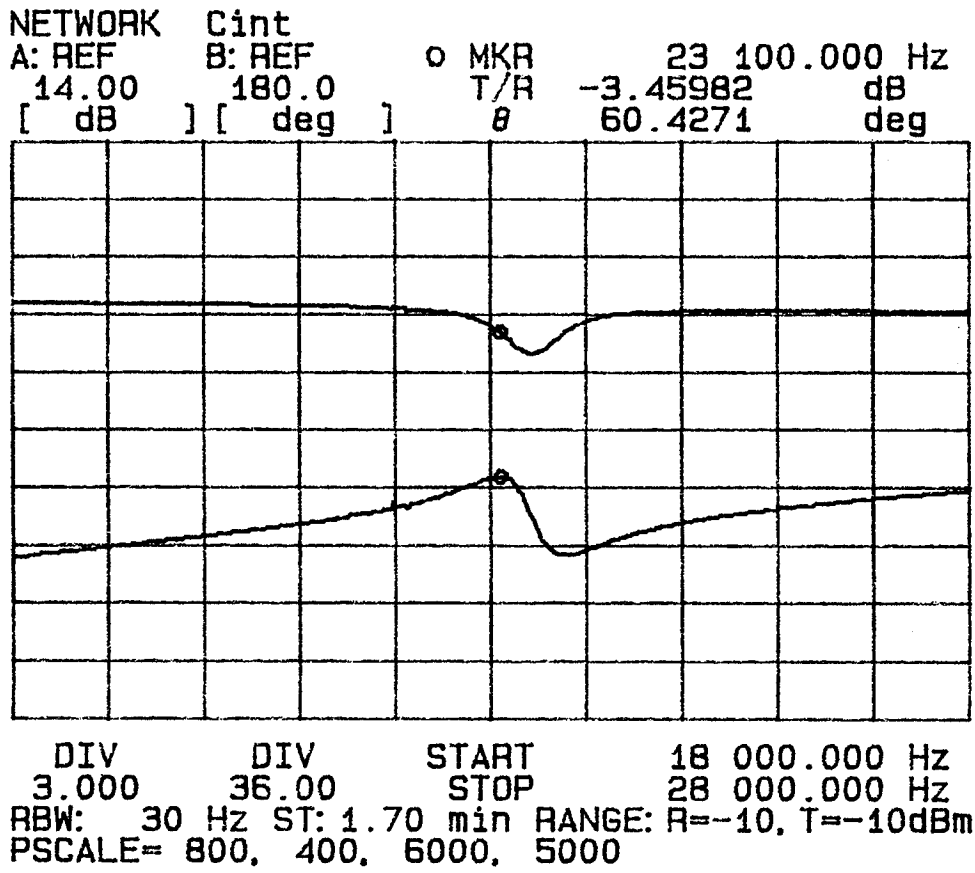

Figure 3.5. Direct measurement (as in Fig. 3.1) of the transconductance spectrum for a microresonator fabricated to the specifications of the example in Chapter 2. ($V_P = 80$ V, $|v_d| = 10$ V)

resonance frequency is no longer discernible; the usefulness of the transconductance spectrum for characterization purposes fades as the dc capacitance increases.

An experimentally measured transconductance spectrum using the direct technique of Fig. 3.1 is shown in Fig. 3.5. Note that in this spectrum the distortion makes Q difficult to extract and shifts the series resonance frequency from that of pure series resonance. In addition, it is obvious that the performance of microresonator systems—in particular, of microelectromechanical filters—will be altered if the direct measurement technique is used.

3.3 Surface Leakage

In addition to probe-to-probe and substrate parasitics, surface leakage can have an even greater distorting contribution. The measured transconductance spectra for microresonators taken out of an oily vaccum environment indicate an effective parasitic capacitance C_{eff} of over 40 fF. To guard against this, microresonator wafers should be appropriately cleaned and dehydrated at the completion of processing.

3.4 Dependence of Feedthrough on Drive Voltage Amplitude

The degree to which parasitic feedthrough masks motional current, causing distortion, is a function of the voltage required to drive the microresonator (as well as the amount of parasitic capacitance), and thus, is a function of the transconductance $\frac{I_s}{V_d}$ of the system. The magnitude of the transconductance at resonance of a dc-biased electrostatic-comb driven lateral microresonator with sense port grounded can be obtained from Eq. 2.26:

$$|\frac{I_s}{V_d}| = \omega_r V_P^2 \frac{Q}{k_{sys}} \left(\frac{\partial C}{\partial x}\right)_d \left(\frac{\partial C}{\partial x}\right)_s \propto V_P^2 \frac{Q}{\sqrt{k_{sys}}} \left(\frac{\partial C}{\partial x}\right)_d \left(\frac{\partial C}{\partial x}\right)_s \tag{3.1}$$

Equation (3.1) reveals that Q, V_P, k_{sys}, and $\frac{\partial C}{\partial x}$ determine the voltage amplitude required to drive the device into resonance. Of these three, Q is most easily changed (by simply changing the operation pressure) over the largest range of values (5 to 100,000 or more). For very high vacuum operation, where ac drive voltages as small as 1 mV in amplitude might suffice, the motional current of a microresonator might be detected directly. However, as the Q goes down, and the required ac voltage becomes larger, motional current masking quickly makes *direct* off-chip detection of resonance difficult.

An idea of the voltage magnitude threshold allowing detection by direct methods (Fig. 3.1) for the example microresonator of Chapter 2 is provided by the simulated plot of Fig. 3.6 comparing the motional current (without parasitics) with the parasitic currents resulting from varying values of $|v_d|$. For acceptable distortion, the parasitic current component should be at least 50 dB below the motional current peak value [1]. From the plot,

[1]Note that this 50 dB value is somewhat arbitrarily selected, and values as high as 30 dB down might suffice, depending upon the application. A parasitic component 50 dB below the motional current peak value for the case of Fig. 3.6 would have a parallel resonant peak at 60 kHz. This is far enough away from the series resonance to suppress Q-distortion sufficiently. However, the presence of the parallel resonant peak

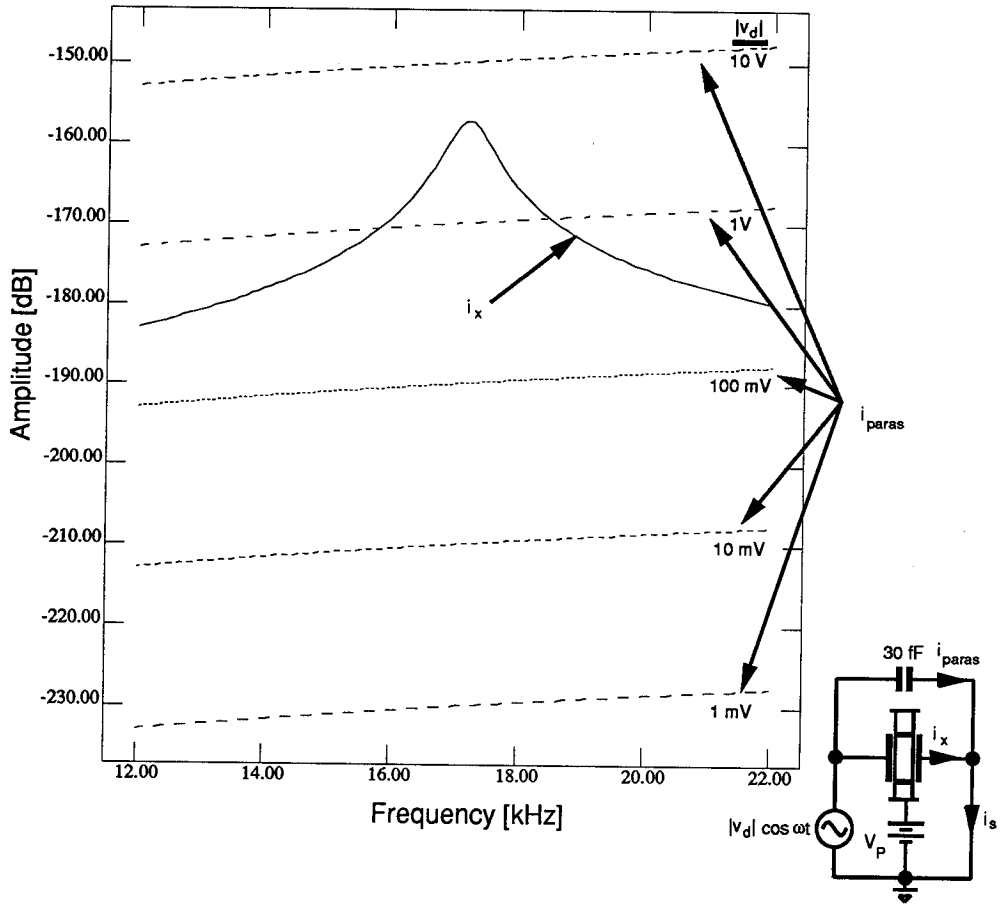

Figure 3.6. Simulated plot of parasitic feedthrough current (C_{paras} = 30 fF) as a function of frequency and drive voltage amplitude, $|v_d|$. Also shown for reference, is the microresonator motional current without parasitics for a displacement amplitude of 10 μm. (V_P = 80 V)

ac voltage amplitudes on the order of millivolts define the the threshold whereby motional current can be measured with acceptable interference from probe-to-probe parasitics, and spectra similar to that of Fig. 2.11 can be obtained. Again, millivolt drive voltages can be achieved by raising the system Q for low frequency ($f_r \approx 20$ kHz) microresonators.

For many applications, however, the microresonator will be designed for drive voltages much larger than millivolts in order to suppress the effects of noise. For these cases, and for the case of one-port microresonators, which will always suffer from distortion due to intrinsic dc parasitic capacitance (no matter the drive voltage amplitude), a detection technique which nulls dc capacitance is required.

3.5 Requirements for an Electromechanical Characterization Technique

In Chapter 1, a previously used direct measurement technique involving cautious and tedious minimization of parasitic dc capacitance via special packaging and bonding was discussed. This approach, however, is actually only useful for vacuum conditions, where only small voltage amplitudes are required for excitation of resonance. Under low-Q environments, the technique becomes useless. This coupled with the tedious packaging requirements of the technique make it undesirable.

It is evident that any direct characterization technique will suffer from probe-to-probe parasitic feedthrough interference if reasonable drive voltages are necessary. The most promising approach for implementation of a convenient, repeatable, open-loop, off-chip, *electrical* characterization method would seem to require an indirect approach; one which avoids the complications of feedthrough interference by *separating* motional current from the interfering parasitics. The following chapters of this report detail techniques for such separation in both the time domain and the frequency domain.

---

might interfere with the performance of some systems. For parasitics 70 dB down, the parallel resonance is at 170 kHz. The smaller $|v_d|$, the farther away the parallel resonance, and the less the local distortion.

4.0 GATED-SINUSOID EXCITATION AND DETECTION (GSED)

The high quality factor Q of microresonators in vacuum makes time domain separation of microresonator motional current from parasitic feedthrough components feasible. The basic approach to implementing such a separation scheme attempts to detect motional current during periods where the voltage signal exciting resonance is turned off. Since continued oscillation of the microresonator during zero-input is required, medium- to high-Q operation of the microresonator in vacuum is necessary.

This chapter describes a technique for determining resonance frequency and approximate motional current amplitude, in which a microresonator is excited in vacuum via a gated sinusoid, and motional current from the oscillating microbridge is detected by open-loop, off-chip, electronic instrumentation during the zero-input period of the excitation signal. The net effect is isolation of microresonator motional current during detection periods and a consequent elimination of all dc capacitance, even the intrinsic dc capacitance of one-port microresonators. Only ac (motional) capacitance is measured.

4.1 The Gated-Sinusoid Excitation and Detection (GSED) Experimental System

A schematic of the experimental set-up for the gated-sinusoid excitation and detection scheme (GSED) is shown in Fig. 4.1. Although the figure depicts the system for a two-port microresonator, only one port is necessary.

The GSED technique is very much instrumentation dependent, and thus, a description of its implementation must include a description of required equipment. For the experiment of this report, the excitation signal was provided by an HP 3314A function generator operating in gated mode, in which a pulsed sinusoid with a 50% duty cycle and adjustable pulse period (sweep/trigger interval) is generated as shown in Fig. 4.1.

The trigger signal in the figure, also generated by the function generator, dictates the periods in which the spectrum analyzer accepts input. The HP 3314A can conveniently

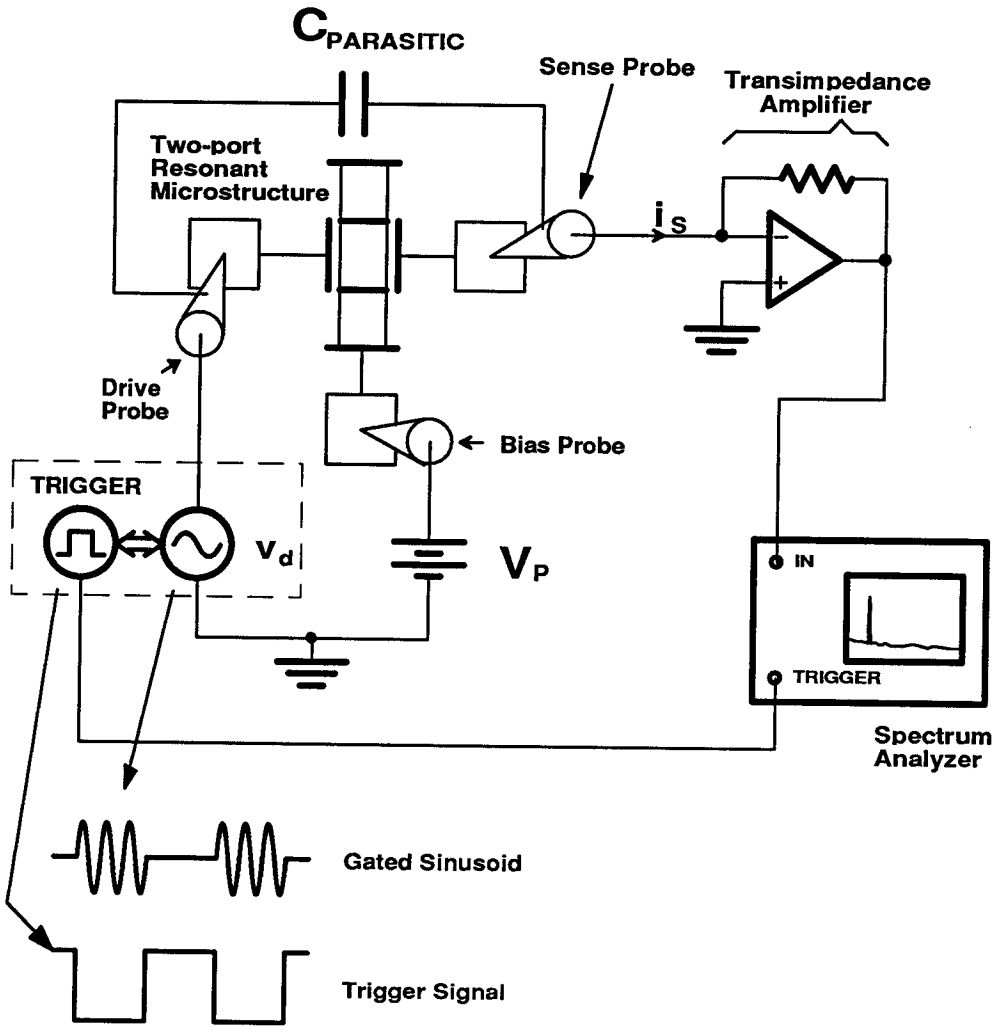

Figure 4.1. Schematic of the experimental set-up for detection of microresonator resonance frequency and quality factor using the gated-sinusoid excitation and detection scheme (GSED).

provide a square wave with the same period as the gated-sinusoid and with rising edge at the start of each zero-input segment of the excitation signal. This signal can then be used to trigger the spectrum analyzer such that it accepts input only during the zero-input phase of the excitation signal. The period (sweep/trigger interval) chosen for this report was 105 milliseconds, although any interval greater than twice the spectrum analyzer sweep time T_s and avoiding breaks in the displayed Fourier spectrum (which occur when the HP 3314A sweep/trigger interval is too small) would be sufficient.

Experimentally, the microresonators under test were placed in vacuum to achieve the

high Q's necessary for continued oscillation of the structures during zero-input. As shown in Fig. 4.1, the gated sinusoid on top of a dc-bias (which is required for detectable current levels and for force amplification) is applied to the driving probe. Microbridge motional current, separated from feedthrough in the time domain, is sensed by the sense probe and directed to a current-to-voltage amplifier, the output of which is fed to the input of a triggered spectrum analyzer. (The amplifier used for the results of this report had a transimpedance amplification of 10^6 and a bandwidth of 600 kHz.)

A spectrum analyzer is used for detection, because the required current-to-voltage amplification is large enough to amplify even stray signals, and these signals can be amplified to proportions larger than the amplified microbridge current. If a time domain instrument, such as an oscilloscope, were used to view the output signal, the motional signal would be accompanied by these stray signals, and the oscilloscope would display a very cluttered picture, in which the dampened sinusoid due to the microresonator motional current would be indistinguishable. On the other hand, since the frequencies of the stray signals are usually different from the signal of interest, a spectrum analyzer can separate the signals and allow easy viewing of the resonance peak.

4.2 Theory of Analog Spectrum Analysis

If one uses a real-time spectrum analyzer, such as the HP 3561A, to implement EAM, then the user need not be concerned with such settings as sweep time and resolution bandwidth. However, most real-time spectrum analyzers do not have the frequency range necessary for some microresonator applications, and thus, one might be forced to use an analog spectrum analyzer. In this case, to most effectively use the GSED scheme the user should have some knowledge of analog spectrum analyzer operation.

An analog spectrum analyzer obtains the magnitude of a signal's Fourier spectrum at a certain frequency by filtering the signal with a sharp filter centered at that frequency. The output of this filter is directed to an envelope detector, and then to a low-pass filter (averager). This system produces a value proportional to the Fourier transform $X(f)$ of the signal at the frequency f of the filter. A schematic showing the system is shown in Fig. 4.2.

Figure 4.2. Schematic of the operation of a swept-filter analog spectrum analyzer.

A typical spectrum analyzer has the equivalent of one tunable filter, which is swept across the frequency range of interest [1] obtaining a complete spectrum for each sweep. The rate at which this filter can be swept depends, on the time necessary for the system of Fig. 4.2 to reach steady state; the swept analyzer must keep in view any frequency component of $X(f)$ long enough for its effect to reach steady state.

To establish the constraints necessary on the rate of filter sweeping for acceptable spectrum analysis accuracy, we define the following:

$$\begin{aligned} \Delta f &\equiv \text{RESOLUTION BANDWIDTH} \\ B_{LP} &\equiv \text{VIDEO BANDWIDTH} \\ W &\equiv \text{FREQUENCY SPAN} \\ T_s &\equiv \text{SWEEP TIME} \end{aligned}$$

Each frequency component of $X(f)$ remains within the resolution bandwidth of the tunable filter for $\Delta f/(W/T_s)$ seconds. The time necessary for the system of Fig. 4.2 to reach steady state must, therefore, be less than this. The time constant for the tunable filter is given by $1/\Delta f$, and that for the low-pass filter by $1/B_{LP}$. These parameters must satisfy the following equation for proper spectrum analyzer performance [19]:

$$\frac{T_s \Delta f}{W} \gg \frac{1}{\Delta f} + \frac{1}{B_{LP}} \tag{4.1}$$

In addition to the above, another constraint must be accounted for. Due to the serial nature of spectrum processing, the tunable filter of the analyzer can view frequency components for only some of the time. This contradicts a fundamental concept of Fourier analysis, in which the infinite time interval should be investigated for each frequency.

[1] Since tunable filters are difficult to implement, a spectrum analyzer actually has a fixed filter, and a heterodyning procedure is used to sweep the Fourier spectrum of the measured signal across the fixed filter frequency. The relative perspective of a swept filter, however, is an equivalent way to view this and is somewhat easier to grasp.

To avoid excessive errors due to the above, it must be insured that over the finite interval during which the serial analyzer views a frequency component of $X(f)$, the behavior of that component is representative of the behavior of the component over the infinte time interval. If the duration of a "representative interval" is denoted by D, then Eq. (4.1) must be modified to read:

$$\frac{T_s \Delta f}{W} \gg \frac{1}{\Delta f} + \frac{1}{B_{LP}} \gg D \tag{4.2}$$

This equation dictates the range of operation within which an analog spectrum analyzer provides calibrated measurements. In particular, it determines the lower limit on T_s, and thus, sets the lower limit on the Q of a microstructure necessary for study via the GSED technique.

4.3 Resonance Frequency Detection

Detection of resonance comes in the form of the sudden appearance of a peak at the resonance frequency on the spectrum analyzer display when the function generator is swept over the resonance frequency. Figure 4.3 presents a photograph showing the appearance of the resonance peak for a parallel-plate driven vertical microresonator with the same characteristics as those for the one-port microresonator discussed in Chapter 3.

Note how the resonance peak appears at the far left of the (analog) spectrum analyzer display. This was done on purpose. The underlying reason is that for analog spectrum analyzers the amplitude of the peak will be a function of its position on the display. This dependence is due to damping of the oscillation amplitude of a microbridge in resonance during the zero-input portion of the gated sinusoid excitation signal. If a spectrum analyzer frequency range is chosen such that the swept filter of the analyzer reaches the resonance frequency after n milliseconds, then the amplitude of the peak will correspond to that after n milliseconds of damping. Thus, the largest signals are obtained when the time required by the tunable filter to reach the resonant frequency is minimized. Minimizing this time corresponds to minimizing the spectrum analyzer SWEEP TIME and placing the resonance peak as close to the left side of the analyzer display as possible (i.e. as close to the starting sweep frequency as possible). The above suggests that when using an analog spectrum analyzer an approximate calculation of the expected resonant frequency of a microresonator under test should be made before measurement, so a proper starting frequency (just a bit under the resonant frequency) may be chosen for best results.

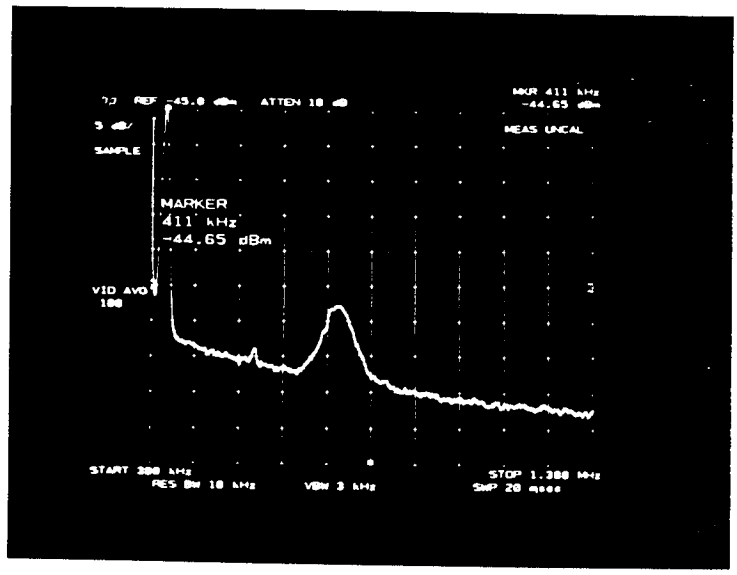

Figure 4.3. Photograph of a spectrum analyzer display showing the resonance peak for a parallel-plate driven vertical microresonator with the same characteristics as those for the one-port discussed in Chapter 3.

If a real-time spectrum analyzer is utilized for GSED, one need not worry about resonance peak placement on the display. The GSED spectrum for a two-port electrostatic comb-driven microresonator obtained using a real-time spectrum analyzer is presented in Fig. 4.4.

A word of caution concerning vacuum operation of microresonators is appropriate at this point. When performing the GSED experiment the amplitude of the driving sinusoid applied as part of the excitation signal should be the smallest value that allows detection of a resonance peak. Larger amplitudes lead to crashing of vertically resonant microbridges into the substrate, and resonant peak shifts (toward larger frequency values) of up to 20 kHz have resulted from this.

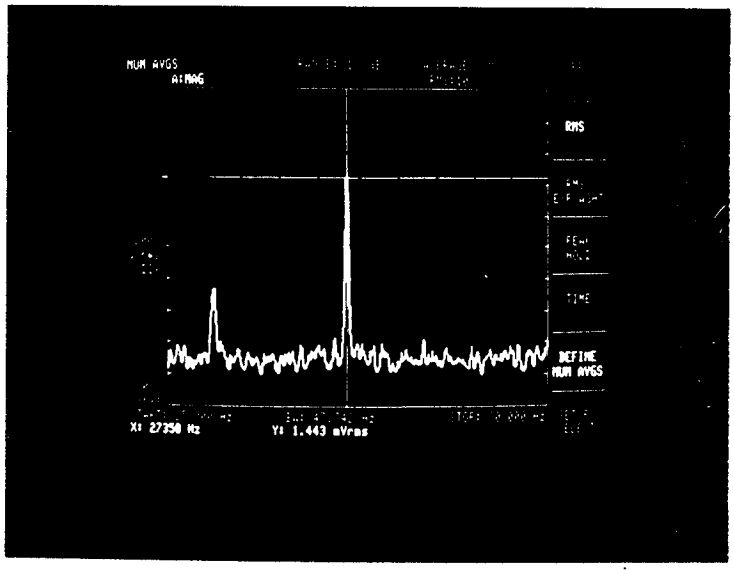

Figure 4.4. Photograph of the GSED Fourier spectrum as seen on the display of an HP 3561A Spectrum Analyzer, which operates in real-time (no swept filter).

4.4 Approximate Determination of Quality Factor, Q

4.4.1 Using a Swept-filter Spectrum Analyzer

The dependence on display position of the resonance peak amplitude of an analog spectrum analyzer conveniently allows for an approximate method for Q-determination. The Q determined, here, is that defined by the number of oscillation cycles sustained before complete damping.

The procedure consists of first establishing a resonance peak, then adjusting the starting frequency of the spectrum analyzer display (toward lower values—even negative values) until the peak disappears. The time required for damping out of the signal may be calculated via the equation

$$t_d = \frac{(f_r - f_{srt})}{(f_{stp} - f_{srt})} T_s \tag{4.3}$$

where f_r is the resonant frequency, f_{srt} and f_{stp} are the starting and stopping display frequencies, respectively, and T_s is the SWEEP TIME. The Q may then be calculated using the

equation

$$Q = \frac{t_d}{f_r} \tag{4.4}$$

This technique, although not useful for low Q conditions, allows for easy, approximate determination of extremely high Q's (as well as mid-range Q's). In Fig. 4.5 is presented a series of photographs of a spectrum analyzer display during Q-determination for this same microbridge. In each of the photos, the tall, broad peak is the zero frequency peak, while the peak to the left of it (closest to the left side of the display) is the negative frequency resonant peak. The positive frequency resonant peak is seen to gradually disappear as the starting frequency of the spectrum analyzer range is moved toward lower values, increasing the time necessary for the swept filter to reach the positive resonant frequency. Data for Q-determination as described in this paper is taken from the last display setting. The Q for the bridge in question is found to be around 10000.

4.4.2 Using a Real-time Spectrum Analyzer

When a real-time spectrum analyzer is used, quality factor can be determined much more accurately. The procedure for this is as follows:

1. Determine the amplitude $|V_{GSED1}|$ of the resonance peak as in Fig. 4.1.

2. Adjust the phase of the trigger signal with respect to the gated-sinusoid such that the trigger lags it by a specified time interval t_{lag} (see Fig. 4.6). Measure the amplitude of the resonance peak $|V_{GSED2}|$.

Having measured the amplitudes at two time points, the logarithmic decrement δ may then be found using [20]:

$$\delta = \frac{1}{n} \ln \left(\frac{|V_{GSED1}|}{|V_{GSED2}|} \right) \tag{4.5}$$

where $n = f_r t_{lag}$ is the number of cycles between the time points. With this, the viscous damping ratio can now be determined using

$$\zeta = \frac{\delta}{\sqrt{(2\pi)^2 + \delta^2}}. \tag{4.6}$$

Finally, the quality factor Q may be determined for small values of ζ using

$$Q = \frac{1}{2\zeta}. \tag{4.7}$$

(a)

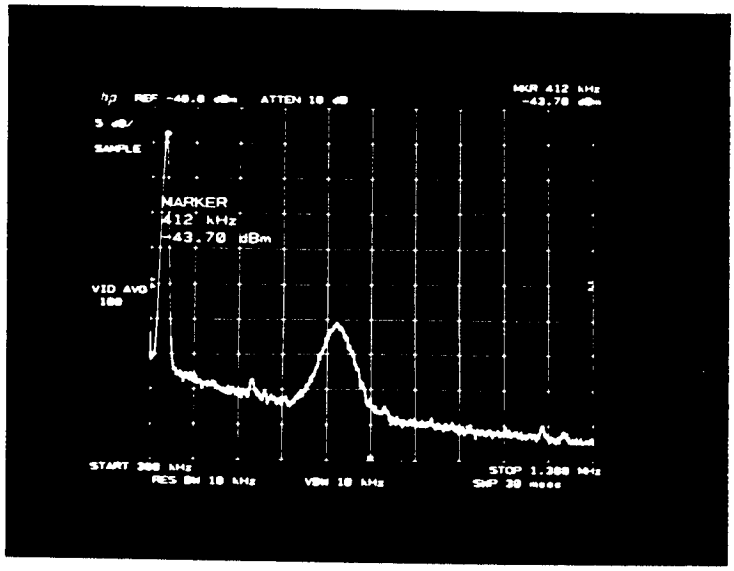

(b)

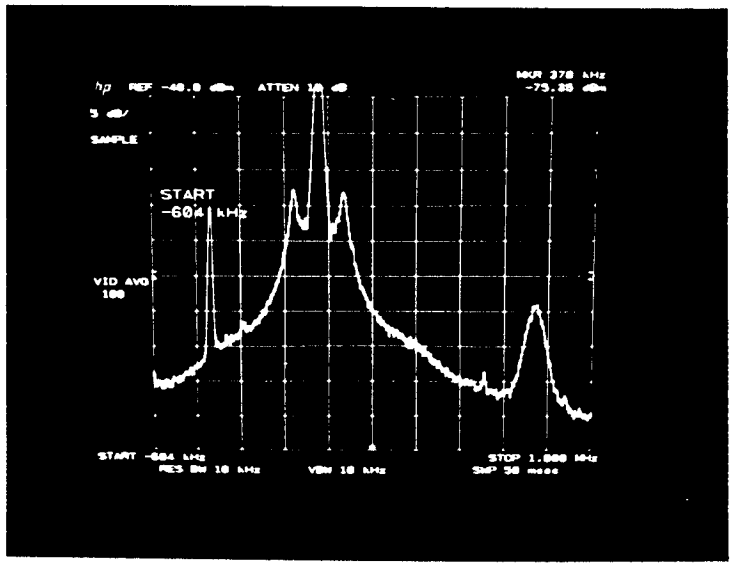

Figure 4.5. Q-determination using GSED with a swept-filter analog spectrum analyzer. (a) First, the magnitude of the resonance peak is measured at a minimum interval between drive signal cut-off and spectrum analyzer triggering. (b) Then, the position of peak on the spectrum analyzer display is moved to the right (i.e. the interval between cut-off of the drive signal and triggering of the spectrum analyzer is increased) until the peak disappears. The position of the peak can then be used to calculate an approximate value of Q, as discussed in the text.

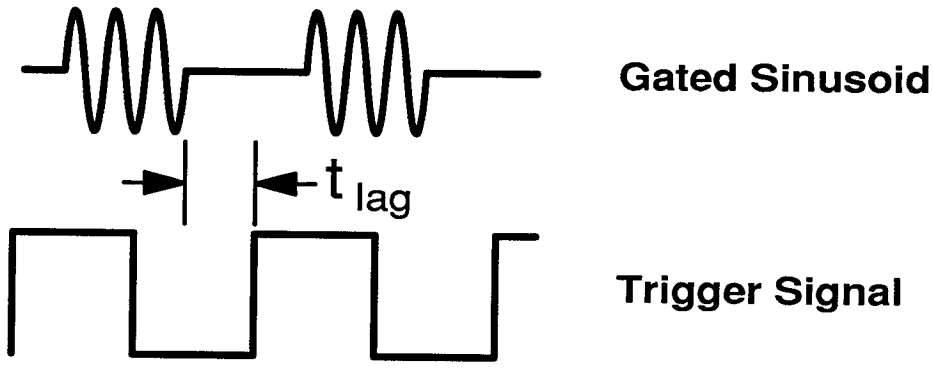

Figure 4.6. Phase adjustment of the trigger signal with respect to the gated-sinusoid to give a delay in the response of a real time spectrum analyzer. This is necessary for Q-determination.

4.5 The Deficiencies of GSED

Gated-sinusoid excitation and detection provides a convenient technique for measurement of microresonator resonance frequency and quality factor. However, since it obtains information through the damped oscillation of a microresonator, it cannot provide a direct measurement of the transconductance spectrum. Application of GSED toward extraction of $\frac{\partial C}{\partial x}$ would be an inaccurate ordeal, and the technique cannot be used conveniently for microresonator system performance verification (which requires a transconductance spectrum).

Fortunately, there is another more powerful characterization technique to be detailed in the next chapter.

5.0 ELECTROMECHANICAL AMPLITUDE MODULATION

The GSED technique, discussed in the previous chapter, enables motional current detection by separating it from feedthrough current in the *time domain*. However, for characterization of microresonators, its limitations are severe, since it cannot conveniently provide a transconductance spectrum.

Fortunately, other options exist. Rather than separate motional current from parasitics in the *time domain*, the currents may be separated in the *frequency domain*, allowing more direct methods for transconductance spectrum determination. The key to an extremely powerful *frequency domain* technique involves the concept of electromechanical amplitude modulation (EAM). The key to EAM lies in the biasing of the microstructure, which includes an ac carrier signal, as well as the dc-bias required for drive force amplification. Qualitatively, the carrier signal and its time-derivative are multiplied by capacitive elements of microstructure motion, resulting in motional current frequency-shifted to sidebands around the carrier frequency and separated from dc parasites still at the drive frequency.

The EAM technique is useful for one-port, as well as multi-port, microstructures with virtually any range of Q. It has been successfully demonstrated as a convenient, repeatable, wafer-level measurement technique and shows potential for application in integrated detection circuitry.

This chapter will detail the theory of EAM and discuss experimental set-ups applied to two-ports and one-ports. A remote EAM technique will also be detailed. As a prelude, however, another frequency domain detection technique related to EAM will be discussed: detection by frequency-doubling.

5.1 Detection By Frequency-doubling

5.1.1 Frequency-doubling

In Eq. (2.9), the drive current into an electrostatic-comb driven microresonator was found to include a modulation component at twice the excitation frequency. This component results from multiplicative interaction between the microresonator ac capacitance $C(t)$ and the excitation voltage v_d. To see this, let us reconsider the general form for $i_d(t)$, focusing on the terms responsible for the modulation component:

$$i_d(t) = C_o\frac{dv_d}{dt} \underbrace{+x\frac{\partial C}{\partial x}\frac{dv_d}{dt} + v_d\frac{\partial C}{\partial x}\frac{\partial x}{\partial t}}_{\text{modulation components}} + V_{PD}\frac{\partial C}{\partial x}\frac{\partial x}{\partial t}, \tag{5.1}$$

Defining at resonance

$$v_d(t) = |v_d|\cos\omega_r t \tag{5.2}$$

$$x(t) = |x|\sin\omega_r t \tag{5.3}$$

the modulation component at resonance may now be found:

$$i_{modulation}(t) = x\frac{\partial C}{\partial x}\frac{dv_d}{dt} + v_d\frac{\partial C}{\partial x}\frac{\partial x}{\partial t} \tag{5.4}$$

$$= \omega_r|x||v_d|\frac{\partial C}{\partial x}\cos 2\omega_r t = i_{2\omega} \tag{5.5}$$

From Chapter 2, we may find an expression for $|x|$:

$$|x| = X(j\omega_r) = M(j\omega_r)V_{PD}\frac{\partial C}{\partial x}V_d = V_{PD}\frac{Q}{k_{sys}}\frac{\partial C}{\partial x}V_d \tag{5.6}$$

Inserting (5.6) in Eq. (5.5), we find

$$i_{2\omega} = \omega_r V_{PD}\frac{Q}{k_{sys}}\frac{\partial C}{\partial x}|v_d|^2\cos 2\omega_r t. \tag{5.7}$$

Note that there is no dc component arising from the above modulation.

The modulation component at twice the resonance frequency is separate from the motional current and accompanying parasitic components at the resonance frequency. Thus, it has potential as a technique for determining the transconductance spectrum of a microresonator. An experimental set-up implementing this detection scheme using a spectrum analyzer is shown in Fig. 5.1(a). Figure 5.1(b) presents the expected Fourier spectrum of the sense current i_s.

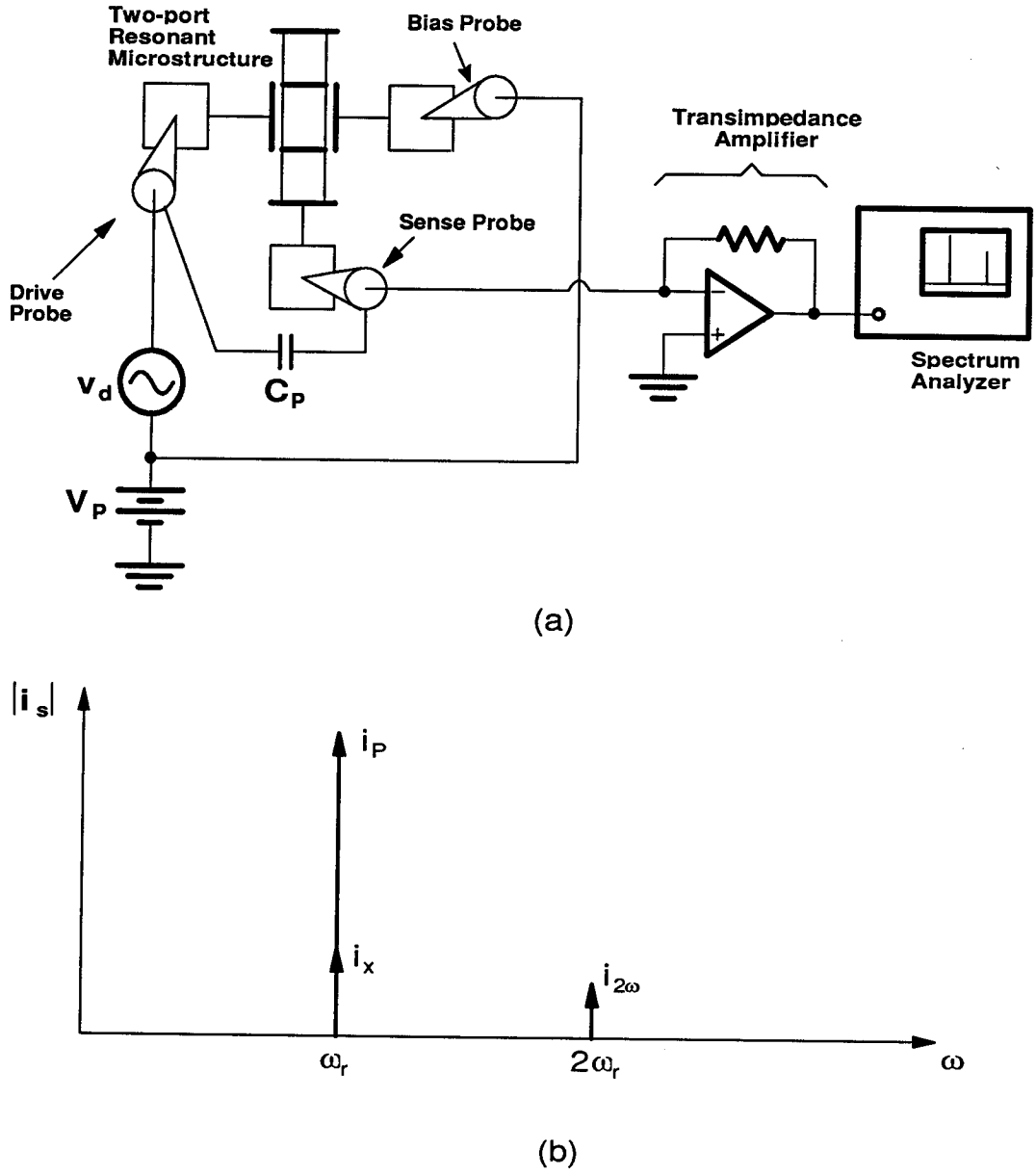

Figure 5.1. (a) Experimental set-up for detecting resonance using the frequency-doubled component of the microresonator sense current. (b) Fourier spectrum of the sense current i_s of (a). The frequency-doubled component is separate from the feedthrough parasitic at the drive frequency, and thus, is detectable.

5.1.2 Problems With Detection Via Frequency-doubling

In theory, resonance frequency detection using the frequency-doubling technique above seems sound. However, several second order effects in the real world severely limit the usefullness this approach.

First, the technique can really only work with an ideal function generator which produces a clean sinusoidal waveform containing no distortion harmonics. In air, where a large excitation voltage ($|v_d| = 10$ V) is required, even an attenuated (by 60 dB, relative to the fundamental) second harmonic of the excitation voltage can feedthrough the probe-to-probe parasitic capacitance and blanket the tiny frequency-doubling current. The second harmonic for most function generators is large enough to prohibit the detection of resonance for a microresonator in air. For microresonators operated in vacuum, the technique is successful, since the required drive voltages are on the order of only 10 mV, resulting in second harmonics three orders of magnitude smaller than in the case of operation at atmospheric pressure.

However, even if the inconvenience of operation in vacuum is acceptable, determination of the microresonator transconductance spectrum is tedious, since a network analyzer, which can provide a transconductance spectrum only for a frequency component at the drive frequency, cannot be used. Demodulation techniques to mix the frequency-doubled component back to the drive frequency (thus, allowing use of a network analyzer) prove futile, prohibited by nonidealities in demodulation circuitry. Specifically, to demodulate the $i_{2\omega}$ component a demodulation carrier signal at the drive frequency should be used. If, however, the multiplier circuit performing the demodulation function cannot completely suppress the demodulation carrier, this carrier will blanket the $i_{2\omega}$ component when it gets mixed back to the drive frequency. Several multiplier circuits were investigated, and none of them offered enough carrier suppression.

Thus, the frequency-doubling technique for resonance detection provides only a slight advantage over GSED in that it can obtain a transconductance spectrum through tedious plotting of spectrum analyzer points at various frequencies. Like GSED, it is effective only in vacuum. The main difference from GSED is that rather than separating the motional current from the parasites in the time domain, it does so in the frequency domain.

Although the frequency-doubling technique suffers from the above constraints, it is still possibly the best technique available for microresonators with very high resonance

frequencies, since it requires very little post processing electronics. Indeed, the merit of frequency-doubling goes even further, since a simple extension of its modulation concept leads to the electromechanical amplitude modulation (EAM) detection technique, the principle result of this report.

5.2 Electromechanical Amplitude Modulation

In order to allow the use of a network analyzer for transconductance spectrum determination, the frequency of the demodulating signal must be different from the drive frequency. Thus, rather than have the drive signal v_d as the frequency-shifting carrier, as is the case in frequency-doubling, a carrier signal v_c with frequency $\omega_c \neq \omega_d$ must be injected into the system in such a way that it multiplies with the motional current, i.e. it is modulated by the motional current. Upon subsequent demodulation, the motional current at ω_d will be separate from any demodulation components at ω_c left over due to nonideal suppression by the multiplier circuit. The resulting output signal will be appropriate for input to a network analyzer.

Injection of the carrier signal v_c can be achieved as shown in Fig. 5.2, which presents a schematic of the excitation and biasing necessary for realization of electromechanical amplitude modulation (EAM) for a two-port electrostatic-comb driven microresonator. The principle difference from the drive configurations shown previously lies in the biasing of the microstructure, which now includes an ac carrier signal, as well as the dc-bias. The latter is still necessary, since it both amplifies the drive force (Eq. (2.14)) and allows this force to be at the same frequency as the drive voltage.

Qualitatively, the carrier signal and its time-derivative are multiplied by capacitive elements of microstructure motion, resulting in motional current, frequency-shifted to sidebands around the carrier frequency and separated from dc parasites still at the driving frequency. The end result of the EAM technique, after demodulation, is an effective nulling of all dc feedthrough capacitors, including any dc capacitors intrinsic to the microresonator.

The principle mechanisms involved in electromechanical amplitude modulation will now be derived.

5.2.1 The EAM Sidebands

The Fourier spectrum for the sense current i_s in Fig. 5.2 will now be derived for the case of a two-port electrostatic-comb driven lateral microresonator. This current is given by (refer to Fig. 5.2)

$$i_s = C_{PD}\frac{dV_f(t)}{dt} + C_{PC}\frac{dV_s(t)}{dt} + C(t)\frac{dV_s(t)}{dt} + V_s(t)\frac{dC(t)}{dt} \tag{5.8}$$

where

$$v_d(t) = |v_d|\cos\omega_d t \tag{5.9}$$

$$v_c(t) = |v_c|\cos\omega_c t \tag{5.10}$$

$$V_f(t) = v_d(t) \tag{5.11}$$

$$V_s(t) = V_{PC} + v_c(t) \tag{5.12}$$

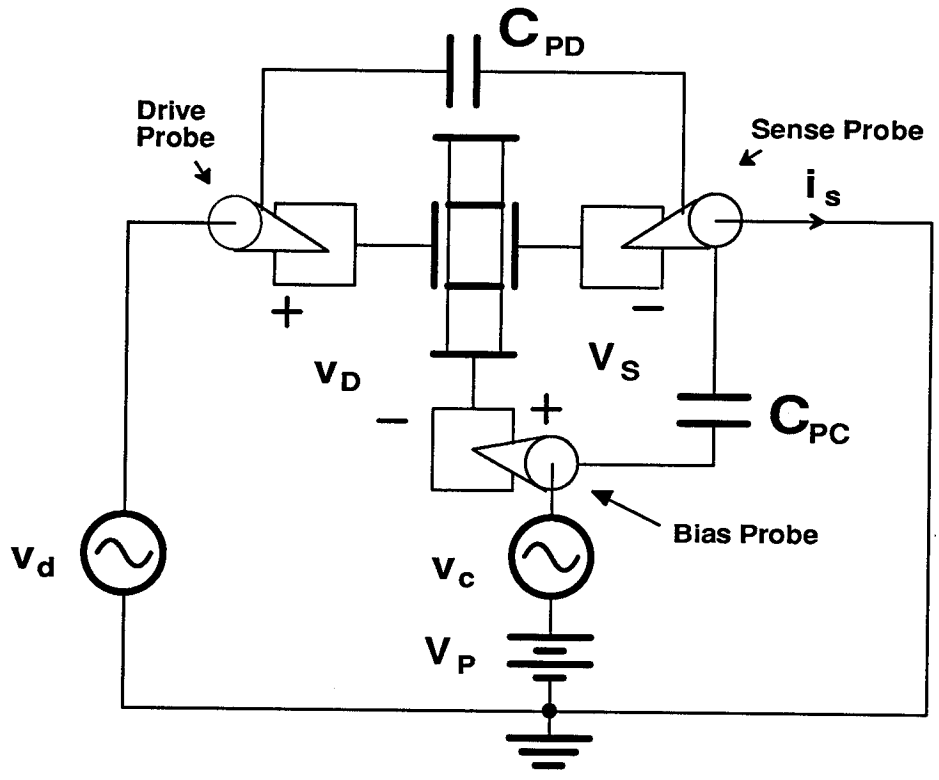

Figure 5.2. Biasing and excitation circuitry necessary for realization of electromechanical amplitude modulation (EAM).

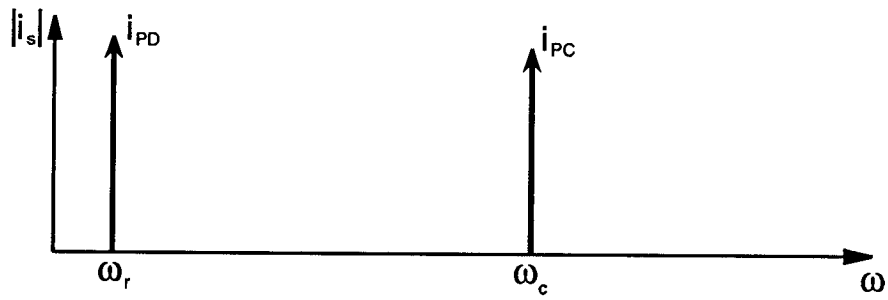

Figure 5.3. Fourier spectrum of the sense current i_s of Fig. 5.2 for off resonance drive frequencies.

$$C(t) = \begin{cases} \approx C_o & \text{off resonance} \\ C_o + C_m(t) & \text{at resonance} \end{cases} \tag{5.13}$$

$$C_m(t) = |C_m| \sin \omega_r t \tag{5.14}$$

where $C(t)$ represents the microresonator finger-overlap capacitance at the *sense port*, C_o is the dc value of this capacitance, $C_m(t)$ is the motional (ac value of) capacitance at the sense port, and C_{PD} and C_{PC} are parasitic capacitors (comprised mainly of probe-to-probe capacitance).

Solving Eq. (5.8) using the off resonance condition of Eq. (5.13) the current entering the sense port during nonresonance periods is found to be

$$i_P = -(\omega_d C_{PD}|v_d|\sin\omega_d t + \omega_c(C_{PC} + C_o)|v_c|\sin\omega_c t). \tag{5.15}$$

This current is composed predominantly of parasitic components, and thus, it is given the subscript P. The Fourier spectrum for i_s off resonance, predicted by Eq. (5.15), is shown in Fig. 5.3.

At resonance, Eq. (5.8) with the appropriate condition of Eq. (5.14) and setting $\omega_d = \omega_r$ (r for resonance), yields

$$\begin{aligned} i_r = {} & i_P + \omega_r V_P |C_m|\cos\omega_r t \\ & - \frac{1}{2}(\omega_c - \omega_r)|C_m||v_c|\cos(\omega_c - \omega_r)t \\ & + \frac{1}{2}(\omega_c + \omega_r)|C_m||v_c|\cos(\omega_c + \omega_r)t. \end{aligned} \tag{5.16}$$

The current peaks (in the Fourier spectrum) due to motion of the microstructure are those containing the time-varying capacitance amplitude term, $|C_m|$. The motional currents of

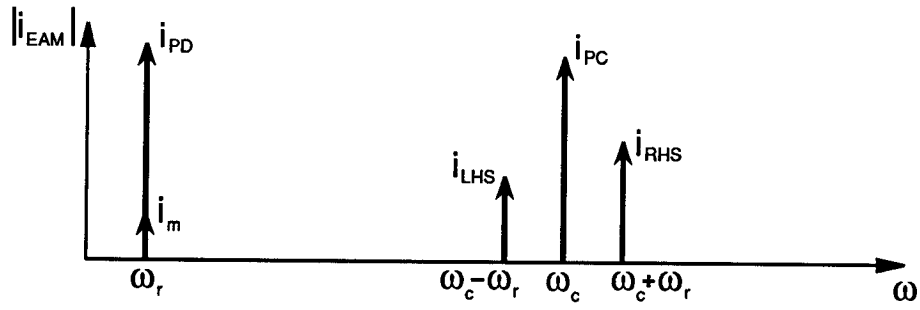

Figure 5.4. Fourier spectrum for $i_s = i_{EAM}$ of Fig. 5.2 at resonance.

interest, however, are only those at frequencies $(\omega_c - \omega_r)$ and $(\omega_c + \omega_r)$, since the motional current at ω_r is inaccessible due to masking by feedthrough currents. The amplitudes of these sidebands are readily seen from Eq. (5.16) to be given by

$$|I_{LHS}| = \frac{1}{2}(\omega_c - \omega_r)|C_m||v_c| \tag{5.17}$$

$$|I_{RHS}| = \frac{1}{2}(\omega_c + \omega_r)|C_m||v_c|. \tag{5.18}$$

These equations show that the left-hand and right-hand sidebands of motional current are not equal in amplitude. The Fourier spectrum corresponding to Eq. (5.16) for i_s at resonance is presented in Fig. 5.4.

Equations (5.17) and (5.18) may be converted to useful transconductance equations, relating phasor sense current I_s to phasor drive voltage V_d, given an expression for $|C_m|$. Thus, defining the displacement x of the microstructure at resonance by

$$x = |X|\sin\omega_r t, \tag{5.19}$$

we can obtain an expression for $|C_m|$ through the time-derivative of C_m (Eq. (5.14))

$$\frac{\partial C_m(x,t)}{\partial t} = \frac{\partial C(x,t)}{\partial x}\frac{\partial x}{\partial t}. \tag{5.20}$$

Converting to phasor form and cancelling $j\omega$ terms gives

$$|C_m| = \left(\frac{\partial C}{\partial x}\right)_s |X|. \tag{5.21}$$

The expression for the transfer function relating phasor displacement X to phasor drive voltage V_d for an electrostatic-comb driven lateral resonant structure at resonance can be found by evaluating Eq. (2.20) at $\omega = \omega_r$, yielding

$$\left|\frac{X}{V_d}\right| = V_P \frac{Q}{k_{sys}}(\partial C/\partial x)_d. \tag{5.22}$$

Inserting (5.22) in (5.21), the expression for $|C_m|$ is found to be

$$|C_m| = V_P \frac{Q}{k_{sys}} \left(\frac{\partial C}{\partial x}\right)_d \left(\frac{\partial C}{\partial x}\right)_s V_d. \tag{5.23}$$

Substitution of (5.23) in Eqs. (5.17) and (5.18) yields the transconductance functions at resonance relating phasor sense current I_s and phasor drive voltage V_d for each sideband of motional current:

$$\left|\frac{I_{LHS}}{V_d}\right| = \frac{1}{2}(\omega_c - \omega_r)|v_c|V_P \frac{Q}{k_{sys}} \left(\frac{\partial C}{\partial x}\right)_d \left(\frac{\partial C}{\partial x}\right)_s \tag{5.24}$$

$$\left|\frac{I_{RHS}}{V_d}\right| = \frac{1}{2}(\omega_c + \omega_r)|v_c|V_P \frac{Q}{k_{sys}} \left(\frac{\partial C}{\partial x}\right)_d \left(\frac{\partial C}{\partial x}\right)_s. \tag{5.25}$$

The magnitude of the transconductance at resonance of a dc-biased (*no ac*) electrostatic-comb driven lateral microresonator is given by (using Eq. (2.26))

$$\frac{I_s}{V_d} = \omega_r V_P^2 \frac{Q}{k_{sys}} \left(\frac{\partial C}{\partial x}\right)_d \left(\frac{\partial C}{\partial x}\right)_s \tag{5.26}$$

Comparison of (5.26) with Eqs. (5.24) - (5.25) shows that motional current produced via EAM contains a $\frac{1}{2}(\omega_c \pm \omega_r)$ factor replacing the ω_r term of oscillating dc-biased structures. Thus, motional current produced via EAM is amplified over that produced by an oscillating dc-biased (*only*) structure by a factor of approximately $\frac{\omega_c}{2\omega_r}\frac{|v_c|}{V_P}$ (for $\omega_c \gg \omega_r$, which is usually the case). Since the carrier frequency may be selected arbitrarily large (the limitation coming from the bandwidth of post-processing electronics), this amplification may be very large, indeed.

5.2.2 Demodulation of EAM Motional Current

In order to view the transconductance spectrum of the microresonator under a network analyzer, the EAM motional current i_{EAM} must be post-processed by *off-chip* electronics. Figure 5.5 summarizes the required signal processing.

The first step (Fig. 5.5) involves a transimpedance amplification and bandpass filtering to eliminate the parasitic feedthrough component at the drive frequency ω_r (assuming resonance). Such filtering also enhances the signal-to-noise ratio of the sensing electronics.

Next (Fig. 5.5), the EAM components of current i_{RHS} and i_{LHS} must be demodulated back down to the resonance frequency ω_r, yielding finally, the Fourier spectrum shown in

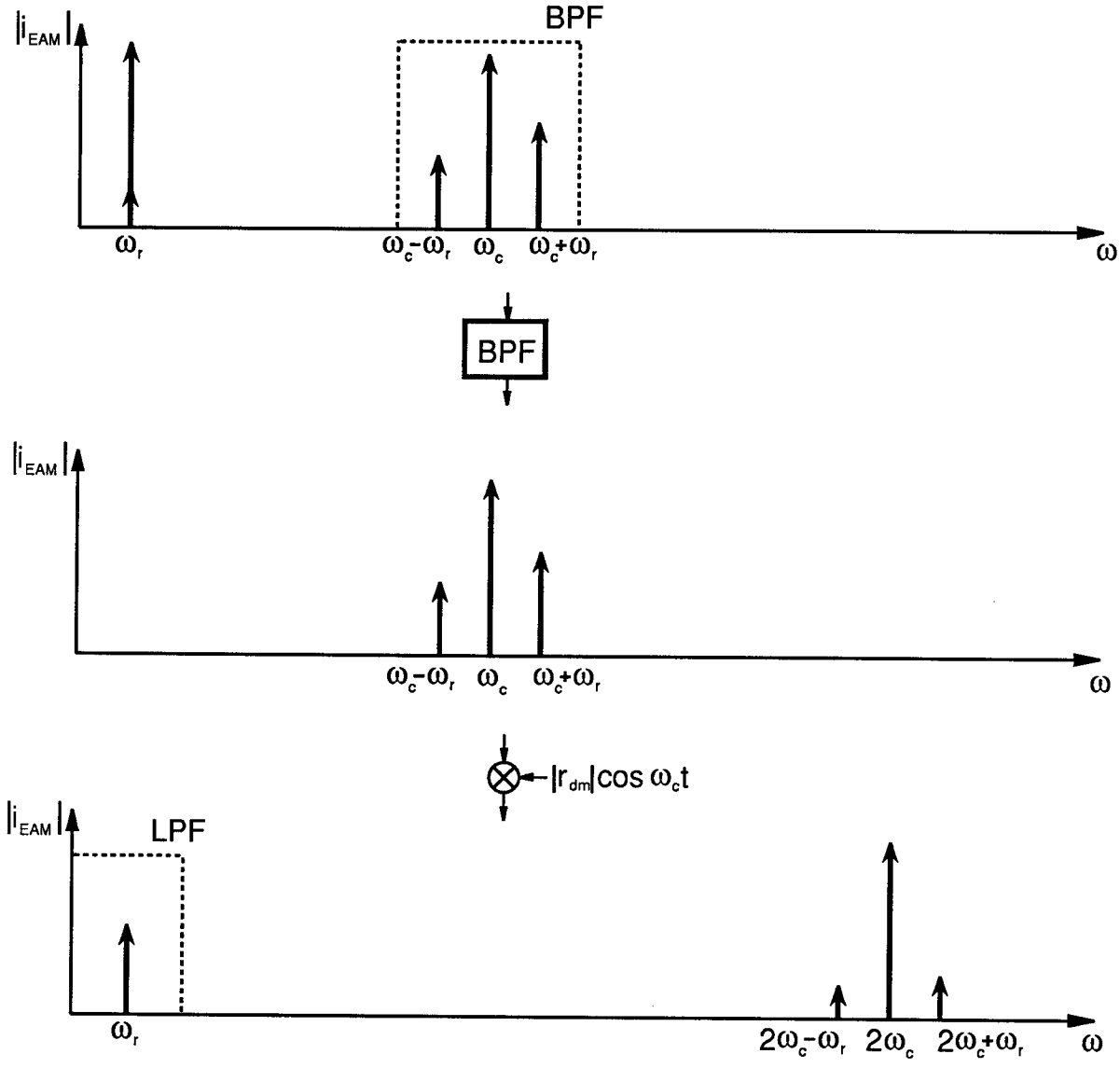

Figure 5.5. Schematic flow diagram of the post-processing necessary to prepare the EAM current i_{EAM} for input to a network analyzer. (a) A bandpass filter is used to filter out the components at the drive frequency. This filtering also improves the signal-to-noise ratio of the system. (b) The sidebands are demodulated back down to the drive frequency with a sinusoid at the carrier frequency ω_c and with adjustable phase. (c) Final EAM output suitable for input to a network analyzer. For viewing with an oscilloscope, the lowpass filter will be necessary.

Fig. 5.5(c). The spectrum in (c) is suitable for input to a network analyzer even without the lowpass filtering shown. The lowpass filter, however, is necessary for viewing via an oscilloscope.

Let us now focus on the demodulation of the EAM motional current back to the original microstructure oscillation frequency. As with any amplitude-modulated signal, this can be achieved by multiplication with a sinusoid of the carrier frequency ω_c.

To obtain an expression for signal at the output of the demodulator v_{dm}, let us first assume a demodulating sinusoid with amplitude $|r_{dm}|$[1] and *in phase* with the original carrier:

$$r_{dm} = |r_{dm}| \cos \omega_c t \tag{5.27}$$

Multiplication of Eq. (5.16) with (5.27), then, yields the following:

$$\begin{aligned} v_{dm} &= i_r r_{dm} \\ &= -\frac{1}{2}\omega_d C_{PD}|v_d||r_{dm}|[\sin(\omega_r - \omega_c)t + \sin(\omega_r + \omega_c)]t \\ &\quad -\frac{1}{2}\omega_c C_{PC}|v_c||r_{dm}|\sin 2\omega_c t \\ &\quad +\frac{1}{2}\omega_r V_P|C_m||r_{dm}|[\cos(\omega_c - \omega_r)t + \cos(\omega_c + \omega_r)t] \\ &\quad -\frac{1}{4}(\omega_c - \omega_r)|C_m||v_c||r_{dm}|[\cos(2\omega_c - \omega_r)t + \cos\omega_r t] \\ &\quad +\frac{1}{4}(\omega_c + \omega_r)|C_m||v_c||r_{dm}|[\cos(2\omega_c + \omega_r)t + \cos\omega_r t]. \end{aligned} \tag{5.28}$$

Only the term at the resonance frequency ω_r is of interest for a transconductance spectrum. From Eq. (5.28),

$$v_{EAM} = \frac{1}{2}\omega_r|C_m||v_c||v_{dm}|\cos\omega_r t. \tag{5.29}$$

The current sensed after demodulation is, thus, of the same order of magnitude as the current that would be sensed from a dc-biased (*no ac*) oscillating microstructure (Eq. (5.26)). Demodulation by a sinusoid *in phase* with the original carrier negates the $\omega_c/2\omega_r$ amplification originally provided by EAM.

Fortunately, however, the EAM amplification can be retrieved by proper selection of the phase of the demodulating carrier r_{dm}. To see this, let us now obtain an expression for

[1] A resistance is used since post-processing of i_{EAM} should effectively implement a transimpedance funtion (to allow voltage input to a network analyzer).

the amplitude of v_{EAM} as a function of the phase θ of r_{dm}, generalized as

$$r_{dm} = |r_{dm}| \cos(\omega_c t + \theta). \tag{5.30}$$

Multiplication of Eq. (5.30) with (5.16) and taking only motional current terms yields:

$$\begin{aligned} v_{dm} &= i_r r_{dm} \\ &= \ldots. - \frac{1}{4}(\omega_c - \omega_r)|C_m||v_c||r_{dm}|\{\cos[(2\omega_c - \omega_r)t + \theta] + \cos(\omega_r t + \theta)\} \\ &\quad + \frac{1}{4}(\omega_c + \omega_r)|C_m||v_c||r_{dm}|\{\cos[(2\omega_c + \omega_r)t + \theta] + \cos(\omega_r t + \theta)\}. \end{aligned} \tag{5.31}$$

Taking terms at ω_r,

$$v_{EAM} = \frac{1}{4}|C_m||v_c||r_{dm}|\{-(\omega_c - \omega_r)\cos(\omega_r t + \theta) + (\omega_c + \omega_r)\cos(\omega_r t - \theta)\} \tag{5.32}$$

Converting to phasor form, we have

$$V_{EAM} = \frac{1}{2}|C_m||v_c||r_{dm}|\{\omega_r \cos\theta - j\omega_c \sin\theta\}. \tag{5.33}$$

Expressing the above in terms of magnitude and phase,

$$V_{EAM} = |V_{EAM}|e^{\angle V_{EAM}} \tag{5.34}$$

where

$$|V_{EAM}| = \frac{1}{2}|C_m||v_c||r_{dm}|\sqrt{\omega_r^2 \cos^2\theta + \omega_c^2 \sin^2\theta} \tag{5.35}$$

$$\angle V_{EAM} = \tan^{-1}\left(-\frac{\omega_c \sin\theta}{\omega_r \cos\theta}\right). \tag{5.36}$$

The θ corresponding to the maximum V_{EAM} amplitude can be found by setting the derivative of $|V_{EAM}|$ to zero and solving for θ, yielding:

$$\frac{\partial|V_{EAM}|}{\partial\theta} = \frac{2(\omega_c^2 - \omega_r^2)\sin\theta\cos\theta}{\sqrt{\omega_r^2 \cos^2\theta + \omega_c^2 \sin^2\theta}} = (\omega_c^2 - \omega_r^2)\sin\theta\cos\theta = 0. \tag{5.37}$$

From Eq. (5.37), $|V_{EAM}|$ is maximized when $\theta = 0°$ or $90°$, depending upon which of ω_c and ω_r is larger.

For the usual case where $\omega_c \gg \omega_r$, $|V_{EAM}|$ is maximized for $\theta = 90°$, as can be seen in the $|V_{EAM}|$ vs. θ plot shown in Fig. 5.6. Evaluating Eq. (5.35) at $\theta = 90°$, the maximum

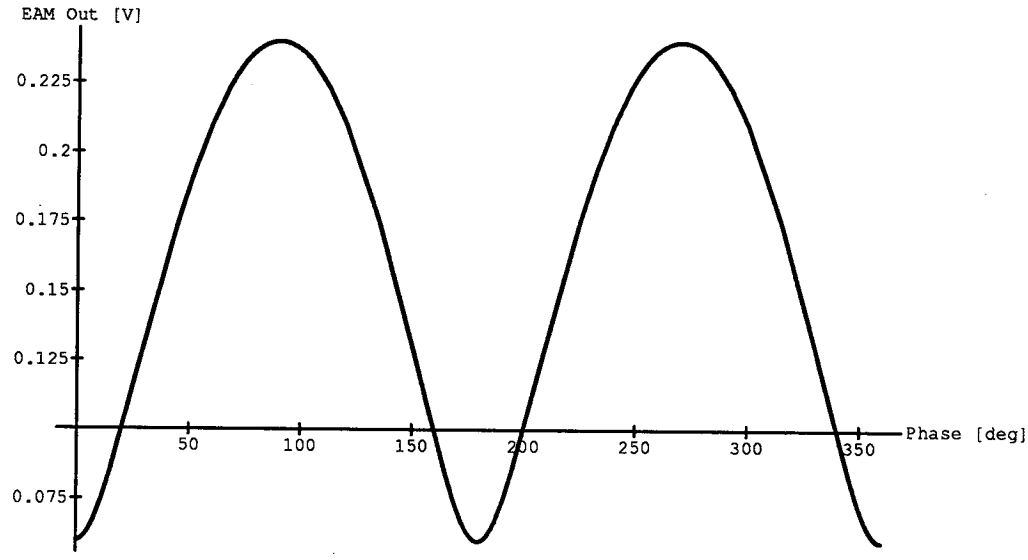

Figure 5.6. Amplitude of EAM output voltage $|V_{EAM}|$ vs. the phase of the demodulating signal, θ for the case of $\omega_c > \omega_r$. The plot is made specifically for the case of $|C_m| = 2.0 \times 10^{-10}$ F/m, $|v_c| = 3.0$ V, $|r_{dm}| = 10^4$, $\omega_c = 80$ kHz, and $\omega_r = 20$ kHz.

v_{EAM} is found to be

$$v_{EAM} = \frac{1}{2}\omega_c|C_m||v_c||r_{dm}| \sin \omega_r t. \tag{5.38}$$

Note that the maximum output signal is amplified over the output obtained directly from a dc-biased (only) microresonator by $\frac{\omega_c|v_c|}{2\omega_r V_P}$, assuming identical transimpedance amplification for both cases. In addition, unlike the output from a dc-biased (only) microresonator, the EAM demodulator output is 90° phase-shifted from the input signal v_d.

In summary, to maximize the output of the EAM demodulator, a demodulation signal 90° phase-shifted from the EAM carrier $r_{dm} = |r_{dm}| \sin \omega_c t$ is required. Such a demodulation signal yields an output with amplitude proportional to the carrier frequency and with phase 90° shifted from the drive signal.

5.2.3 Experimental Implementation of EAM

An experimental set-up implementing EAM for determination of the transconductance spectrum for a microresonator is presented in Fig. 5.7. The post-processing electronics

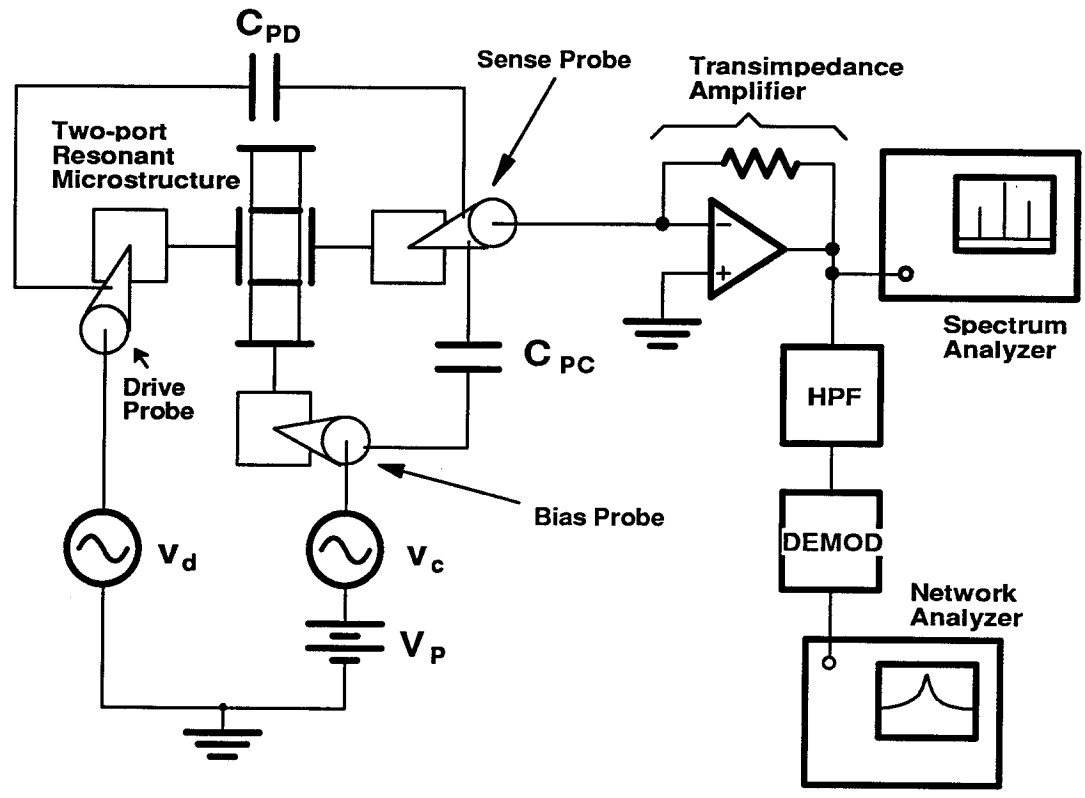

Figure 5.7. Schematic of the EAM system for determination of a microresonator transconductance spectrum.

shown follow closely that described in the previous section and in Fig. 5.5. More detailed information on the electronics used, including detailed circuit diagrams and equipment specifics, is given in Appendix A.

A sample spectrum obtained using the set-up of Fig. 5.7 is presented in Fig. 5.8 for a microresonator with properties summarized in the inset. The shape of the spectrum corresponds to pure series resonance, indicating an effective nulling of dc capacitance, both parasitic and intrinsic. Resonance frequency and quality factor are easily obtainable from the spectrum, and in the next chapter, the procedure for extracting the microresonator circuit model from such an EAM spectrum will be detailed.

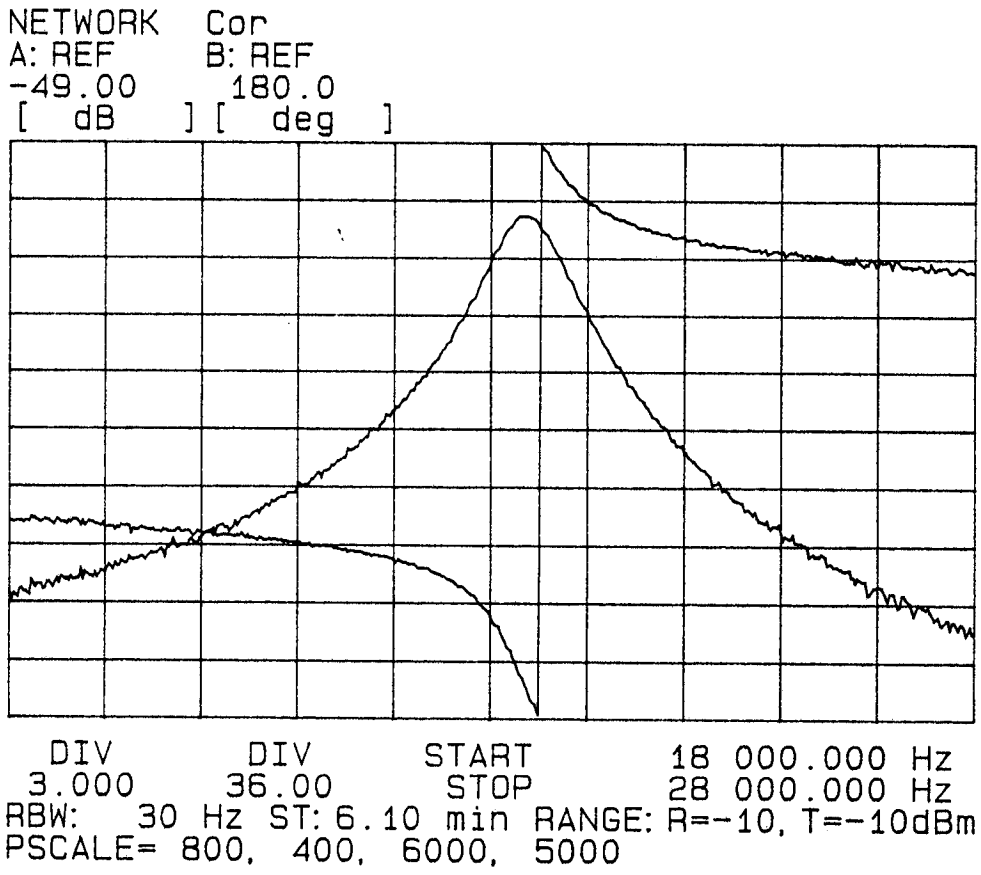

Figure 5.8. Transconductance spectrum for an electrostatic-comb driven lateral microresonator as determined by the EAM technique.

5.3 Remote Carrier EAM

The electromechanical amplitude modulation technique can detect and determine *any* ac capacitance, and thus, it can serve a very general role in characterization of micromechanical structures. One prime example of this is the availability of *remote carrier EAM*, in which the carrier signal is remotely, rather than directly, coupled to microresonator motion through a nearby noncontacting conductor. Remote carrier EAM can determine the shape of the transconductance spectrum of any microresonator without requiring application of a carrier to the resonant shuttle or any excitation electrode.

A typical experimental set-up for this technique is shown in Fig. 5.9. Here, the noncontacting conductor supplying the carrier is simply a tungsten probe. The movable shuttle of the microresonator (which is electrically connected to the microresonator ground plane) is grounded. In addition, a sense plate, halfway covered by the shuttle under off resonance

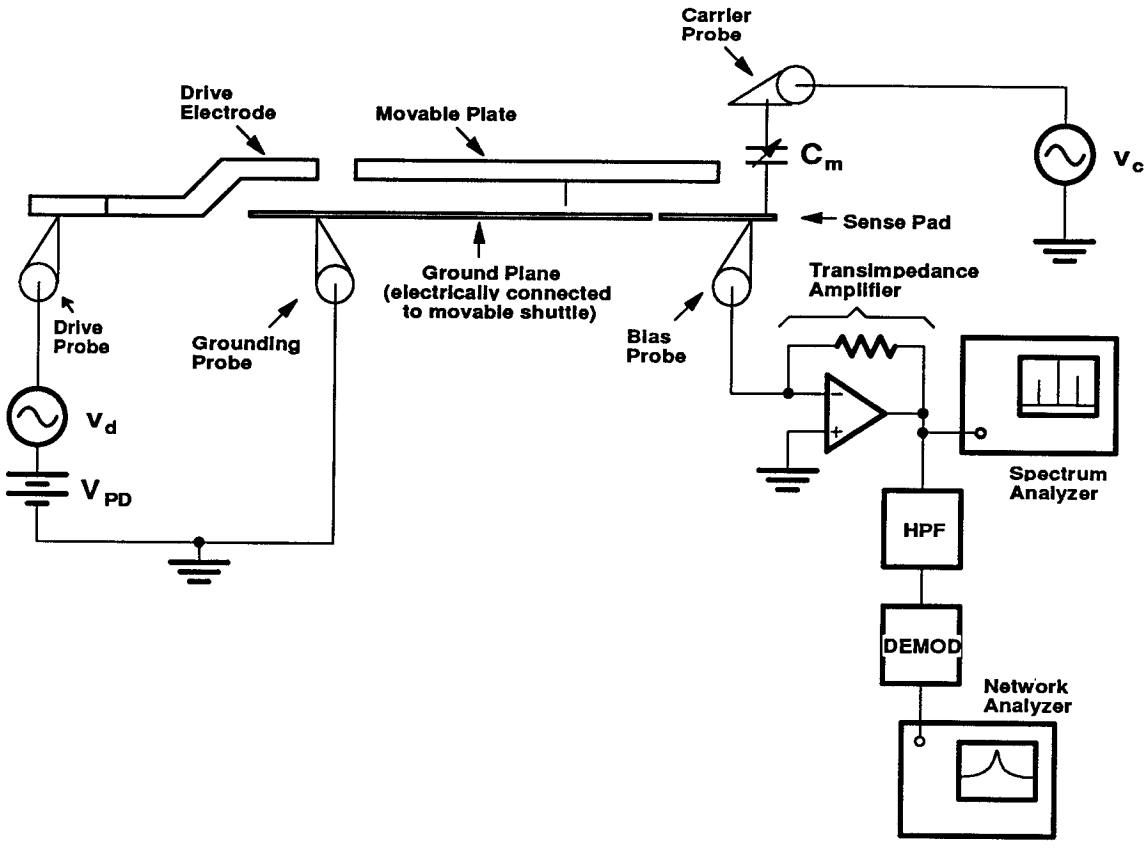

Figure 5.9. Schematic of an implementation of remote carrier EAM. Here, the noncontacting tungsten probe serves as one terminal of the time-varying capacitance to be measured and as the probe with which the carrier is introduced.

conditions, has been provided. This plate and the tungsten probe form the terminals of a capacitor which varies as the microresonator oscillates. This is the motional capacitance to be detected.

EAM is instigated in this system by applying the carrier v_c to the noncontacting probe (effectively, across the motional capacitance). Demodulation of the resulting EAM current can be achieved as before (with the same post-processing electronics).

The magnitude of capacitance variation might be of interest for certain applications, and this can be determined from the resulting transconductance spectrum by taking the EAM output voltage magnitude $|V_{EAM}|$ at resonance and using

$$|C_m| = \frac{2|V_{EAM}|}{\omega_c |v_c| |r_{dm}|}. \tag{5.39}$$

Of course, resonance frequency and quality factor are also easily extracted.

5.4 EAM for One-port Microresonators

EAM has been detailed extensively above for the case of a two-port microresonator, but with a slight modification in the biasing scheme, it also can be applied to one-ports. Figure 5.10 shows the experimental set-up necessary to implement EAM for one-ports for (a) a one-port parallel-plate driven microresonator and (b) a two-port electrostatic-comb driven microresonator used as a one-port.

The EAM current resulting at the summing node of the transimpedance amplifier can be found in the same manner as in Section 5.2.1. Thus, refering to Fig. 5.10,

$$\begin{aligned} i_r &= C_P\frac{dV_d(t)}{dt} + C(t)\frac{dV_d(t)}{dt} + V_d(t)\frac{\partial C(t)}{\partial t} \\ &= \underbrace{(C_P + C_o)\frac{dv_c}{dt}}_{\sin\omega_c t} + \underbrace{(C_P + C_o)\frac{dv_d}{dt}}_{\sin\omega_r t} + \underbrace{V_P\frac{\partial C}{\partial t}}_{\cos\omega_r t} + \underbrace{C_m(t)\frac{dv_c}{dt}}_{(\sin\omega_r t)(\sin\omega_c t)} + \underbrace{C_m(t)\frac{dv_d}{dt}}_{(\sin\omega_r t)^2} \\ &\quad \underbrace{v_c\frac{dv_c}{dt}}_{(\cos\omega_c t)(\cos\omega_r t)} + \underbrace{v_d\frac{dv_d}{dt}}_{(\cos\omega_r t)^2}, \end{aligned} \tag{5.40}$$

where the effective frequency contributions of each component are indicated. The Fourier spectrum of Eq. (5.40) is shown in Fig. 5.11. The terms of interest are, again, those at $(\omega_c \pm \omega_r)$, and these terms are found to be identical to those in Eq. (5.16). Thus, the sidebands of the EAM current for the system of Fig. 5.10 can be described as before. Demodulation of this current is also achieved in the same manner as for two-ports.

The only difference between the i_r of one-port EAM and that for two-port EAM is the presence of the frequency-doubled term. This term is masked by feedthrough of the drive signal second harmonic, anyway, so actually, there is practically no difference between the two. Incidentally, when selecting a carrier frequency for EAM, one should chose ω_c such that crossing by the frequency-doubled component and the $\omega_c - \omega_d$ term is avoided. Otherwise, a sharp glitch in the transconductance spectrum will appear.

5.5 Comparison of EAM to Capacitive Detection

The net effect of EAM detection compares very well with capacitive detection, shown in Fig. 5.12, where current is detected by the gate capacitance C_{gs1} of a depletion mode NMOS transistor. The gate of the transistor is biased to ground by a reverse biased diode

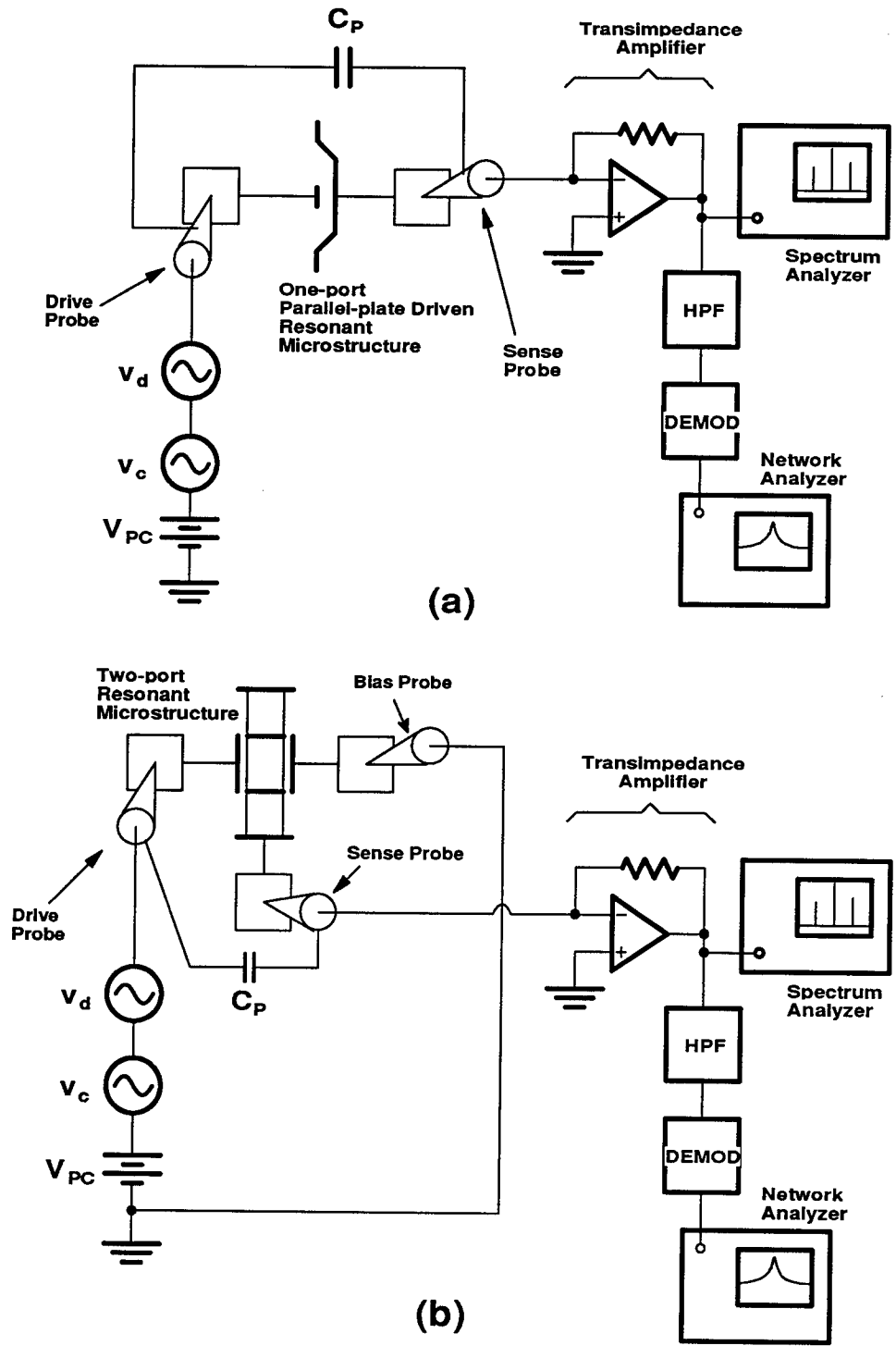

Figure 5.10. Experimental set-ups necessary to implement EAM for one-ports for (a) a one-port parallel-plate driven microresonator and (b) a two-port electrostatic-comb driven microresonator used as a one-port.

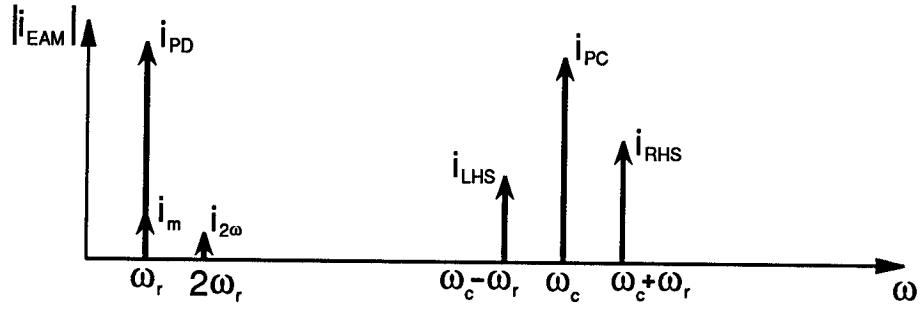

Figure 5.11. Fourier spectrum for the current seen at the summing node of the amplifier of Fig. 5.10 at resonance.

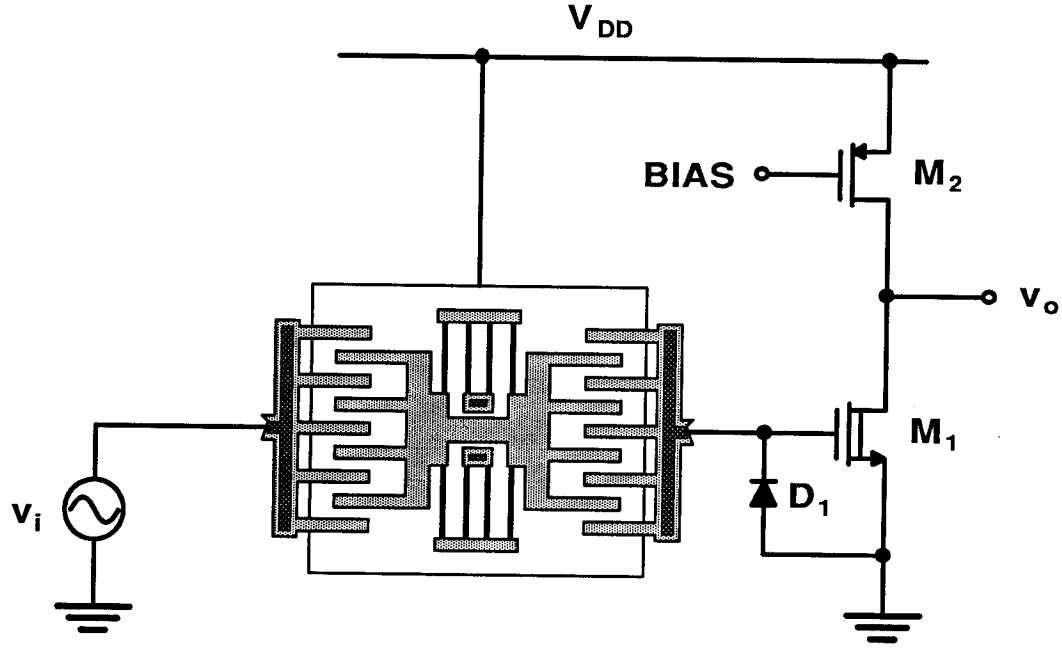

Figure 5.12. On-chip, the motional current of a microresonator can be detected via capacitive detection. Here, an implementation of capacitive detection is shown using a depletion mode NMOS transistor.

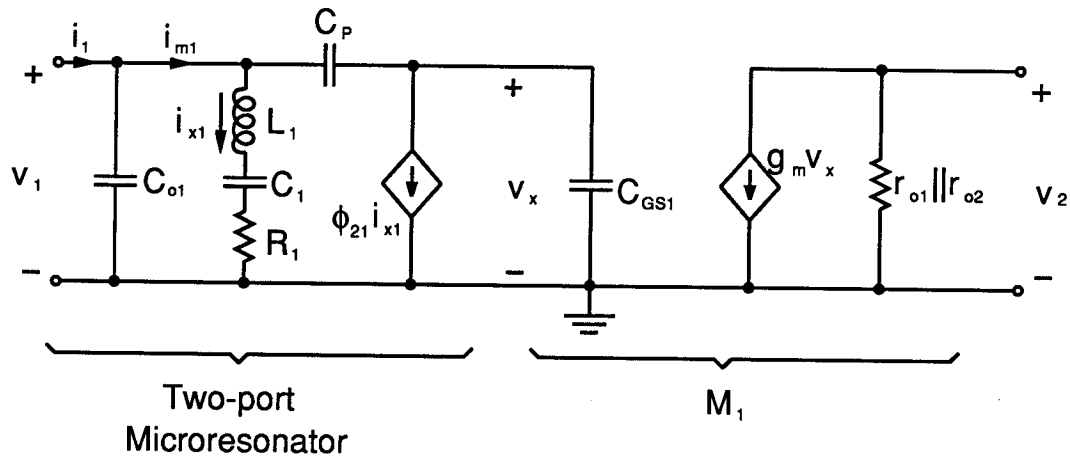

Figure 5.13. Small signal equivalent circuit for the on-chip detection scheme shown in Fig. 5.12 for (a) a two-port microresonator and (b) a one-port microresonator.

with high off resistance. The small signal equivalent circuit for Fig. 5.12 is shown in Fig. 5.13 (a) for a two-port microresonator and (b) for a one-port microresonator.

The current-to-voltage transfer function $\frac{V_o}{I_s}$ for the circuits of Fig. 5.13 is given by

$$\frac{V_o}{I_s} = \frac{1}{j\omega C_{gs1}} g_m(r_{o1}||r_{02}), \tag{5.41}$$

which can be rearranged to yield

$$\frac{V_o}{I_s} = \frac{(r_{o1}||r_{02})}{j(\frac{\omega}{\omega_1})}, \tag{5.42}$$

where

$$\omega_1 = \frac{g_m}{C_{gs1}}. \tag{5.43}$$

Let us now compare this with the corresponding effective transfer function for the EAM system $\frac{V_{EAM}}{I_s}$, where I_s is the current that would result from direct (non-EAM, i.e. dc-bias only) detection at the sense port. Evaluating Eq. (5.34) for maximum output yields

$$\frac{V_{EAM}}{I_s} = \frac{\omega_c |v_c||r_{dm}|}{2j\omega V_P} \tag{5.44}$$

Combination of Eq. (5.44) with (5.26) yields for the transfer function at maximum EAM output

$$\frac{V_{EAM}}{I_s} = \frac{|r_{dm}|}{j(\frac{\omega}{\omega_1})}, \tag{5.45}$$

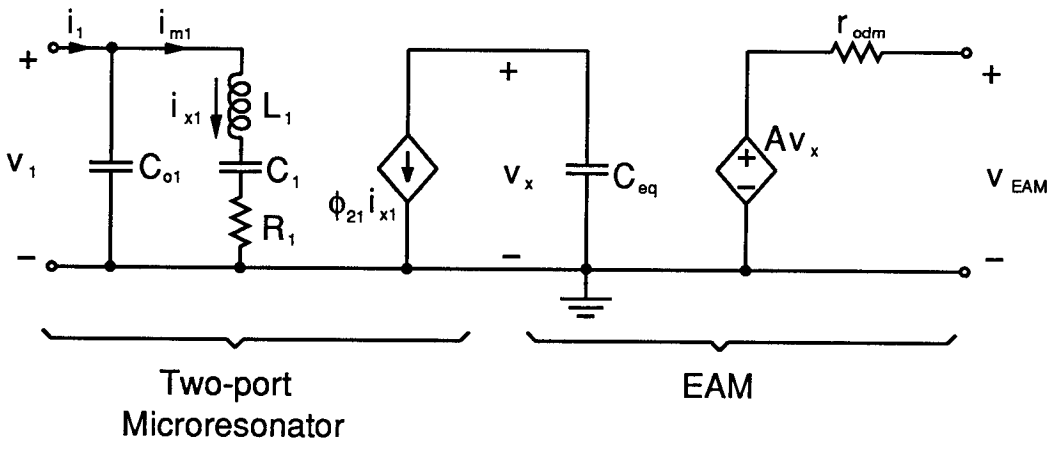

$$C_{eq} = \frac{1}{\omega_c |r_{dm}|}$$
$$A = \frac{|v_c|}{2V_P}$$

Figure 5.14. Equivalent circuit for the EAM system with element values.

where

$$\omega_1 = \frac{\omega_c |v_c|}{2V_P}. \tag{5.46}$$

Thus, the effective EAM transfer function has the same form as that for capacitive detection.

5.6 Equivalent Circuit Modelling EAM

The similarity between the effective EAM transfer function and that for capacitive detection suggests a similar equivalent circuit for the EAM system of Fig. 5.7 or Fig. 5.10. Such a circuit is presented in Fig. 5.14, which in addition to the circuit schematic includes expressions for the (new) circuit elements. Note that circuit applies to both one- and two-port microresonators.

The capacitance C_{EAM} corresponds to the C_{gs1} of Fig. 5.13, and its value is selected somewhat arbitrarily, but logically in that it is a capacitance. The main difference between the circuits of Fig. 5.13 and Fig. 5.14 emphasizes the most powerful feature of the EAM technique: The dc parasitic capacitors C_P of the former figure are eliminated in Fig. 5.14.

It should be noted that the EAM circuit of Fig. 5.14 makes no attempt to model correctly the components of input current at frequencies other than the drive signal frequency

ω_d. Only the drive port impedance for ω_d components are modelled. EAM current components at $(\omega_c \pm \omega_d)$ and frequency doubled components are not modelled. A circuit with a more complicated microresonator input model could be proposed to correct for this, using multipliers and adders (unconventional circuit elements), but for most cases, Fig. 5.14 should suffice.

6.0 APPLICATIONS OF EAM

Having discussed in detail the techniques available for electromechanical characterization of microresonators, this report now turns to applications of these techniques, in particular, of the EAM technique. In this chapter, application of this technique to microresonator circuit model extraction and system performance verification will be demonstrated. First, however, the usefulness of EAM as a design aid will be demonstrated.

6.1 Characterization of Mechanical Behavior

The transimpedance spectrum obtained by EAM, as shown in Fig. 2.11, holds not only information concerning the electromechanical behavior of a microresonator, but also provides a direct, quantitative measurement of pure mechanical behavior.

As an illustration of the usefulness of this feature, let us consider the spectra for the electrostatic-comb driven microresonator of Fig. 6.1(a), which is suspended by straight clamped-clamped beams, rather than folded-flexures. The system spring constant k_{sys} for this sort of suspension has a nonlinear dependence on displacement x, and consequently, has a force vs. displacement transfer function as shown in Fig. 6.1(b) [21].

Fig. 6.2 presents the spectra measured via the EAM technique for the cases of (a) an upward sweep in frequency; and (b) a downward sweep in frequency. The nonlinear spectrum of Fig.6.1(b) is evident.

6.2 Designing for $\frac{\partial C}{\partial x}$

In Chapter 2, the equivalent circuit for an electrostatic-comb driven lateral microresonator was calculated using a simple parallel-plate capacitance approximation for determination of $\frac{\partial C}{\partial x}$. This approximation was said to be largely incorrect due to second order effects, namely fringing of electric fields and levitation. This section will now demonstrate

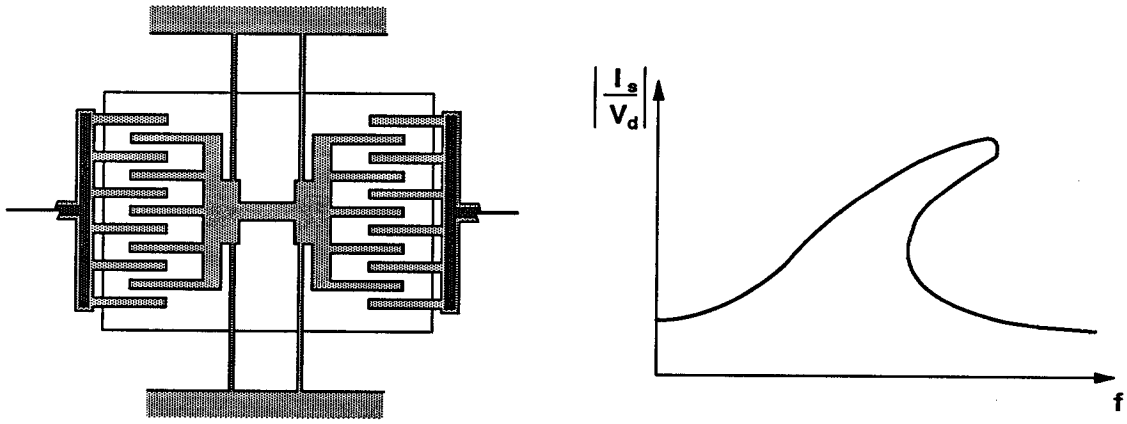

(a) (b)

Figure 6.1. (a) Electrostatic-comb driven lateral microresonator with clamped-clamped beams. (b) Typical frequency response spectrum for a resonator with a nonlinear spring constant.

the use of EAM to quantify the degree of inaccuracy inherent in the approximate $\frac{\partial C}{\partial x}$ model. In particular, the influence of ground plane design, first published by Tang, et. al. [11], will be quantified in terms of its effect on $\frac{\partial C}{\partial x}$, and thus, on the microresonator circuit model.

6.2.1 $\frac{\partial C}{\partial x}$ for the Case of a Uniform Ground Plane

Figure 6.3 shows the microphotograph of a microresonator with a uniform ground plane fabricated to the specifications of the example microresonator discussed in Chapter 2. The uniform ground plane induces an imbalance in the vertically directed electrostatic forces coupling the shuttle with drive and sense electrodes, as shown in Fig. 6.4 [11].

Two competing phenomena now determine the value of overlap capacitance, and thus, the value of $\frac{\partial C}{\partial x}$. The capacitance due to fringing electric fields around the overlapped fingers tends to increase the total capacitance over the value predicted by a simple parallel-plate approximation. On the other hand, levitation of the shuttle decreases the finger overlap area, thus, lowering the total capacitance.

The most dominant phenomenon can easily be revealed by inspection of a transconductance spectrum. Such a spectrum, obtained via EAM, is shown in Fig. 6.5. The value of $\left(\frac{\partial C}{\partial x}\right)_s$ can be calculated by obtaining the peak value of $|\frac{V_{EAM}}{V_d}|$ from Fig. 6.5, and using

$$\left(\frac{\partial C}{\partial x}\right)_s = \left[\frac{2|\frac{V_{EAM}}{V_d}|N_2 k_{sys}}{\omega_c V_P |v_c||r_{dm}|N_1 Q}\right]^{\frac{1}{2}}. \tag{6.1}$$

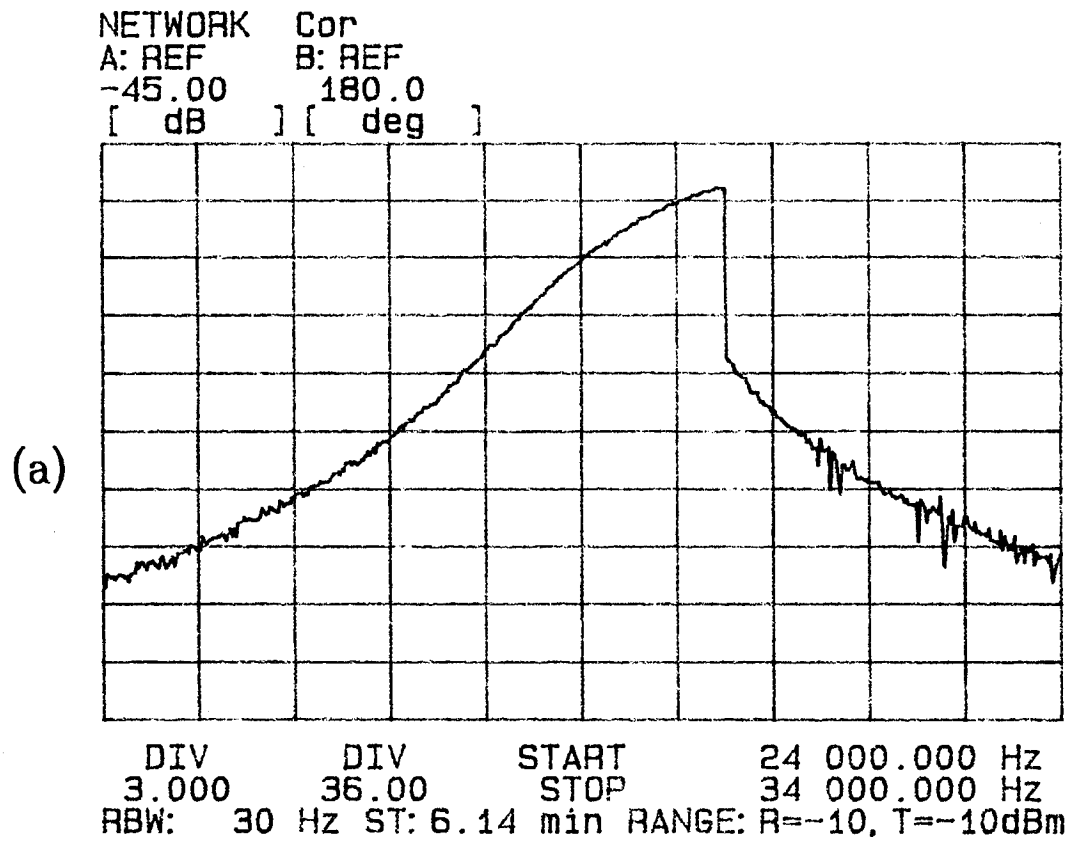

(a)

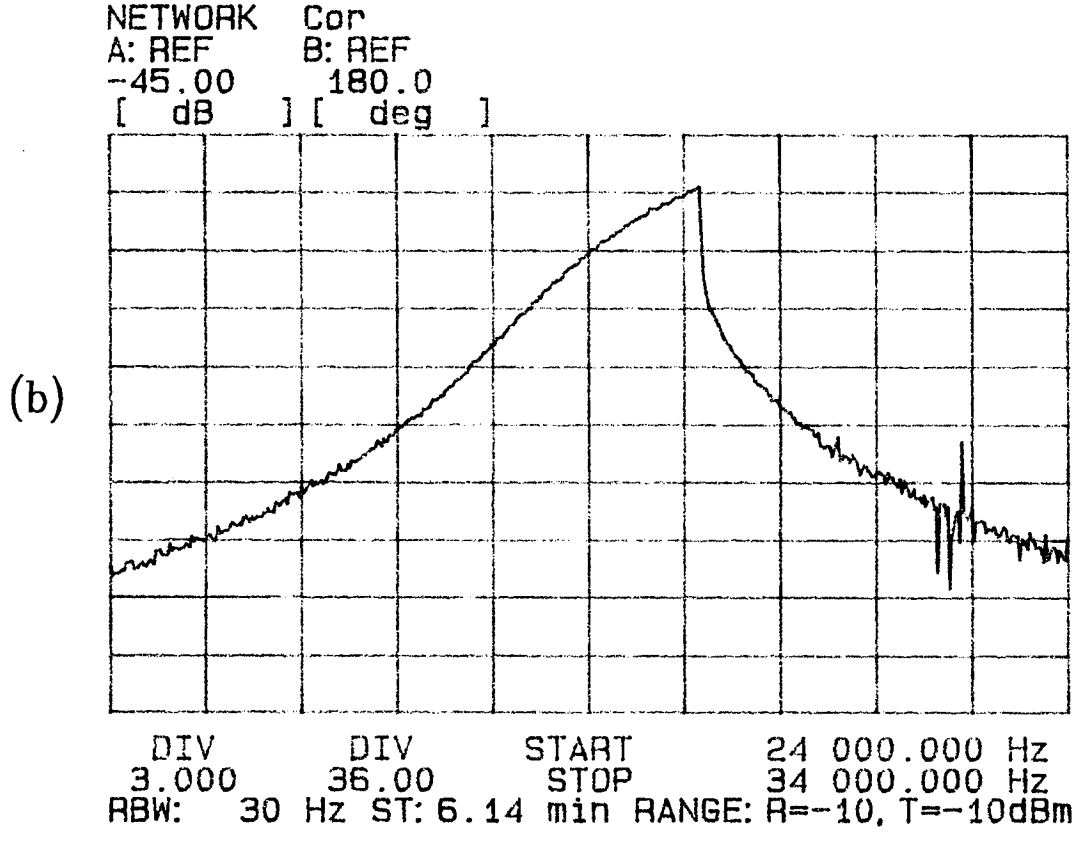

(b)

Figure 6.2. Frequency response of a fabricated clamped-clamped electrostatic-comb driven microresonator as measured via the EAM technique. In (a), the source is swept upward in frequency, while in (b), it is swept downward.

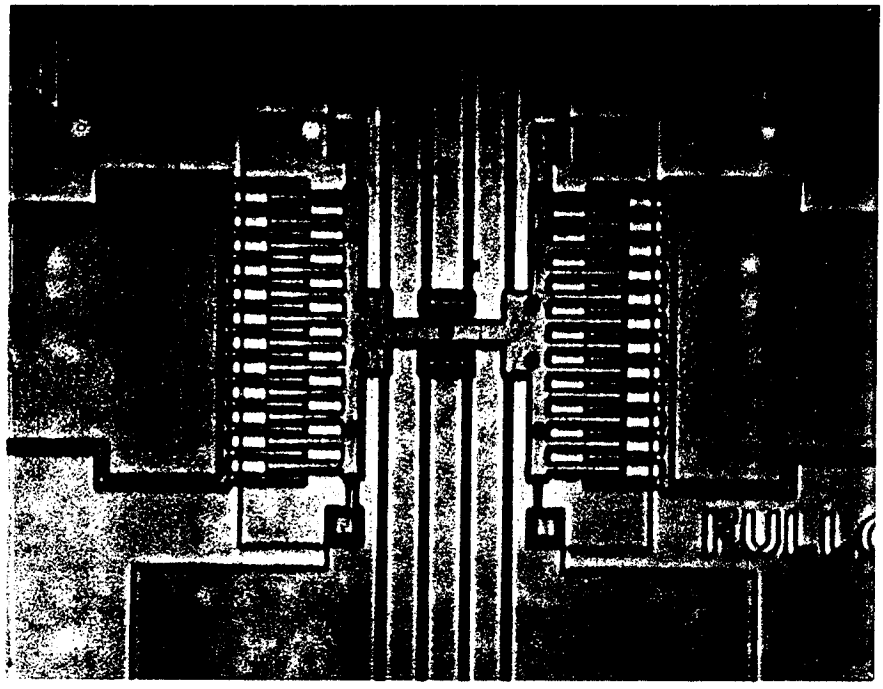

Figure 6.3. Microresonator utilizing a uniform (full) ground plane fabricated to the specifications of the example in Chapter 2.

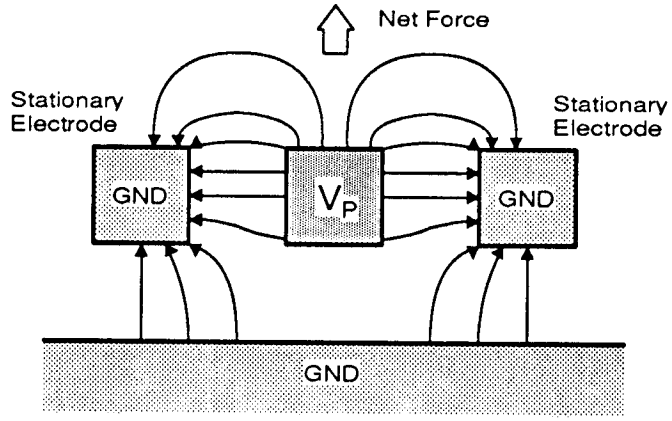

Figure 6.4. Illustration of the imbalance of vertically directed electric fields around the microresonator shuttle fingers and electrode fingers caused by a uniform ground plane. The net result is a vertically directed force. (Adapted from reference [11].)

Following this procedure, we obtain $\left(\frac{\partial C}{\partial x}\right)_s = 2.23 \times 10^{-10}$ F/m for the case of a full ground plane. Comparing this with the value obtained through simple theory, $\left(\frac{\partial C}{\partial x}\right)_s = 2.12 \times 10^{-10}$ F/m, we see that the effect of fringing fields dominates over the levitation effects.

6.2.2 $\frac{\partial C}{\partial x}$ for the Case of a Sliced Ground Plane

Tang et. al. showed that levitation due to an imbalance of vertically directed electric fields can be suppressed somewhat by use of a sliced ground plane, which is present only under the drive and sense fingers and under the area over which the shuttle fingers traverse during resonance. A top view microphotograph of a microresonator fabricated to the same specifications as above, but utilizing a sliced ground plane, is shown in Fig. 6.6. Its transconductance spectrum, as measured via EAM, is shown in Fig. 6.7. Using the procedure of the previous subsection, we find $\left(\frac{\partial C}{\partial x}\right)_s = 2.97 \times 10^{-10}$ F/m, which is 33 % higher

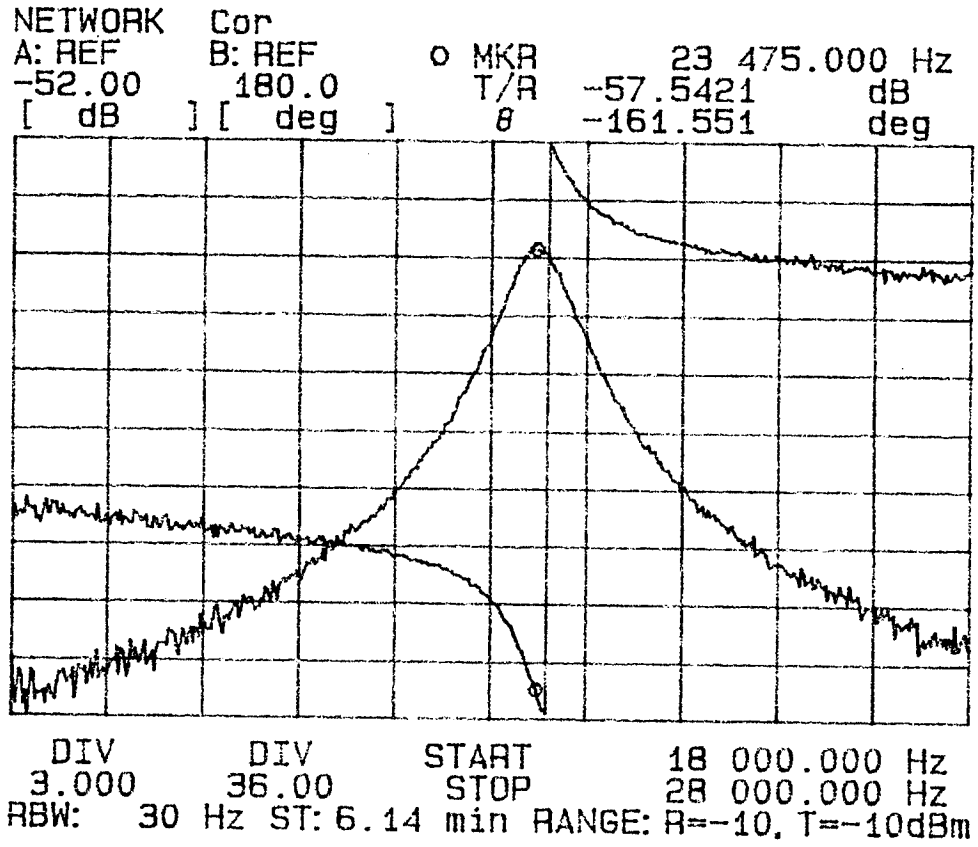

Figure 6.5. Transconductance spectrum for the microresonator of Fig. 6.3 as measured via EAM.

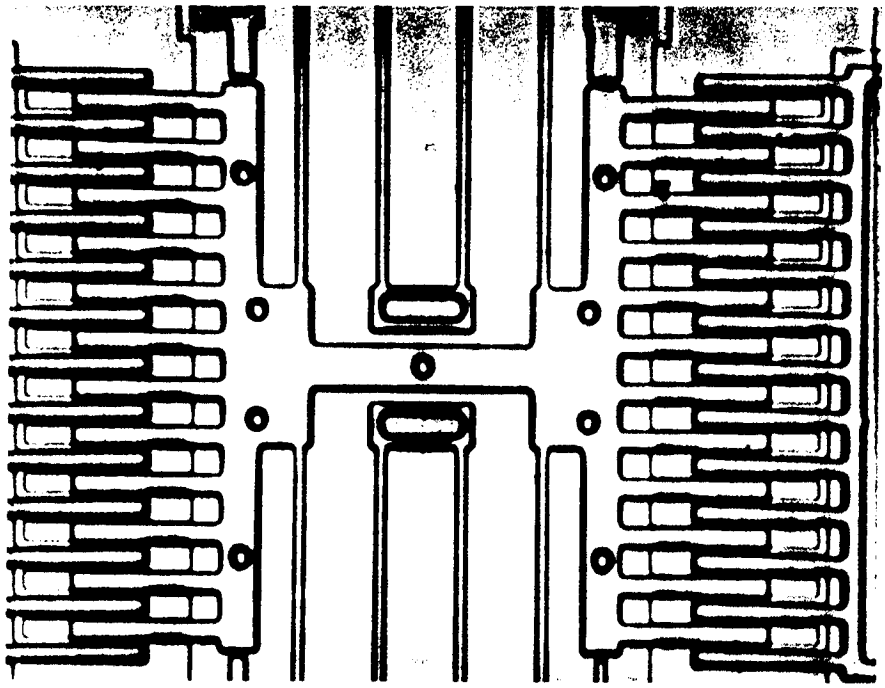

Figure 6.6. Microresonator utilizing a sliced ground plane fabricated to the specifications of the example in Chapter 2.

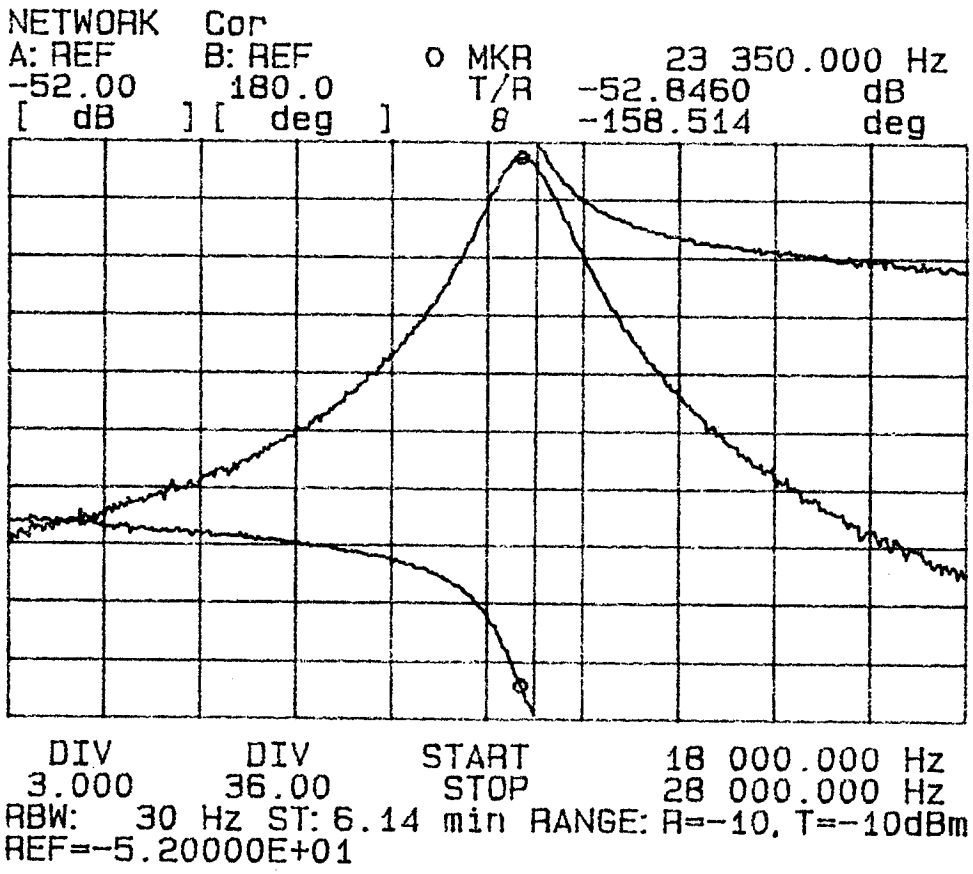

Figure 6.7. Transconductance spectrum for the microresonator of Fig. 6.6 as measured via EAM.

than for the case of a full ground plane. This value is also much higher than the value obtained through the simple theory of Chapter 2, $\left(\frac{\partial C}{\partial x}\right)_s = 2.12 \times 10^{-10}$ F/m. Evidently, reduction of levitation can greatly increase the transconductance of a microresonator.

6.3 Microresonator Circuit Extraction

Using data extracted from Fig. 6.7 and the equations in Fig. 2.7, the circuit elements modelling the fabricated microresonator are determined to be:

$$L_1 = 7.54 \times 10^4 \text{ H} \qquad L_2 = 7.54 \times 10^4 \text{ H}$$
$$C_1 = 9.41 \times 10^{-16} \text{ F} \qquad C_2 = 9.41 \times 10^{-16} \text{ F}$$
$$R_1 = 3.31 \times 10^8 \qquad R_2 = 3.31 \times 10^8$$
$$\phi_1 = -1.0 \qquad \phi_2 = -1.0$$

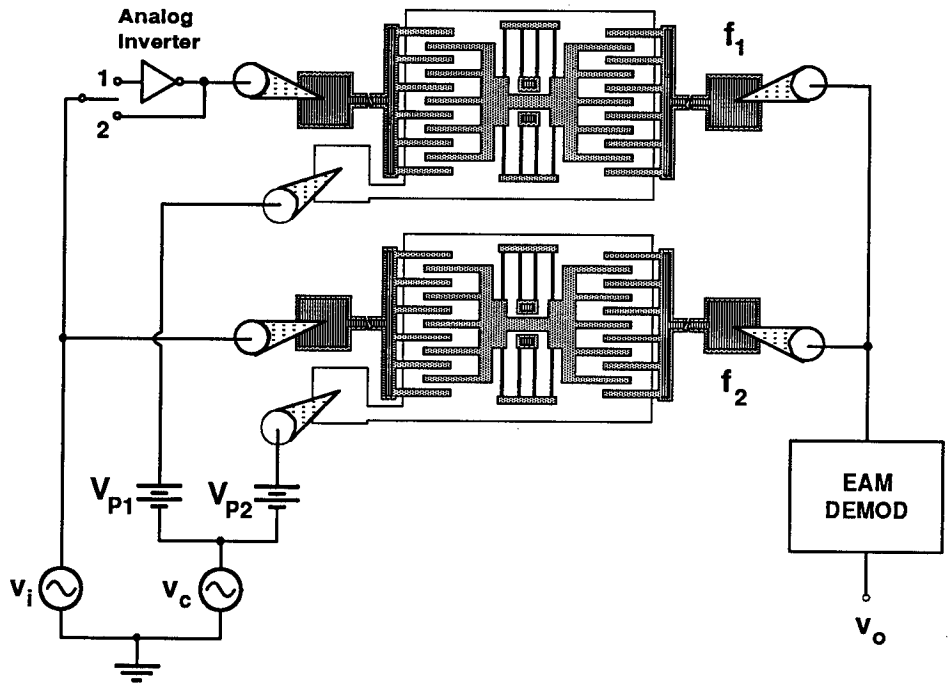

Figure 6.8. Schematic of a parallel microresonator filter. When the switch is set at 1, the analog inverter provides a 180° phase shift and a bandpass filter results. When the switch is set at 2, a notch filter is implemented.

Note that the value of series resistance R calculated using the simple theory of Chapter 2 overshoots the actual value by more than 100 %.

6.4 Microresonator System Performance Verification: Parallel Microresonator Filters

Possibly the most useful application of EAM is for off-chip verification of microresonator system performance. To illustrate, we introduce the parallel microresonator electromechanical filter, shown in Fig. 6.8 biased for EAM detection. This filter operates through the addition of properly phased current outputs of microresonators with resonance frequencies differing by a specific amount, and thus, its performance may only be verified by an *electrically*-based sensing scheme.

Both a bandpass filter and a notch filter can be implemented via this scheme. For the case of the bandpass filter, the phase (Fig. 6.9(a)) of the microresonators are selected such that currents combine in the interval of frequency between the resonances (currents are in

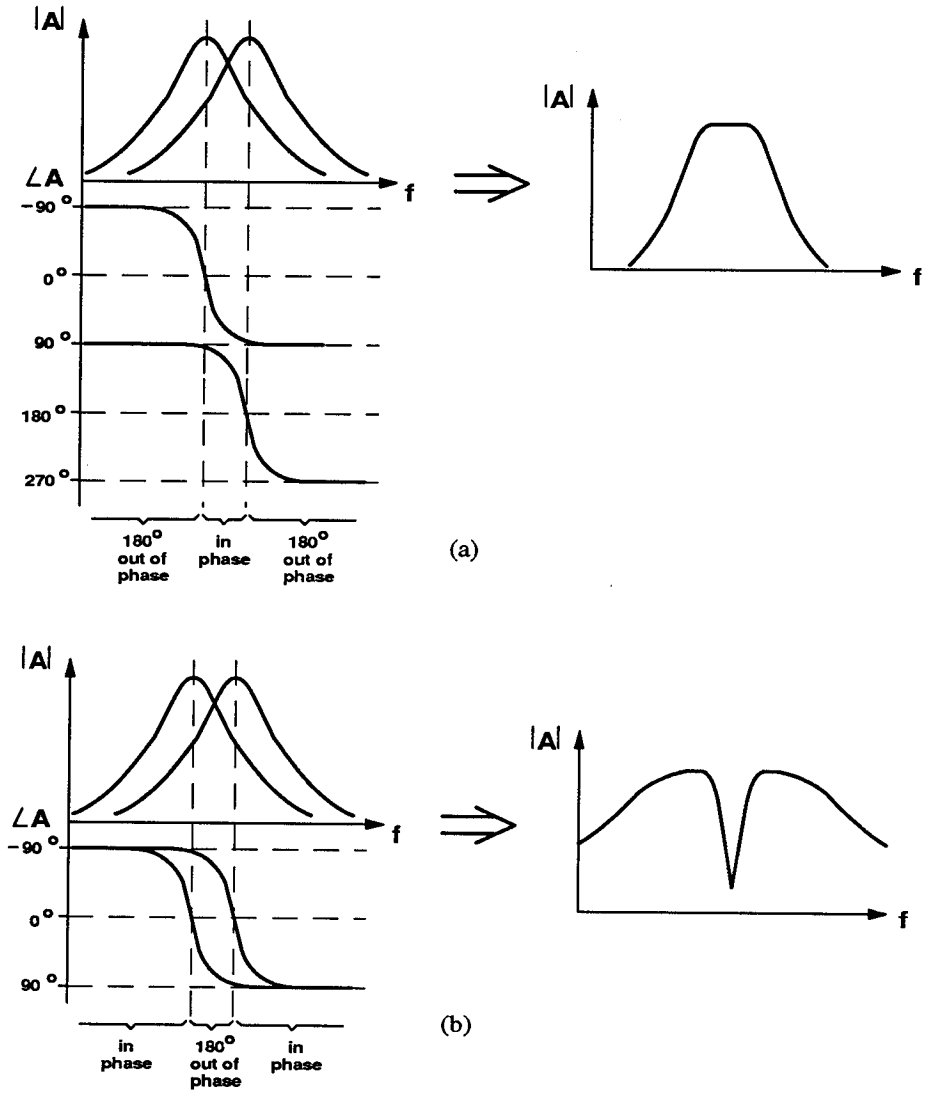

Figure 6.9. Mechanism behind parallel microresonator filters for the case of (a) a bandpass filter; and (b) a notch filter. In (a), microresonator currents at frequencies between the resonances of the microresonators are in phase, and thus, add. Those at frequencies outside this interval are 180° out of phase, and thus, subtract, leading to improved roll-off. In (b), everything in (a) is turned around.

phase) but subtract outside this interval (currents are approximately 180° out-of-phase). This subtraction leads to increased roll-off outside the passband. In Fig. 6.8, the bandpass filter is implemented when the switch is set at 1, which includes the analog inverter.

For the notch filter, the phasing scheme is reversed as shown in Fig. 6.9(b). Here, there is subtraction between the resonances and addition outside. The notch filter is implemented when the switch is set at 2 in Fig. 6.8.

Experimentally measured spectra using the EAM technique are presented in Fig. 6.10, for (a) a bandpass filter and (b) a notch filter. The filters of Fig. 6.10 were designed for operation under atmospheric pressure, and thus, they are relatively low-Q filters. Design and operation under vacuum would greatly enhance the performance of these filters in terms of roll-off, noise, and stability. High-Q design does not necessarily mean that the required drive voltage will be small. To suppress the effects of noise, it is preferable that large drive voltages be required. For either case, the EAM technique can verify the electromechanical performance of a microelectromechanical filter *without the need for on-chip electronics.*

(a)

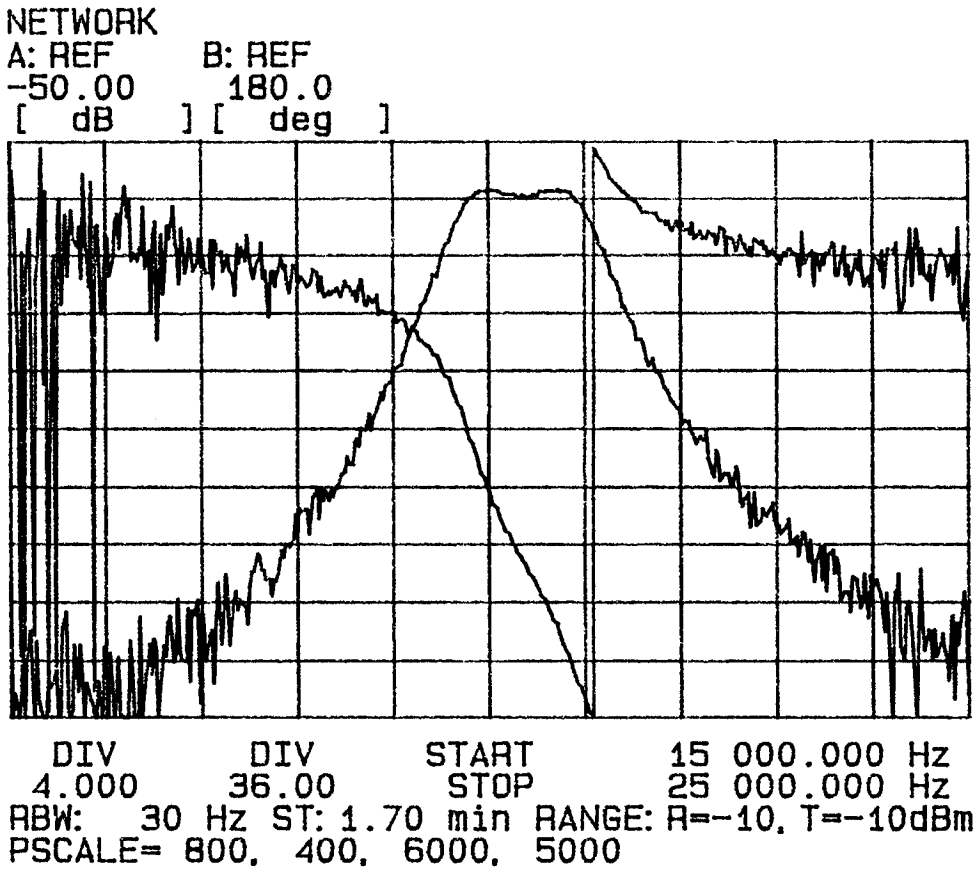

(b)

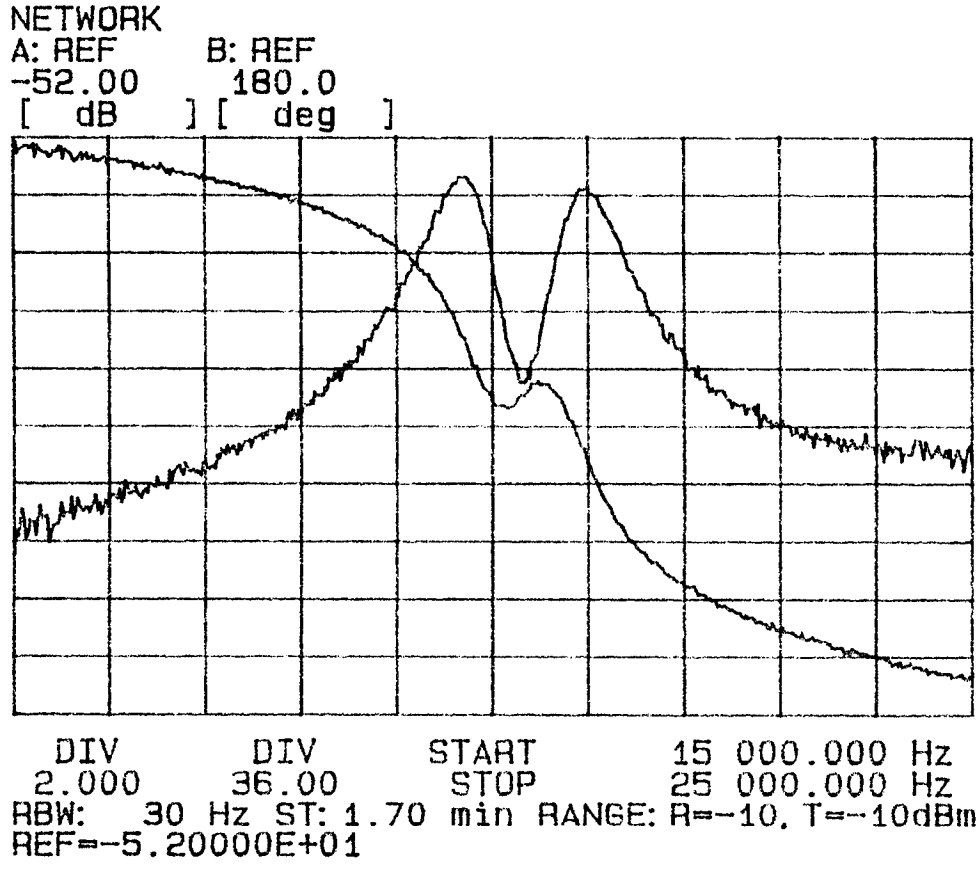

Figure 6.10. Experimental frequency response spectra for (a) a bandpass parallel microresonator filter and (b) a notch filter. These spectra were measured via the EAM technique under low-Q conditions: Q = 27.

7.0 CONCLUSIONS

To summarize, a time-domain method and a technique based upon electromechanical amplitude modulation (EAM) that *electrically* detect microresonator motional current using only *off-chip* electronics have been analyzed and demonstrated. This EAM technique is useful for one-port, as well as multi-port microresonators with virtually any range of Q. It has been successfully demonstrated as a convenient, repeatable, wafer-level measurement technique.

Application of the EAM technique to microresonator circuit model extraction and system performance verfification has been demonstrated. Design of the microresonator ground plane has been found to affect the series resistance by more than 50 %, and thus, careful consideration should be given to ground plane design when implementing microresonator systems. The performance of parallel microresonator filters, which operate through combination of the properly phased output currents from microresonators with resonance frequencies spaced a certain interval apart, have been verified without the need for on-chip electronics. Through EAM, months of integrated circuit processing time is saved.

7.1 On-chip Application of EAM

Although EAM has been described as a convenient *off-chip* detection technique, it also shows a strong potential for application in integrated detection circuitry because of its ability to null dc capacitance. As was seen in Fig. 3.4, only 5 fF in parallel with a microresonator (or microresonator system) can seriously distort its performance. This sensitivity to external capacitance is a consequence of tiny device dimensions, and thus, is an intrinsic problem associated with capacitively driven and sensed micromechanical devices.

The capacitance required to distort microresonator performance can easily be produced by a single MOS transistor, which in a 2 μm technology usually has a gate-to-source capacitance on the order of 20 fF. Of course, whether a circuit distorts microresonator per-

formance, or not, depends upon the particular design; i.e. for the gate capacitance of an MOS transistor to be in parallel with a microresonator, the transistor would have to be used in some sort of feedback between the microresonator input and output. The main point, however, is that, even on-chip, there exist circuit configurations that can contribute enough unwanted capacitance to distort system performance. In these cases, and for high performance situations, where any amount of feedthrough, no matter how small, should be eliminated (i.e. micromechanical filters), an on-chip EAM implementation might be desired.

APPENDIX A

Figure 7.1 shows the schematic of the actual EAM circuit used for this report. It uses an active high pass filter designed via well-known techniques. The filter, however, is actually a bandpass filter, since the op amps used cut off at around 5 MHz. Better noise performance can be achieved if a passive bandpass filter is used.

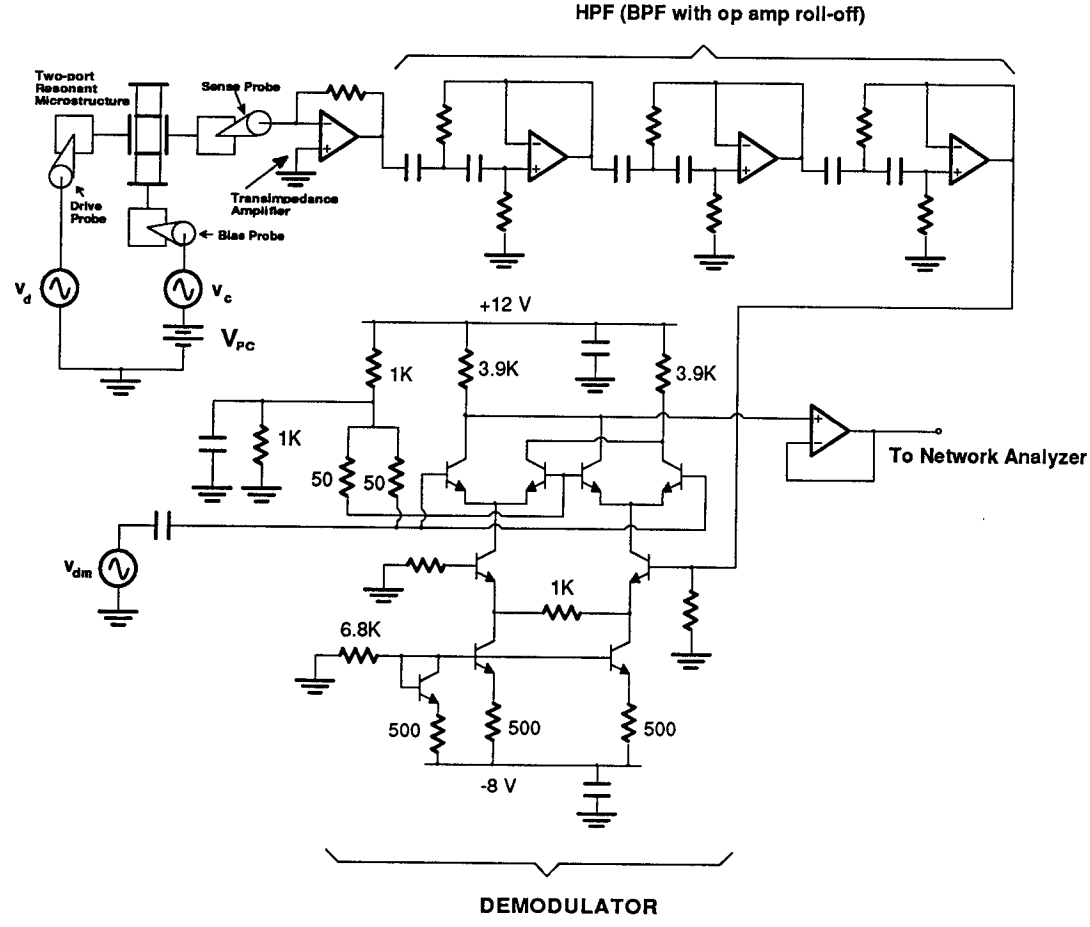

Figure 7.1. Practical implementation of the EAM system. The filter should be designed for a cutoff frequency near the highest microresonator frequency to be measured.

For demodulation, a simple balanced multiplier, such as the LM1496, can be used.

BIBLIOGRAPHY

[1] R. T. Howe, "Resonant microsensors," *Technical Digest*, 4th International Conference on Solid-State Sensors and Actuators, Tokyo, Japan, June 2-5, 1987, 843-848.

[2] M. A. Schmidt and R. T. Howe, "Resonant structures for integrated sensors," *Technical Digest*, IEEE Solid-State Sensor Workshop, Hilton Head Island, South Carolina, June 2-5, 1986.

[3] R. M. Langdon, "Resonator sensors—a review," *J. Phys. E., Sci. Inst.*, **18**, 103-115, (1985).

[4] E. P. EerNisse and J. M. Parcos, "Practical considerations for miniature quartz resonator force transducers," *Proceedings*, 28th ISA International Instrumentation Symposium, 1982, 33-44.

[5] J. G. Smits, H. A. C. Tilmans, and T. S. J. Lammerink, "Pressure dependence of resonant diaphragm pressure sensors," *Technical Digest*, 3rd International Conference on Solid-State Sensors and Actuators, Philadelphia, Pennsylvania, June 11-14, 1985, 93-96.

[6] J. C. Greenwood, "Etched silicon vibrating sensor," *J. Phys. E., Sci. Inst.*, **17**, 650-652, (1984).

[7] K. Ikeda, *et al*, "Silicon pressure sensor with resonant strain gauges built into diaphragm," *Technical Digest*, 7th Sensor Symposium, Tokyo, Japan, May 30-31, 1988, 55-58.

[8] D. C. Satchell and J. C. Greenwood, "Silicon microengineering for accelerometers," *Proc. Inst. of Mech. Eng.*, **1987-2**, Mechanical Technology of Inertial Devices, Newcastle, England, April 7-9, 1987, 191-193.

[9] R. T. Howe and R. S. Muller, "Resonant microbridge vapor sensor," *IEEE Trans. on Electron Devices*,**ED-33**, 499-506, (1986).

[10] W. C. Tang, T.-C. H. Nguyen, and R. T. Howe, "Laterally driven polysilicon resonant microstructures," *Sensors and Actuators*, vol. 20, 25-32, 1989.

[11] W. C. Tang, M. G. Lim, and R. T. Howe, "Electrostatically balanced comb drive for controlled levitation," *Technical Digest*, IEEE Solid-State Sensor and Actuator Workshop, Hilton Head Island, South Carolina, June 4-7, 1990, 23-27.

[12] M. W. Putty, "Polysilicon resonant microstructures," M.S. Thesis, Dept. of Electrical Engineering and Computer Science, University of Michigan, Ann Arbor, Mich., September, 1988.

[13] D. W. DeRoo, "Determination of Young's modulus of polysilicon using resonant micromechanical beams," M.S. Thesis, Dept. of Electrical Engineering, University of Wisconsin, Madison, January 1988.

[14] W. Benecke, *et al*, "Optically excited mechanical vibrations in micromachined silicon cantilever structures," *Technical Digest*, 4th International Conference on Solid-State Sensors and Actuators, Tokyo, Japan, June 2-5, 1987, 838-842.

[15] H. Guckel, T. Randazzo, and D. W. Burns, "A simple technique for the determination of mechanical strain in thin films with application to polysilicon," *J. Appl. Phys.*, vol. 57, 1985, pp. 1671-1675.

[16] E. P. EerNisse, "Quartz resonator frequency shifts arising from electrode stress," *Proceedings*, 29th Annual Symp. on Frequency Control, 1976, pp. 1-4.

[17] R. A. Brennen, M. G. Lim, A. P. Pisano, and A. T. Chou, "Large displacement linear actuator," *Technical Digest*, IEEE Solid-State Sensor and Actuator Workshop, Hilton Head Island, South Carolina, June 4-7, 1990.

[18] M. A. Schmidt, R. T. Howe, S. D. Senturia, and J. H. Haritonidis, "Design and calibration of a microfabricated floating-element shear-stress sensor," *IEEE Trans. on Electron Devices*, **35**, 750-757, (1988).

[19] G. L. Turin, *EECS 124: Spectrum Analysis Laboratory Manual*, Dept. of Electrical Engineering and Computer Sciences, University of California at Berkeley, March 1980.

[20] W. F. Thomson, *Theory of Mechanical Vibrations*, Englewood Cliffs, NJ: Prentice-Hall Inc., 1971.

[21] S. Timoshenko, D. H. Young, and W. Weaver, Jr., *Vibration Problems in Engineering*, New York: John Wiley & Sons, 1974.